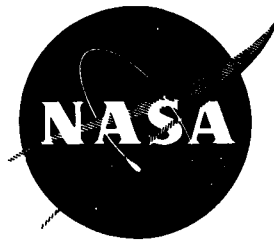


N73-18801

NASA-CR-120896



**CASE FILE  
COPY**

**HYDROGEN - OXYGEN AUXILIARY PROPULSION  
FOR THE SPACE SHUTTLE**

**VOLUME II: LOW PRESSURE THRUSTERS**

by

Aerojet Liquid Rocket Company  
Sacramento, California 95812



prepared for

**NATIONAL AERONAUTICS AND SPACE ADMINISTRATION**

NASA Lewis Research Center

Contract NAS 3-14354

John W. Gregory, Technical Management

## NOTICE

This report was prepared as an account of Government-sponsored work. Neither the United States, nor the National Aeronautics and Space Administration (NASA), nor any person acting on behalf of NASA:

- A. Makes any warranty or representation, expressed or implied, with respect to the accuracy, completeness, or usefulness of the information contained in this report, or that the use of any information, apparatus, method, or process disclosed in this report may not infringe privately-owned rights; or
- B. Assumes any liabilities with respect to the use of, or for damages resulting from the use of, any information, apparatus, method or process disclosed in this report.

As used above, "person acting on behalf of NASA" includes any employee or contractor of NASA, or employee of such contractor, to the extent that such employee or contractor of NASA or employee of such contractor prepares, disseminates, or provides access to any information pursuant to his employment or contract with NASA, or his employment with such contractor.

Requests for copies of this report should be referred to

National Aeronautics and Space Administration  
Scientific and Technical Information Facility  
P.O. Box 33  
College Park, Md. 20740

Final Report

HYDROGEN-OXYGEN AUXILIARY PROPULSION  
FOR THE SPACE SHUTTLE

Volume II: Low Pressure Thrusters

Prepared for

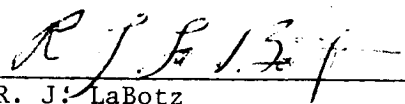
National Aeronautics and Space Administration  
Contract NAS 3-14354

30 January 1973

by

Aerojet Liquid Rocket Company

Approved by:

  
R. J. LaBotz  
Program Manager

Technical Management: John W. Gregory  
Liquid Rocket Technology Branch  
NASA Lewis Research Center  
Cleveland, Ohio 44135

### ABSTRACT

An abbreviated program was conducted to investigate igniter, injector, and thrust chamber technology for a  $10.3 \text{ N/cm}^2$  (15 psia) chamber pressure, 6660 N (1500 lbf) gaseous  $\text{H}_2/\text{O}_2$  APS thruster for the Space Shuttle Vehicle. Successful catalytic igniter tests were conducted with ambient and cold propellants. Injector testing with a heat sink chamber ( $\text{MR} = 2.5$ , area ratio = 5.0) gave a measured specific impulse of 386 sec with 11% of the fuel used as film coolant. This coolant flow rate was demonstrated to be more than adequate to cool a spun adiabatic wall, flightweight thrust chamber.



## TABLE OF CONTENTS

	<u>Page</u>
I. Summary	1
II. Introduction	3
A. Background	3
B. Objective	4
C. Scope of Work	4
D. Criteria	4
III. Technical Discussion	7
A. Injectors	7
B. Heat Sink Chambers	55
C. Cooled Chambers	62
D. Catalytic Igniter	87
E. Thrust Chamber Valves	109
F. Injector Testing (Task XVIII)	114
G. Heat Sink Chamber Testing	134
Appendix A	143

<u>Table</u>	<u>TABLE LIST</u>	<u>Page</u>
I	Engine Operating Conditions	5
II	Engine Design Requirements	5
III	Coaxial Element Cold Flow Test Summary	15
IV	Injector Face Fatigue Life Design Predictions	30
V	Vaned Element Cold Flow Test Summary	36
VI	Nozzle Optimization Summary	58
VII	Reverse Dump Cooled Chamber Pressure Loss Distribution	85
VIII	Catalytic Igniter Data - Test Series 1 and 2	95
IX	Catalytic Igniter Data - Test Series 3	98
X	Catalytic Igniter Data - Test Series 4	100
XI	Catalytic Igniter Data - Test Series 5	101
XII	Catalytic Igniter Data - Test Series 6	103
XIII	Data Obtained from Tests with the Low P <sub>c</sub> Catalytic Igniter During Tests with Cold Propellants, Test Series 7	106
XIV	Engine Test Data and Performance Summary	121
XV	Performance Summary	132

<u>Figure</u>	<u>FIGURE LIST</u>	<u>Page</u>
III-1	Coaxial Element Injector	10
III-2	Hydrogen Manifold Velocity vs Number of Elements	12
III-3	Element Dimensions vs Number of Elements	12
III-4	Coaxial Injector Cold Flow Element Configurations	13
III-5	Effect of Mixture Ratio on Coaxial Element Mixing Efficiency	17
III-6	Effect of Oxygen Swirl on Mass and Mixture Ratio Profiles	18
III-7	Effect of Fuel Velocity on Coaxial Element Mixing Efficiency	21
III-8	Effect of Oxygen Post Recess on Coaxial Element Mixing Efficiency	22
III-9	Effect of Oxygen Post Recess on Hydrogen Annulus Mixture Ratio	23
III-10	Mixture Ratio Distribution of Scarfed Element with Nonswirling Oxygen	25
III-11	Mixture Ratio Distribution of Scarfed Element with Swirling Oxygen	26
III-12	Predicted Coaxial Element Injector Face Temperatures	28
III-13	Mixture Ratio Profiles Based on Cold Flow Data	32

<u>Figure</u>	<u>FIGURE LIST (cont.)</u>	<u>Page</u>
III-14	Vaned Injector Element Assembly	34
III-15	Typical Shadowgraph	39
III-16	Penetration Characteristics	41
III-17	Velocity Comparisons	42
III-18	Jet Spreading Characteristics	45
III-19	Vane Flow Distribution	46
III-20	Vane Flow Characteristics	48
III-21	Segment Mixing and Distribution Model	49
III-22	Radial and Axial Mixture Ratio Profiles - Vane Injector	50
III-23	Radial Mixture Ratio Profile	51
III-24	Workhorse Chamber Assembly	57
III-25	Thermocouple Installation	60
III-26	Cooled Chamber Concepts	66
III-27	Film-Cooled Chamber	67
III-28	Predicted Film Temperature Profiles	69
III-29	Predicted Film-Cooled Chamber Gas-Side Transient Temperatures	70
III-30	Film-Cooled Chamber Loads and Resultant Stress Profiles	72
III-31	Reverse Dump Cooled Chamber Section	74
III-32	Reverse Dump Cooled Chamber Assembly	75
III-33	Predicted Reverse Dump Cooled Chamber Throat Temperature	77
III-34	Reverse Dump Cooled Chamber Temperature Profile	79
III-35	Predicted Film Coolant Ring Thermal, Hydraulic, and Injection Characteristics	80
III-36	Reverse Dump Cooled Chamber Liner Thermal Stress	82
III-37	Effect of Applied Strain on Cycle Life of Reverse Dump Cooled Liner	84
III-38	Catalytic Igniter Assembly	88
III-39	Catalytic Igniter Hydraulic Analysis Schematic	92
III-40	Catalytic Igniter Hardware	93
III-41	Flow Characteristics of Titan Valve	110

FIGURE LIST (cont.)

<u>Figure</u>		<u>Page</u>
III-42	Thrust Chamber Valve Travel Times	112
III-43	Thrust Chamber Valve Control System Response	113
III-44	Streak Chamber - Postfire Condition	117
III-45	Injector Energy Release Performance	123
III-46	Influence of Design Parameters on Injector Performance	126
III-47	Film Cooling Performance Loss vs Mixture Ratio	129
III-48	Film Cooling Performance Loss vs Percent Film Cooling	130
III-49	Corrected Altitude Performance	133
III-50	Wall Heat Flux vs Wall Temperature	135
III-51	Experimental Heat Flux to a 533°K (500°F) Wall	137
III-52	Throat Heat Flux vs Percent Film Cooling and Chamber Pressure	139
III-53	Recovery Temperatures with Film Cooling	141

## I. SUMMARY

The objective of the low pressure portion of this program was to establish a technology base for subsequent development of a low chamber pressure (6.9 to 13.8 N/cm<sup>2</sup> (10 to 20 psia)), gaseous oxygen/gaseous hydrogen auxiliary propulsion system (APS) thruster. Primary emphasis in the program was to be on igniter, injector, and cooled chamber technology. Midway in the program the low pressure work was terminated in favor of additional high pressure work. This report describes the accomplishments of the truncated low pressure thruster program.

Design, cold flow, and fabrication work was performed on two different injector concepts: (1) a 200 element coaxial design; and (2) a unique vaned concept. Only the coaxial injector was carried completely through fabrication and into hot fire testing before the point of program termination. Twenty-four thruster tests were conducted for performance and heat transfer data. These tests were conducted using a workhorse chamber, and a film coolant ring designed to introduce hydrogen coolant at various velocities and axial positions. All tests were conducted at simulated altitude conditions.

The parameters evaluated are shown below:

$P_c$	6.9 to 13.8 N/cm <sup>2</sup> (10 to 20 psia)
Mixture ratio	2 to 4
$L^*$	41 and 66 cm (16 and 26 in.)
Film coolant	0 to 30% (of the hydrogen)
Coolant sleeve length	1.27 to 7.1 cm (0.5 to 2.78 in.)

The specific impulse performance for all tests exceeded the 375-sec contract goal, including tests with 30% film coolant. Thermal data indicate that the film-cooled chamber design can operate successfully with 11% hydrogen coolant at a 1087°K (1500°F) maximum wall temperature. The altitude performance at this condition is 389 sec.

## I. Summary (cont.)

Design work was initiated on both film cooled and reverse dump cooled chambers. The final detailed designs were not completed and no cooled chamber fabrication work was initiated.

Over 200 tests were conducted with a catalytic igniter at simulated altitude conditions. The design employs a small catalyst bed for primary reaction with additional (secondary) oxygen added to the bed effluent to increase the heat output of the assembly.

The shortest times to the reaction of the secondary oxygen with the effluent ranged from 0.03 sec for a hot bed restart with ambient propellants to 0.075 sec with ambient temperature bed and propellants. Successful ignitions were achieved with both the propellant and bed temperatures at approximately 161°K (290°R). Operation was found to be somewhat unpredictable at all temperatures in that tests at identical conditions resulted in different response characteristics.

Relatively fast response of a catalytic ignition system for oxygen-hydrogen was demonstrated. Additional effort is required to improve operating reproducibility.

## II. INTRODUCTION

### A. BACKGROUND

The National Aeronautics and Space Administration has conducted feasibility and preliminary design studies of a fully recoverable and reusable space transportation system, commonly referred to as the Space Shuttle vehicle. As initially conceived, the vehicle consisted of two separate manned elements, a booster stage and an orbiter stage, each of which is individually recoverable. The Space Shuttle vehicle is designed to provide low cost transportation to earth orbit to support a variety of missions, including logistics resupply of a Space Station.

In order to achieve maximum cost effectiveness the space transportation system will be designed for up to 100 flights (reuses) over a 10 year operational lifetime and will be capable of relaunch within two weeks after landing. The system will be designed to minimize required post-flight refurbishment, maintenance, and checkout.

The hydrogen-oxygen propellant combination was considered for use in the mainpropulsion systems of both the booster and orbiter stages, because of its high performance, relatively low cost, and non-toxic, non-corrosive nature. These propellants were also considered for the APS for the same reasons plus the additional benefits derived from commonality between the main and auxiliary propellant storage and feed systems. These benefits included possible use of main engine boost residuals for auxiliary propulsion requirements and potential flexibility in distribution of orbital maneuvering propellant between the main engines and the APS to provide capability for a wide range of missions.

Hydrogen-oxygen propellants have been widely used for large main propulsion engines, but their application to an auxiliary propulsion engine is relatively new. Although some technology work has been done on small, low pressure  $H_2-O_2$  engines, a great deal more work was needed to provide an adequate technology base for the Space Shuttle application.

## II, Introduction (cont.)

### B. OBJECTIVE

The objective of this program was to generate a comprehensive technology base for high performance, gaseous hydrogen-gaseous oxygen rocket engines suitable for the auxiliary propulsion systems (APS) of the Space Shuttle vehicle in the chamber pressure regime from 6.8 to 13.6 N/cm<sup>2</sup> (10-20 psia). This technology groundwork will provide input for the auxiliary propulsion systems tradeoff studies and configuration decisions on an overall vehicle basis. It will insure that specifications established for the APS are realistic and achievable, and it will provide the basis for an expeditious engine development program.

### C. SCOPE OF WORK

The scope of this program was to conduct a program of analytical and experimental efforts to investigate the use of gaseous hydrogen-gaseous oxygen propellants in auxiliary propulsion engines. The principal efforts in this program were devoted to evaluation of thrust chamber cooling concepts, gas-gas injector designs, injector/chamber interactions, and the pulsing and steady-state performance of the complete thrust chamber assembly, including the valves, igniter, injector, and chamber. Ignition and valve work were generally limited to the efforts required to prepare these components for testing with the injector and injector/chamber assembly.

### D. CRITERIA

Nominal design point and the ranges of operating conditions for this program are given in Table I.



II,D, Criteria (cont.)

TABLE I  
ENGINE OPERATING CONDITIONS

	<u>Nominal Design Point</u>	<u>Testing Range</u>
Thrust:	6720N (1500 pounds)	--
Chamber Pressure:	10.2 N/cm <sup>2</sup> (15 psia)	6.9-13.8 N/cm <sup>2</sup> (10-20 psia)
Mixture Ratio	2.5	2.0 - 4.0
Nozzle Expansion Ratio	5:1	--
Propellant Inlet Temperatures:		
Hydrogen	300°K (540°R)	111-444°K (200-800°R)
Oxygen	300°K (540°R)	111-444°K (200-800°R)
Propellant Inlet Pressures (to valve):		
Hydrogen:	13.8 N/cm <sup>2</sup> (20 psia) (Max.)	As required
Oxygen:	17.3 N/cm <sup>2</sup> (25 psia) (Max.)	As required
C* Efficiency (goal):	95%	--
Specific Impulse (goal):	375 secs	--

The general engine design requirements are listed in Table II.

TABLE II  
ENGINE DESIGN REQUIREMENTS

Fuel: Gaseous hydrogen derived from the vaporization of liquid hydrogen per MIL-P-27201.

Oxidizer: Gaseous oxygen derived from the vaporization of liquid oxygen per MIL-P-25508A.

Installation: Buried within vehicle mold line.

Maximum External Temperature: 700°K (800°F)

Total Life Capability: Estimated 50 hours, with maintenance, based on 30 minutes life required per mission for 100 missions during a 10 year period.

Total Number of Pulses: Estimated 1,000,000 pulses, with maintenance, based on 10,000 pulses per mission for 100 missions during a 10 year period.

II,D, Criteria (cont.)

TABLE II. ENGINE DESIGN REQUIREMENTS (cont.)

Maximum Single Firing Duration: 1000 seconds

Duty Cycle Limitations: None

Compatibility: Compatible with propellants, test fluids, and cleaning fluids for 10 year life requirement.

Reusability: To be reusable with minimum servicing and refurbishment

Service and Maintainability: Designed for ease of service and maintenance when required.

Minimum Impulse Bit (goal): 223 N sec (50 lb sec)

Response: 50 milliseconds (Time from electrical signal to 90% thrust).

### III. TECHNICAL DISCUSSION

As originally defined, this contract contained 21 tasks. Tasks I through X constituted the High  $P_c$  program while Tasks XI through XX made up the Low  $P_c$  program with Task XXI being a common reporting task.

<u>Task Titles</u>	<u>Low <math>P_c</math> Task</u>
Injector analysis and design	XI
Injector fabrication	XII
Thrust chamber analysis and design	XIII
Thrust chamber fabrication	XIV
Ignition system analysis and design	XV
Ignition system fabrication and checkout	XVI
Propellant valves preparation	XVII
Injector tests	XVIII
Thrust chamber cooling tests	XIX
Pulsing tests	XX

Part way through the program, the program objectives were redirected toward providing an expanded high pressure program which would analytically and experimentally investigate the impact of lower temperature propellants (fuel = 150 to 600°R, oxidizer = 300 to 600°R). Work on Tasks XIV, XIX, and XX was halted by a stop work order while the scope of work on Tasks XII, XIII, XVII, and XVIII was reduced to that compatible with closing out Low  $P_c$  activities in an orderly manner. The following section discusses the work performed and results obtained under the reduced program.

#### A. INJECTORS

##### 1. Preliminary Concept Evaluation and Selection

The selection of injector element types for this program was based on studies conducted in support of the proposal, where four candidate

### III,A, Injectors (cont.)

elements were compared for this application. These element types were: two coaxial configurations, one using 80 elements and one using 900 elements; an 84-element triplet; and a radial vane configuration which distributes fuel across the injector face through radial vanes prior to mixing with the oxidizer which flows between the vanes.

Assessment of the four concepts indicated that the vane and coaxial element designs rank higher than the triplet concept. The triplet injector is hampered by more complex fabrication and manifolding and has a history of high face heat fluxes. As a result, it was not considered further. The strong points of the selected designs are in different areas. The vane injector is a novel concept which is uniquely suited for application in a low pressure system. It has performance, durability, ease-of-manufacture, and inlet-pressure-requirement advantages; however, it is relatively undeveloped. The coaxial element injector, on the other hand, has considerable industry experience at higher pressure levels and had been tested extensively by ALRC on a uni-element and full-scale segment basis at  $10.4 \text{ N/cm}^2$  (15 psia). Its primary weakness is its lower performance potential, which can be rectified by element modifications designed to enhance the mixing effectiveness of the basic element. These two concepts are complementary and were selected to present a technology program with balanced injector development risks.

## 2. Coaxial Element Injector

### a. Detailed Analysis and Design

#### (1) Design Description

The coaxial element injector was designed to meet the engine design requirements of Table I and the engine operating conditions shown in Table II. The injector consists of removable element assemblies configured to interface with an ALRC manifold assembly. This manifold assembly had been

### III,A, Injectors (cont.)

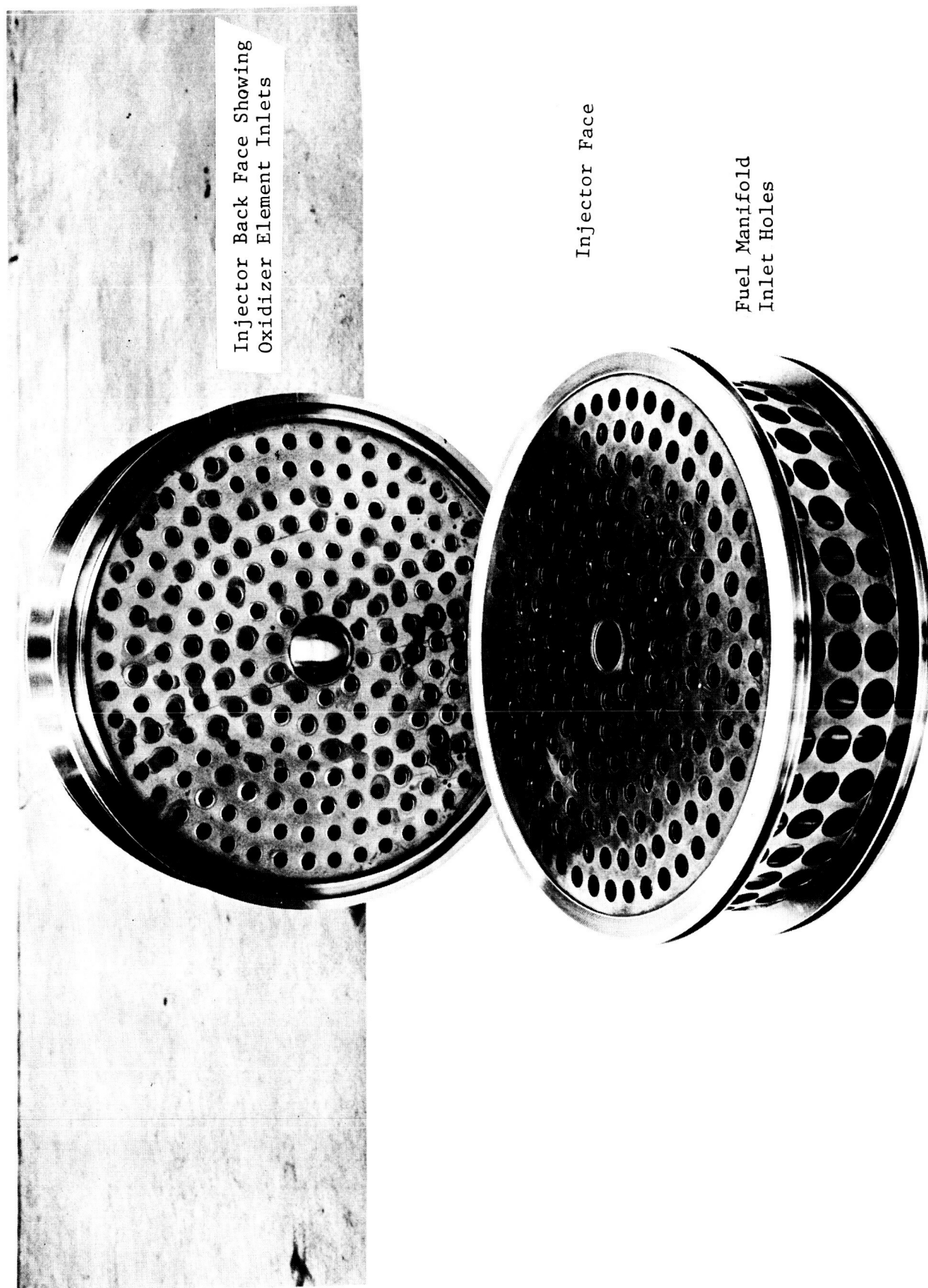
flow tested to provide uniform hydrogen and oxygen flow to the removable element assemblies and served as a fixed part of the test facility.

The coaxial element assembly shown in Figure III-1 consists of a nominal 38 cm (15-in.)-dia hydrogen inlet ring with external surfaces to interface and seal to the manifold assembly. Internal surfaces of the ring interface with the injector face plate and a back surface plate, which together interface with the element tubing to form the coaxial elements. Provisions for accommodating an igniter are incorporated in the center of the element assembly.

The element assembly shown in Figure III-1 contains 200 elements. Swirlers are installed in the oxygen tube inlets of the inboard elements and pressure balance caps in the inlets of the outboard elements. This combination of elements was selected for maximum performance and compatibility as a result of the element cold flow testing, which is discussed in a following section.

The elements were formed by brazing standard 1.27 cm (0.5-in.) OD, 0.051 cm (0.020-in.) wall thickness stainless steel tubing to a stainless steel backing plate and to a copper face plate. The copper face plate incorporates integral tabs to ensure alignment to form the hydrogen annulus. The element was designed to allow the face plate and back plate to be match drilled as an assembly to reduce tolerance accumulations.

The injector face was designed to be cooled by conduction, rather than transpiration. Heat is conducted from the uncooled areas of the face plate to the hydrogen annulus of each element where the heat is transferred to the primary hydrogen. The materials analyzed, both thermally and structurally, to determine the feasibility of this face cooling technique



Injector Back Face Showing  
Oxidizer Element Inlets

Injector Face

Fuel Manifold  
Inlet Holes

Figure III-1. Coaxial Element Injector

### III,A, Injectors (cont.)

are discussed in the thermal and structural analysis section.

#### (2) Element Quantity Optimization

The objective of the element quantity evaluation was to determine the effect of the number of elements on element size and hydrogen manifold flow velocities prior to recommending an element configuration for flow testing. Element quantities of from 50 to 1000 were evaluated assuming oxidizer and fuel injection velocities of 45.7 m/sec (150 ft/sec) and 427 m/sec (1400 ft/sec), respectively. Element geometry, hydrogen velocity between the elements, and face cooling were also considerations.

Element quantity was found to have little effect on hydrogen manifold cross velocity between the oxygen injection tubes as shown in Figure III-2. This trend results from selection of a fixed tube wall thickness to diameter ratio for this analysis.

Element quantity significantly affects element dimensions as shown in Figure III-3. Both the oxygen tube diameter and the hydrogen annulus width decrease rapidly up to 200 elements. Minimum oxygen tube diameter is desired to obtain small oxygen streams that are easier to mix. Maximum hydrogen annulus gap is desired to minimize the effect of tolerances on hydrogen distribution. Benefits of increased element quantity accrue slowly after 200 elements, and that quantity was selected for cold flow testing and thermal analysis.

#### (3) Cold Flow Testing

##### (a) Test Objectives

Injector performance inefficiency associated with gas-gas low chamber pressure APS thrusters is primarily a result of incomplete

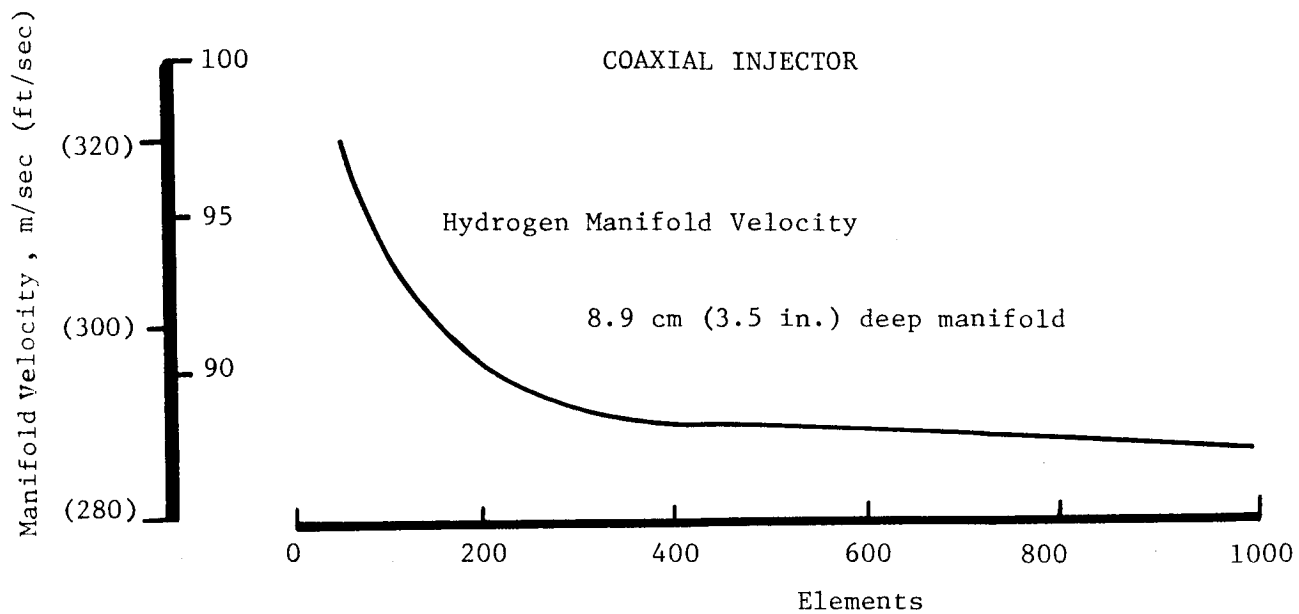


Figure III-2. Hydrogen Manifold Velocity vs Number of Elements

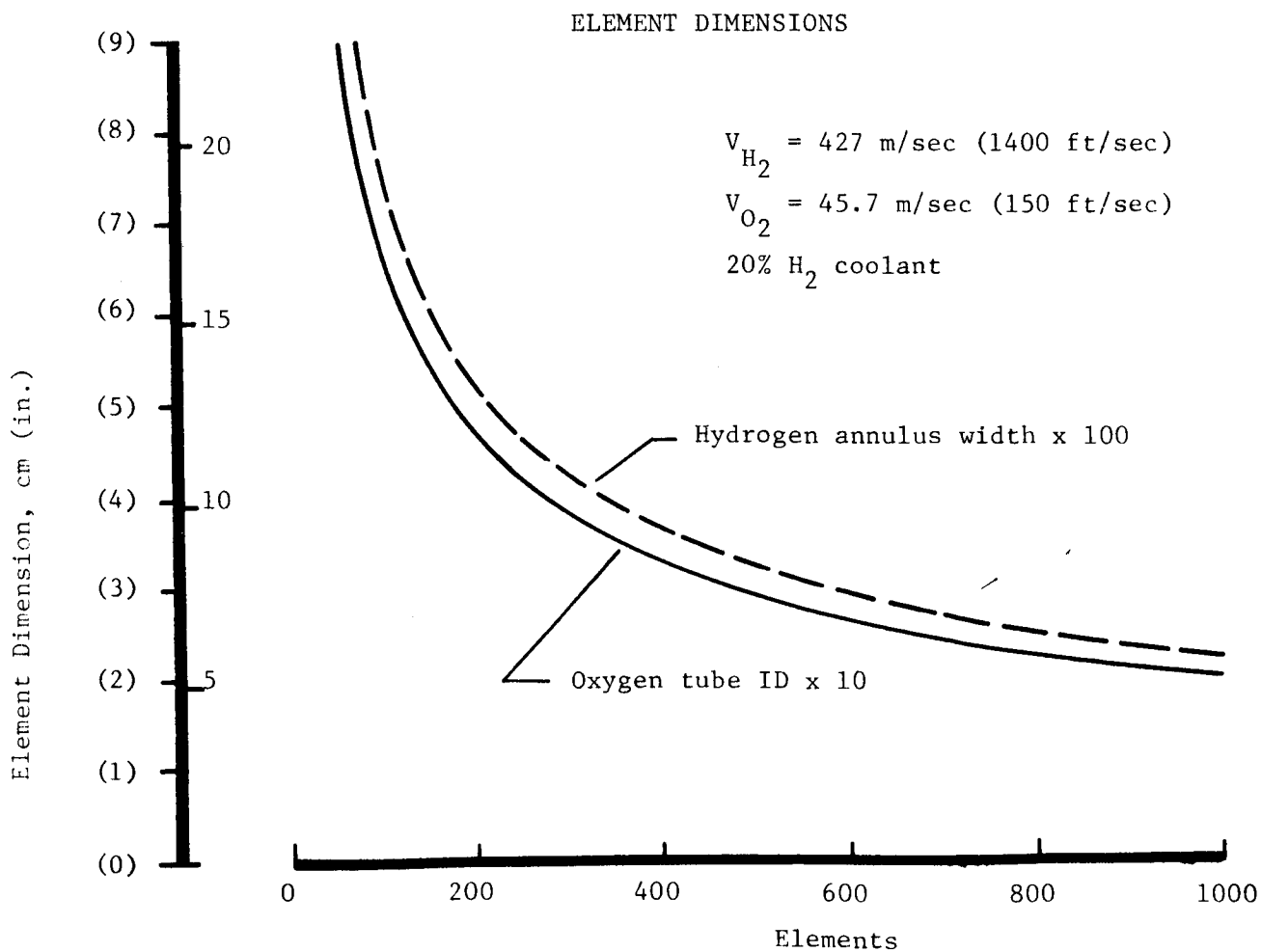
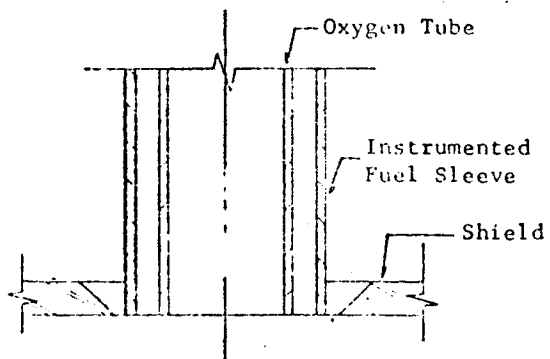
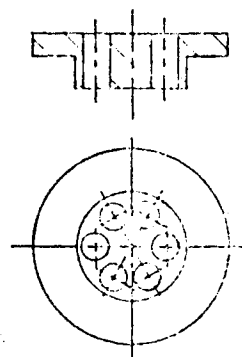


Figure III-3. Element Dimensions vs Number of Elements

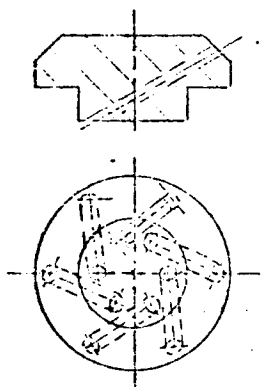




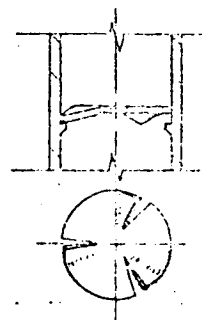
Showerhead Coaxial



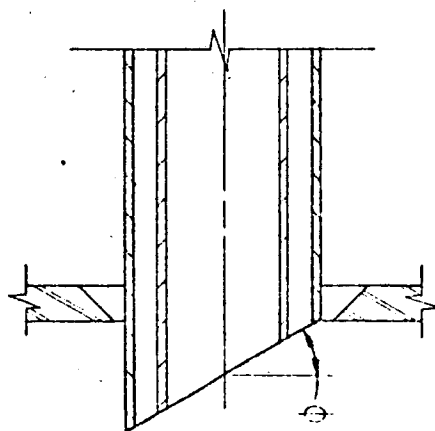
Oxygen  $\Delta P$  and  
Distribution Cap



Pneumatic Swirler



In-Line Swirler



Scarfed Element

Figure III-4. Coaxial Injector Cold Flow Element Configurations

### III,A, Injectors (cont.)

intra-element propellant mixing. Incomplete mixing results in the formation of zones of nonoptimum propellant mixture ratio, which causes an energy release loss. These propellant maldistributions may also produce undesirable oxidizer-rich chemical species adjacent to the chamber wall, causing local reaction with wall fuel coolant and increased chamber wall heating. The objective of the cold flow test program was to obtain gas-gas injector design data by obtaining a better understanding of gas-gas element injection and mixing characteristics for candidate injection element designs. These data, acquired at the laboratory level, provide the basis for injector element design.

#### (b) Cold Flow Test Hardware

The results obtained from the high pressure coaxial element cold flow test series, which preceded this activity, clearly showed the advantage of a swirler in the oxygen tube to augment mixing of the fuel and oxidizer. This background and the improved chamber wall thermal environment afforded by the use of scarfed coaxial elements (Ref III-A) provided the basic variations in coaxial element design selected for cold flow test evaluation.

Cold flow test hardware was fabricated to evaluate five types of coaxial elements. Figure III-4 shows the five coaxial element configurations in schematic format. A direct through-flow oxygen tube was used to obtain baseline mixing data. A flow restriction was installed in the oxygen tube inlet to provide additional pressure drop in a manner intended to promote mixing with the hydrogen. Three swirler designs were fabricated to determine the effect of two different swirl velocities on mixing and pressure drop and to evaluate a concept intended to reduce pressure loss. Two scarfed element designs were fabricated for testing with and without swirl to

---

Ref III-A. Gregory, J. W., "FLOX/Methane Pump-Fed Engine Technology Review," Paper 70-718, San Diego, Calif., June 1970.

TABLE III

## COAXIAL ELEMENT COLD FLOW TEST SUMMARY

Configurations		Measurement Positions		
<u>Oxygen Tube Inlet</u>	<u>Element Outlet</u>	<u>Length,</u> <u>cm (in.)</u>	<u>Rake</u> <u>Rotation,</u> <u>deg</u>	<u>Flow Test</u> <u>Mixture Ratio</u> <u>(O/F)</u>
1. Through Flow	a. zero recess	0 - 7.62 (3)	0 - 270	1.7 - 4.0
	b. 1.27 cm (0.5 in.) recess			2.0 - 4.0
	c. 2.54 cm (1.0-in.) recess			
2. Six-hole Pressure Drop Cap	a. zero recess			
	b. 1.27 cm (0.5-in.) recess			
	c. High $V_f$ annulus, 1.27 cm (0.5-in.) recess			
	d. 22.5° scarf, zero recess			
	e. 22.5° scarf, 1.27 cm (0.5-in.) recess			
	f. 45° scarf, zero recess			
	g. 45° scarf, zero recess			
3. 107 mps (350 fps) swirler	a. zero recess			
	b. 1.27 cm (0.5-in.) recess			
	c. High $V_f$ annulus, 1.27 cm (0.5-in.) recess			
4. 200 fps swirler	a. zero recess			2.0 - 4.0
	b. 1.27 cm (0.5-in.) recess			
	c. High $V_f$ annulus, 1.27 cm (0.5-in.) recess			
5. Inline swirler	a. zero recess			2.0 - 4.0
	b. 1.27 cm (0.5-in.) recess			
	c. 22.5° scarf, zero recess			
	d. 22.5° scarf, 1.27 cm (0.5-in.) recess			
	e. 45° scarf, zero recess			
	f. 45° scarf, 1.27 cm (0.5-in.) recess			

### III,A, Injectors (cont.)

determine the resultant propellant vectors and mixture ratio distribution. A final configuration was fabricated to evaluate the effect of hydrogen velocity on mixing.

The cold flow tests were conducted using heated 366°K (200°F) helium and cold 144°K (-200°F) nitrogen to simulate the densities of room temperature hydrogen and oxygen. These simulants were flowed through the candidate elements to atmospheric pressure (equivalent to chamber pressure) at flow rates selected to simulate the Mach number of the element flowing propellants. A temperature rake was used to measure the temperature profile of the combined flow at selected distances from the element outlet from which a local mixture ratio was inferred. A total pressure rake was used to define the mass flux profile across the element. The results were combined to identify the mass flux of each mixture ratio zone from which a mixing efficiency was calculated.

#### (c) Results

The coaxial element cold flow tests were conducted to acquire mixing and mass flux distribution data for 22 element configurations. The element configurations and test conditions are summarized in Table III.

The results of some of the cold flow tests are given in Figure III-5. This figure shows the mixing efficiency of six configurations over a range of mixture ratio. A recess length of 1.27 cm (0.5 in.) was chosen to allow inclusion of all configurations. The one-inch mixing length was found to best indicate element mixing characteristics; at longer mixing lengths, all elements show good mixing, preventing element differentiation. The most efficient mixing was achieved with the high velocity ratio oxygen swirl elements which showed improvement with increasing mixture ratio (angular

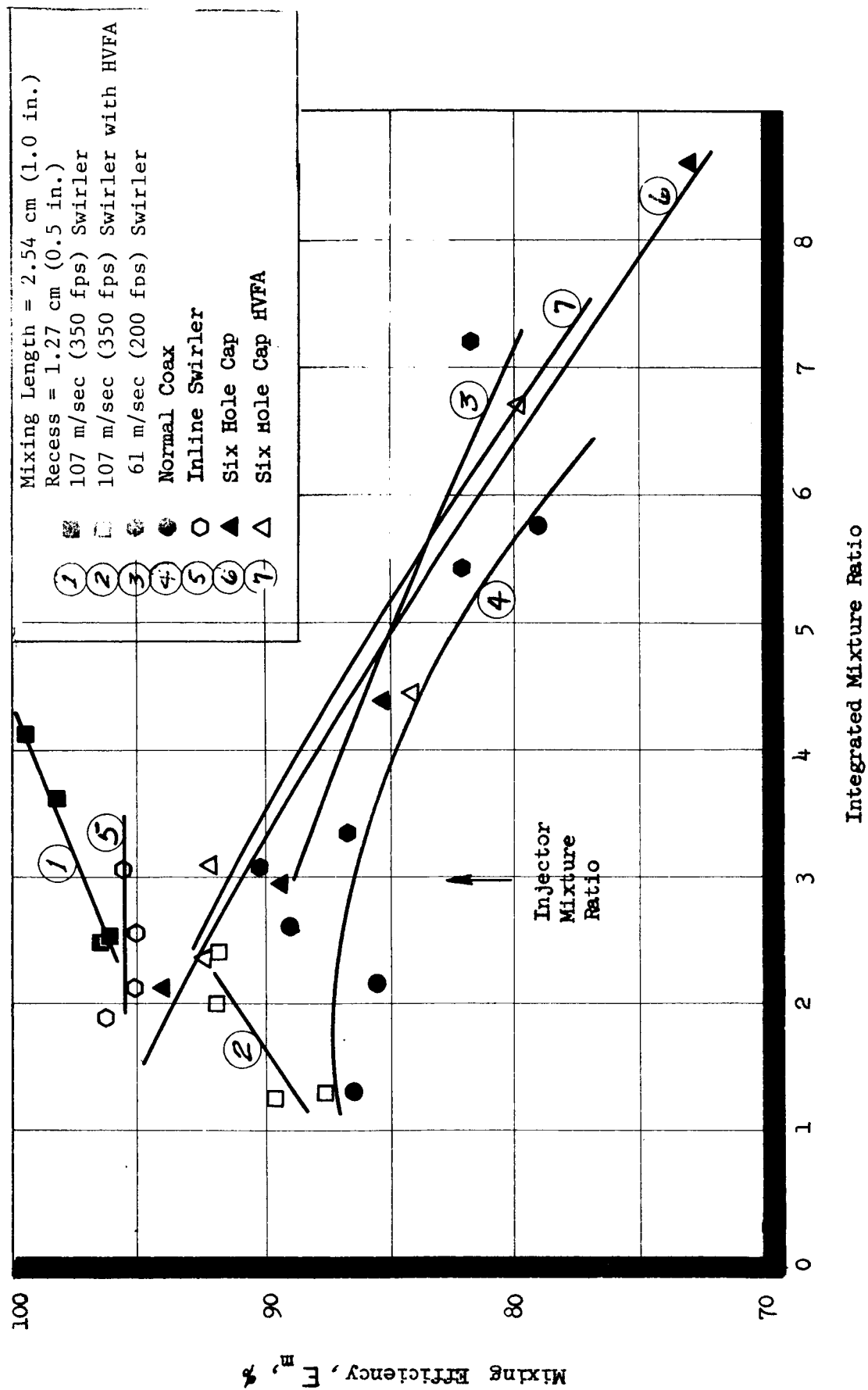


Figure III-5. Effect of Mixture Ratio on Coaxial Element Mixing Efficiency

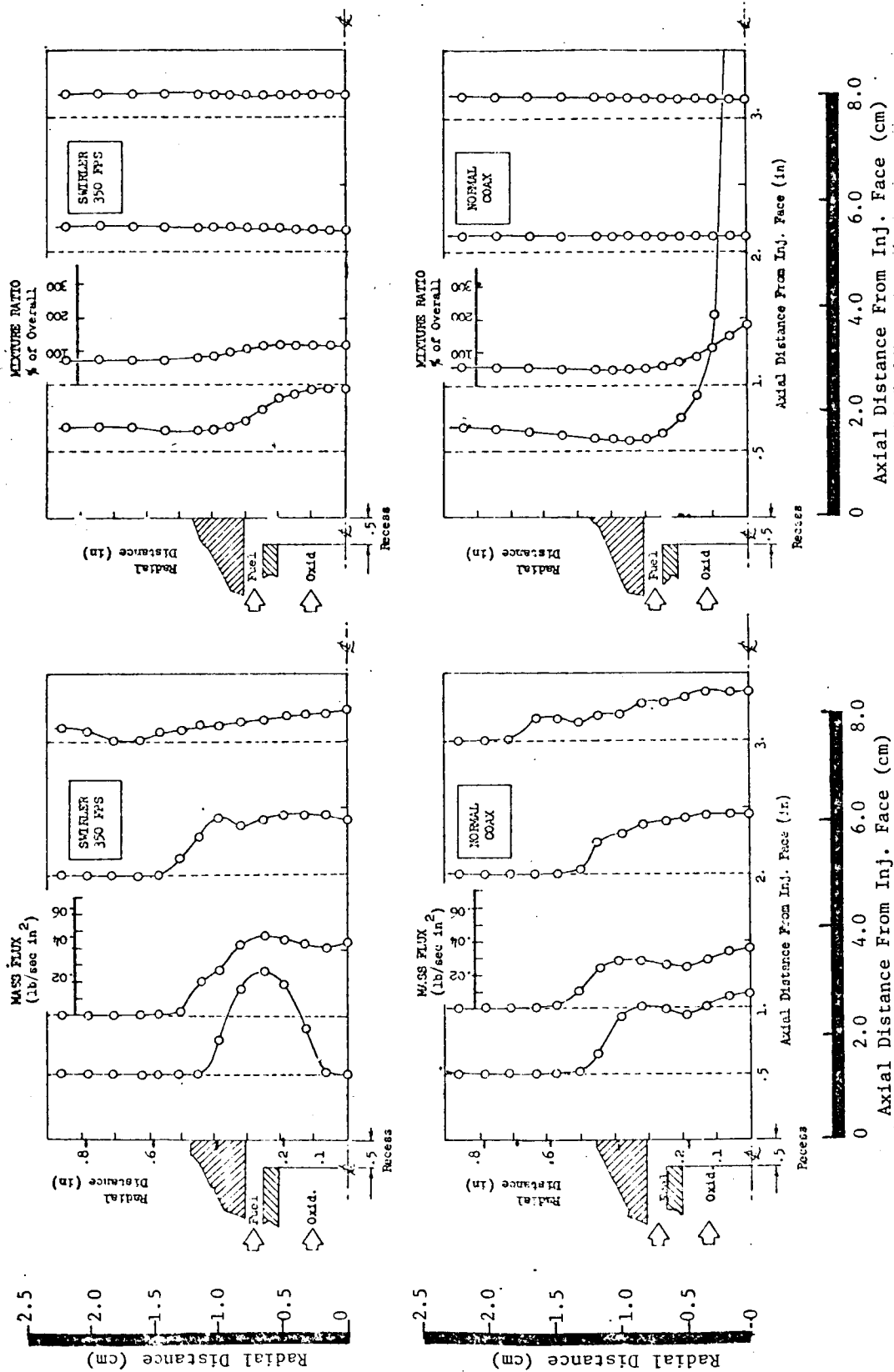


Figure III-6. Effect of Oxygen Swirl on Mass and Mixture Ratio Profiles

### III,A, Injectors (cont.)

momentum). The lower velocity 61 m/s (200 fps) swirler element was less efficient and approached the axial flow designs, indicating that the low swirl momentum was not sufficient to promote mixing. Momentum exchange designs (oxygen swirlers) tended to increase mixing with increased mixture ratio, which increases oxygen momentum. Shear mixing designs showed decreased mixing efficiency as the fuel-to-oxidizer velocity ratio was reduced by increasing mixture ratio.

The effect of the swirler on element mass and mixture ratio distribution is shown in Figure III-6. The mass flux and mixture ratio profiles measured at four axial stations for swirl and nonswirl coaxial elements are shown for comparison. The vertical scale indicates the fourteen radial locations where data to determine mass flux and mixture ratio were sampled.

The nonswirl coaxial element produced a high central oxidizer flux of  $0.00311 \text{ kg/cm}^2 \text{ sec}$  ( $0.05 \text{ lb/in.}^2\text{-sec}$ ) at a 1.27 cm (0.5-in.) mixing length, whereas the swirler element produced a central void with the mass concentrated adjacent to the fuel annulus. The nonswirl element showed a heavy oxidizer concentration in the center at the 1.27 cm (0.5-in.) mixing length. At a 2.54 cm (1.0-in.) mixing length, the swirler element exhibits only slight mixture ratio variations as a function of radius. The nonswirl element core mixture ratio at this station is about twice the swirler value. At the 5.1 cm (2.0-in.) mixing length, the mixture ratio profiles of both elements were uniform, indicating a completely mixed composition.

To determine the effect of shear velocity between oxidizer and fuel streams on mixing effectiveness, tests were conducted at two fuel velocities. The design point hydrogen velocity of 427 m/sec (1400 fps) and a higher velocity of 671 m/sec (2000 fps) were compared in tests with both

### III,A, Injectors (cont.)

swirling and nonswirling oxygen. Without swirl, a slight mixing improvement was found near the element outlet as shown in Figure III-7. The swirler design exhibited mixing improvement near the element outlet when tested with the higher velocity hydrogen. Little improvement was noted beyond a 2.54 cm (1.0-in.) mixing length.

Recessing the oxidizer tube within the fuel element increases the time of intimate fuel-to-oxidizer contact prior to expansion of the fuel outward from the oxidizer core. The change in mixing efficiency relative to a comparable flow test at zero recess for five elements is shown in Figure III-8. The shear mix element exhibited considerable mixing efficiency improvement with recess. The swirler elements were less improved by recess. With recess, the mixture ratio adjacent to the outer surface of the hydrogen annulus can become adverse. To evaluate the effect of oxygen tube recess on injector heating, tests were conducted with a thin-wall stainless steel sleeve used to form the outside surface of the hydrogen annulus. Thermocouples were installed on the sleeve and tests were conducted to determine steady-state sleeve temperature from which wall mixture ratio and a theoretical combustion temperature (assuming equilibrium reaction) were inferred. The hardware schematic and test results are shown in Figure III-9. These results show that swirl elements recessed 1.27 cm (0.5 in.) or nonswirl elements recessed 2.59 cm (1.0 in.) may result in undesirable face heating. Nonswirl elements recessed 1.27 cm (0.5 in.) do not appear to be particularly adverse.

The final test series evaluated the mixture ratio profile characteristics of scarfed injection elements. Biased mixture ratio profiles on elements adjacent to the chamber wall have been used to improve chamber compatibility as reported in Reference III-A. The documented tests were conducted with a swirl type element which was scarfed on the outlet end using liquid oxidizer and gaseous fuel. Flow tests were conducted to determine element mixture ratio profiles for scarfed elements without oxygen



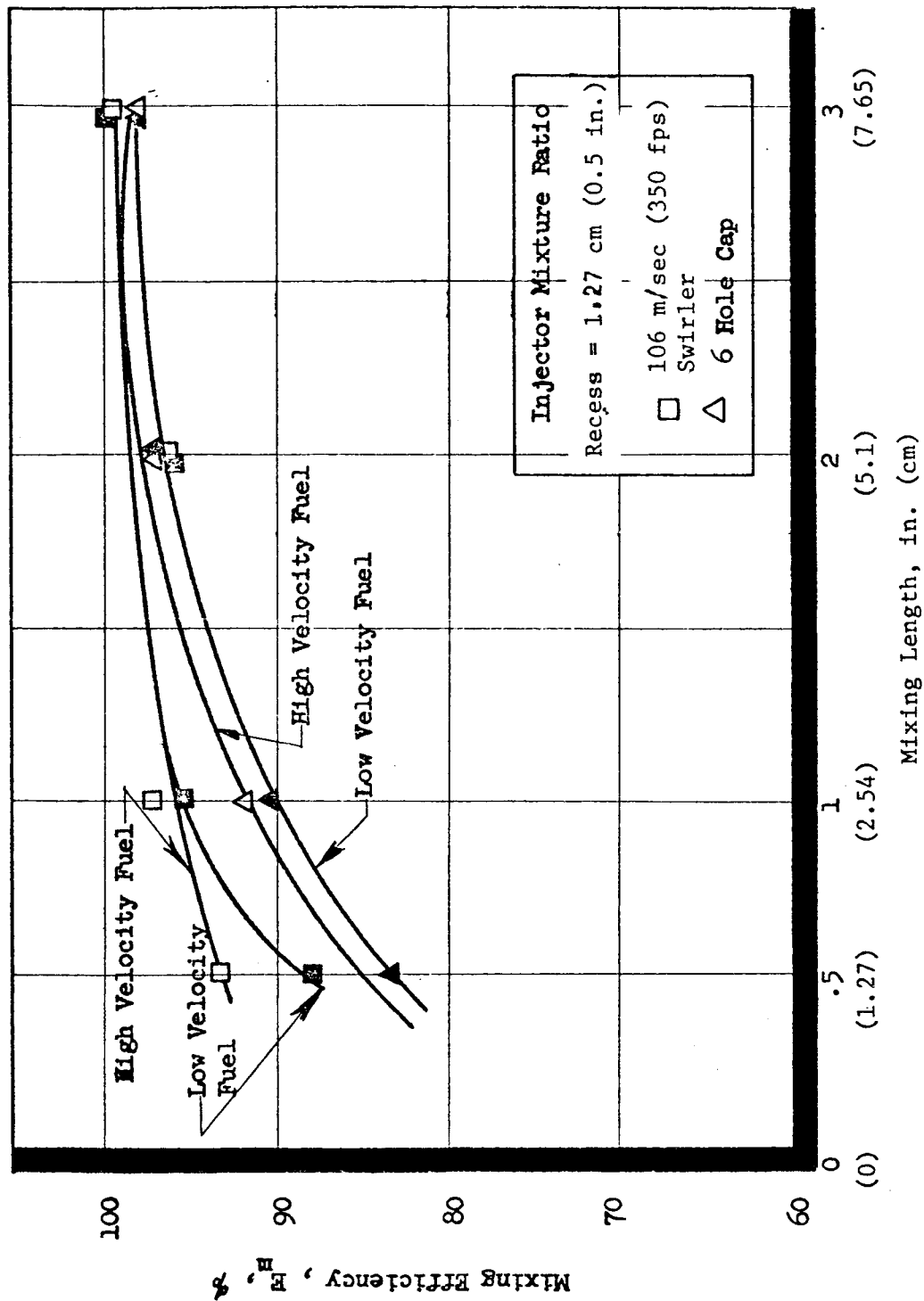


Figure III-7. Effect of Fuel Velocity on Coaxial Element Mixing Efficiency

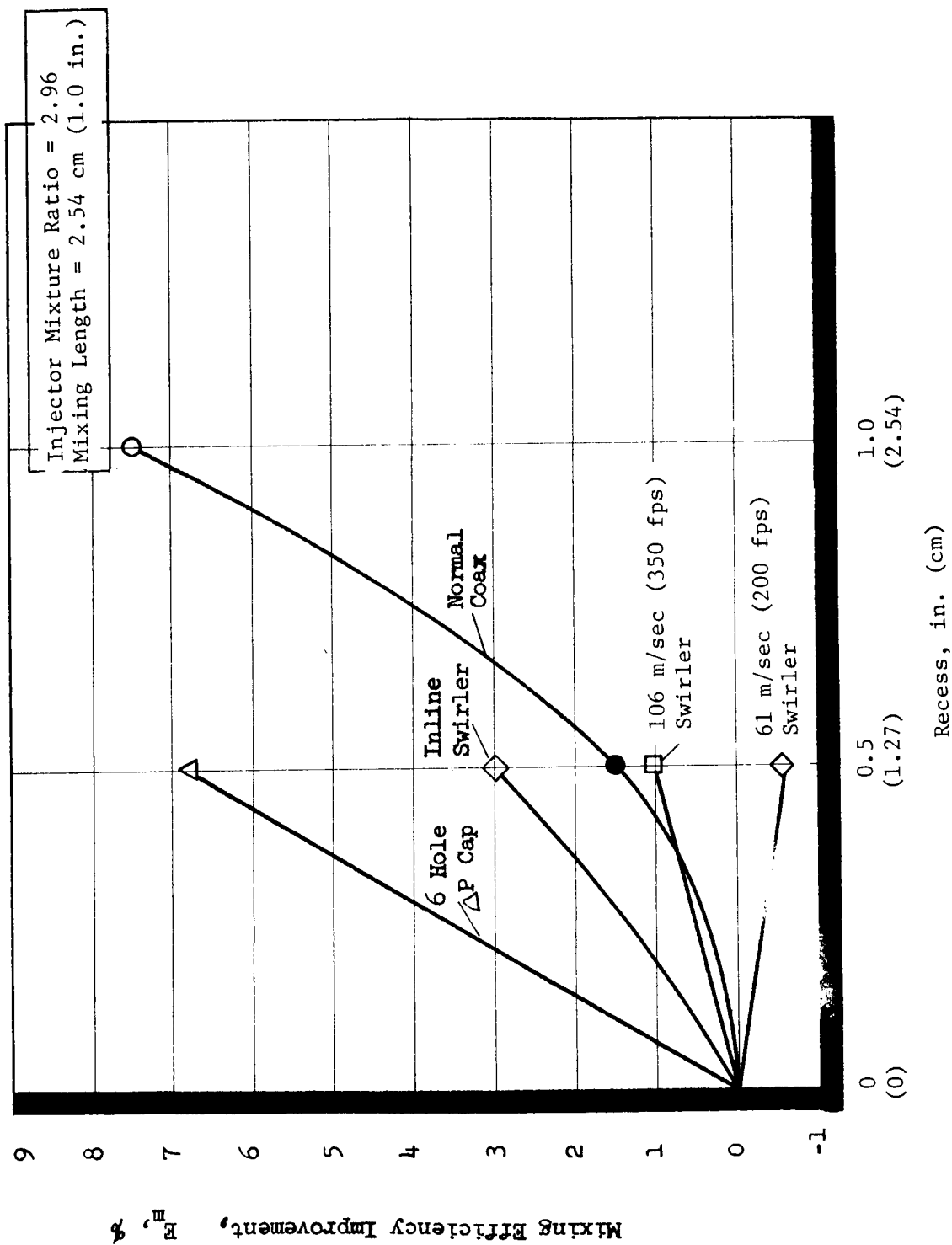


Figure III-8. Effect of Oxygen Post Recess on Coaxial Element Mixing Efficiency

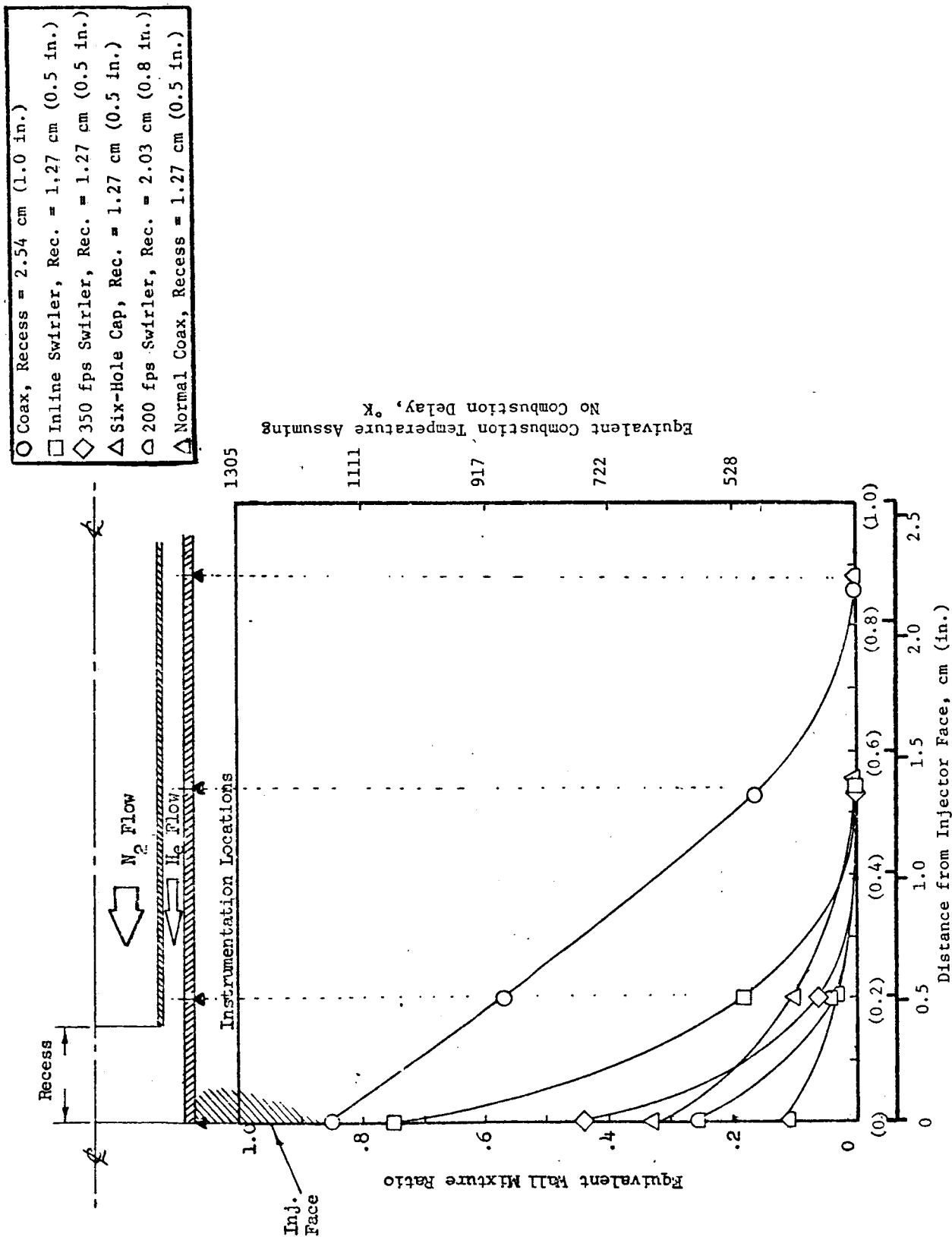


Figure III-9. Effect of Oxygen Post Recess on Hydrogen Annulus Mixture Ratio

### III,A, Injectors (cont.)

swirl, for baseline data, and with swirl. With nonswirling oxygen flow, the scarfed element exhibits near axisymmetric distribution with a distinct oxidizer core varying to a 0.2 mixture ratio periphery at a 2.54 cm (1.0 in.) mixing length. The mixture ratio profile is slightly elongated between the tip and root of the scarf as shown in Figure III-10. When the oxygen flow was rotated, the oxidizer element core was shifted away from the scarf tip by approximately  $135^\circ$  in the direction of oxidizer rotation as shown in Figure III-11. The lee side, at  $315^\circ$ , showed a zone of low mixture ratio. By orienting these elements  $45^\circ$  to a radial line, a desirable wall mixture ratio characteristic will be produced.

#### (d) Element Selection

Two element configurations were selected for the coaxial injector. A nonrecessed oxygen tube with a swirler in the inlet to promote mixing was used for all but the outer ring. The element selected for the outer ring was a recessed oxygen tube with a nonswirling pressure balance cap on the inlet. The selections were made to provide maximum mixing potential for the inboard elements with a minor compromise of mixing efficiency to improve the compatibility of the elements adjacent to the chamber wall.

The high rotational velocity oxygen swirler element clearly demonstrated the best mixing characteristics of all elements tested. The pressure drop required by this element was within the limits of the pressure schedule. An adverse feature of this concept was identified during hot fire testing of the high pressure coaxial element injector. Tests conducted with oxygen swirl resulted in high chamber heat fluxes near the injector, which were attributed to the more rapid mixing characteristics of this element. When the swirler was removed, the forward

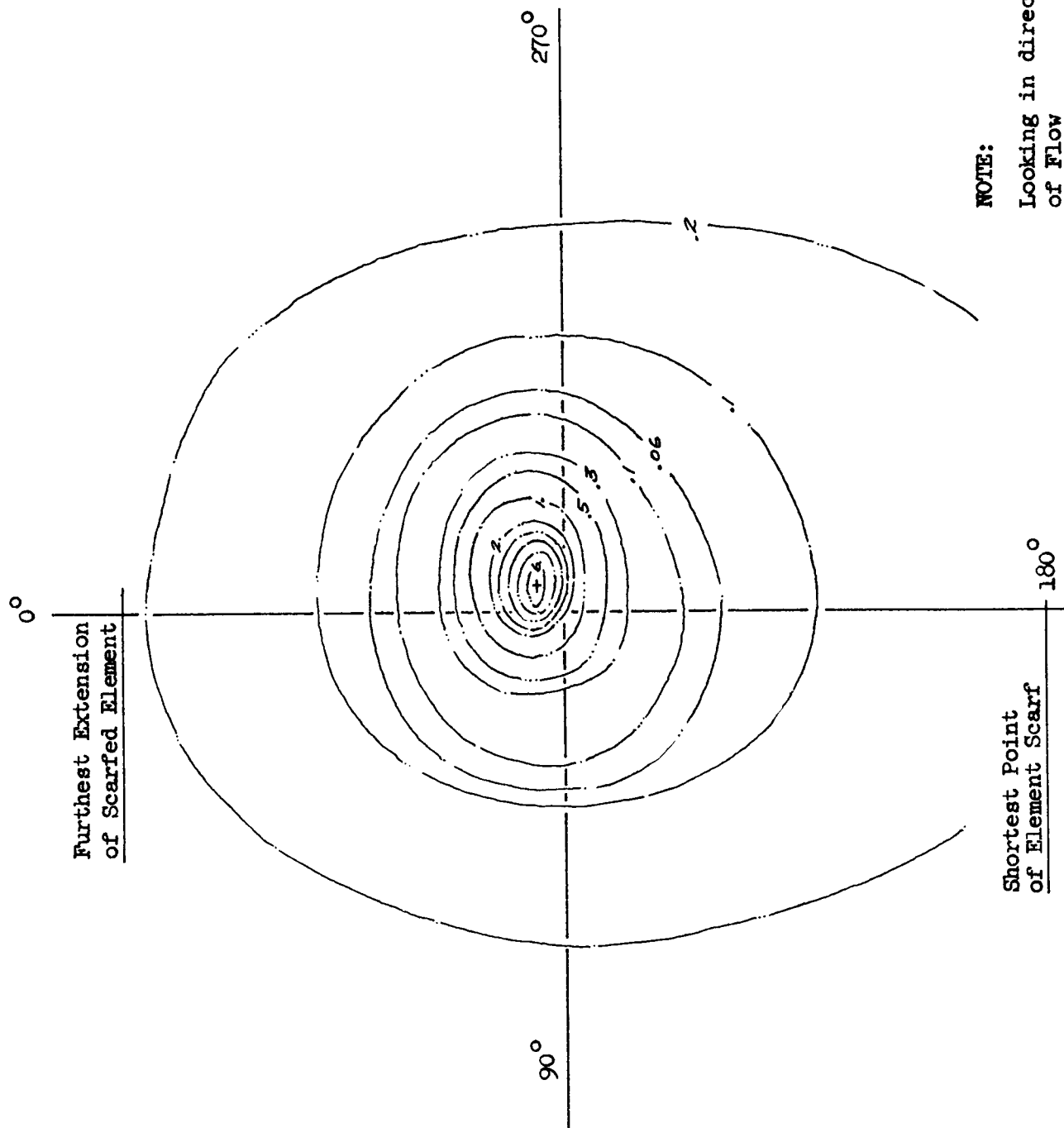


Figure III-10. Mixture Ratio Distribution of Scarfed Element with Nonswirling Oxygen

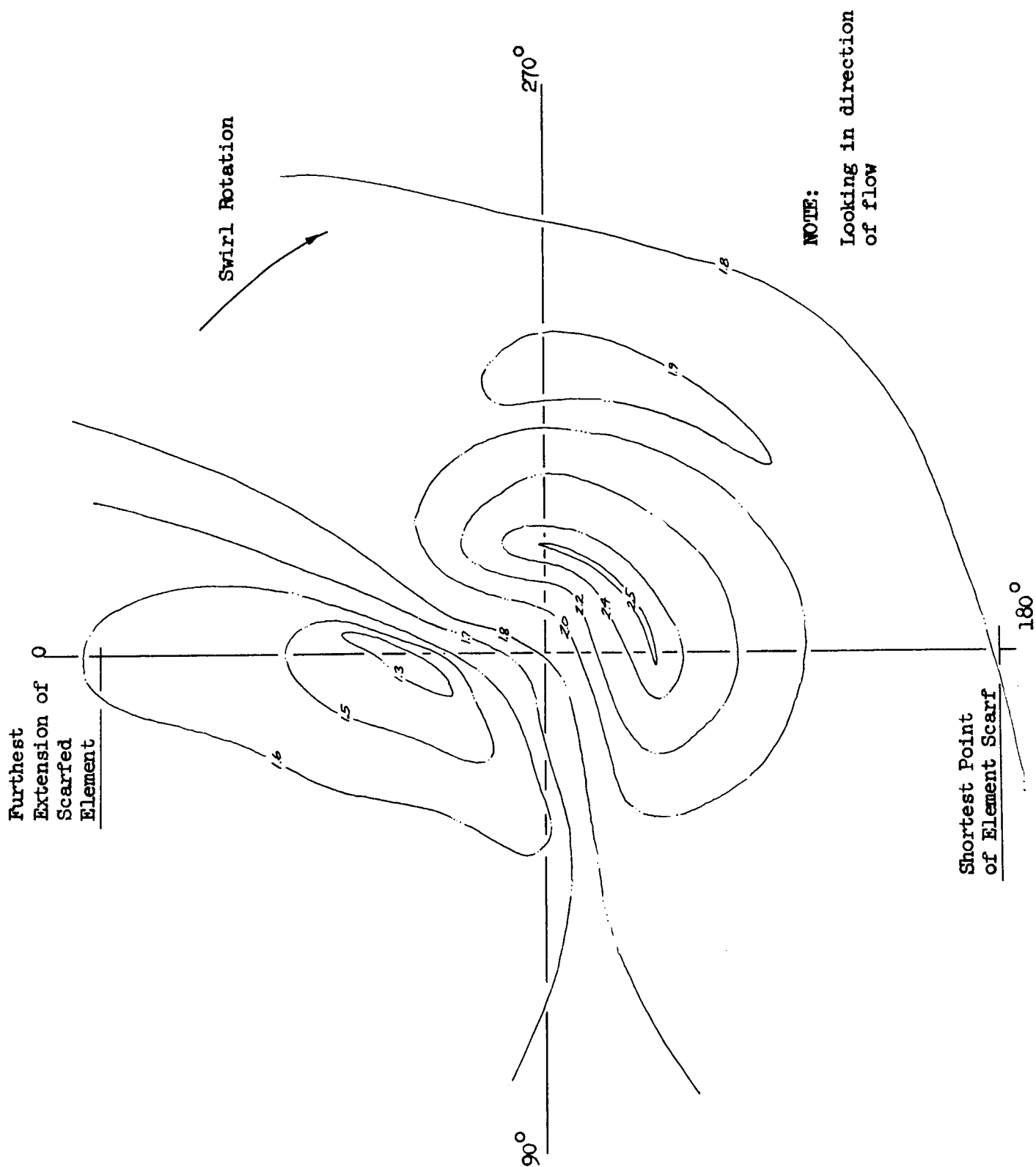


Figure III-11. Mixture Ratio Distribution of Scarfed Element with Swirling Oxygen

### III,A, Injectors (cont.)

chamber heat flux was reduced but the heat fluxes toward the throat increased because of the combustion delay resulting from the slower initial mixing. The higher heat fluxes near the throat station was considered to be less adverse for chamber cooling and, therefore, nonswirl elements were selected for the element ring adjacent to the chamber wall. The outlet end of the oxygen tube was designed to be even (or flush) with the injector face to ensure that adverse mixture ratios and combustion did not cause injector face heating.

The nonswirl, recessed element selected for the outer ring incorporated a pressure balance cap with six holes for uniform oxygen distribution at the exit plane. A recess of 1.27 cm (0.5 in.) ( $\approx 1 L/D$ ) was found to increase mixing potential by nearly 7% over the nonrecessed configuration. Nonswirl element heating due to recess was found to be less severe than with oxygen swirl.

#### (4) Thermal and Structural Analysis

Thermal and structural analyses of the coaxial element assembly were conducted to verify the adequacy of the design to withstand pressure loads, to evaluate materials, to estimate the temperature of the conductively cooled face, and to predict the cyclic life of the assembly.

The heat transfer from the uncooled areas of the injector face to the hydrogen flowing through each element depends upon the conductivity and the thickness of the face material. Four materials were analyzed over a range of face thicknesses to determine the feasibility of this cooling technique. The steady-state temperature profiles predicted for the corner points of the nodal network used for this analysis are shown in Figure III-12. Calculated temperatures ranged from 450°K (350°F) to 505°K (550°F) for a 0.63 cm (0.25-in.)-thick face plate. These temperatures were well within the thermal limits of the materials.

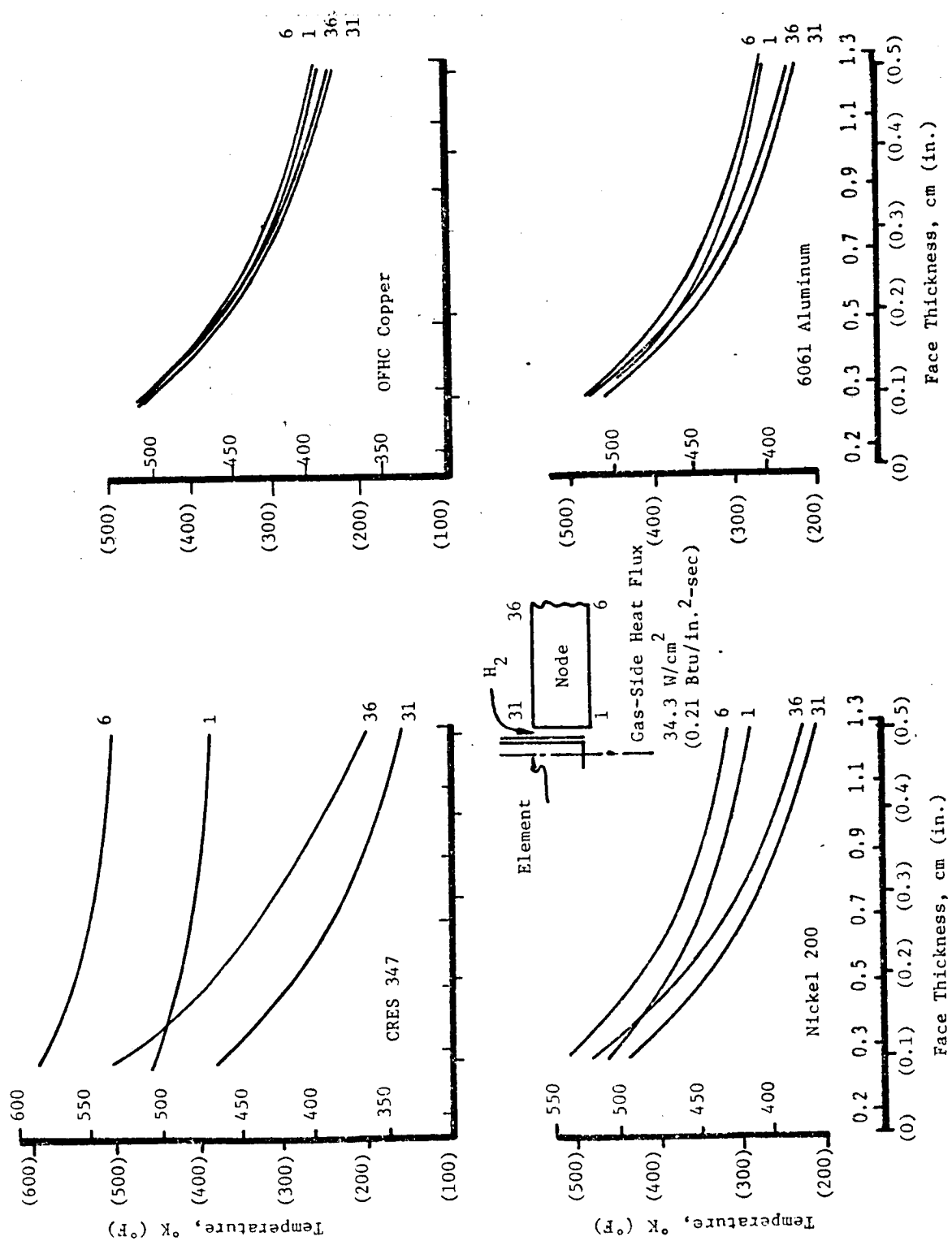


Figure III-12. Predicted Coaxial Element Injector Face Temperatures



### III,A, Injectors (cont.)

The results of the thermal analyses were used for a thermal stress analysis to predict the fatigue life for the candidate injector face materials. This analysis considered both the thermal gradient across the injector face thickness and the gradient between the injector face and the external ring to which the face plate is attached. The external ring was assumed to remain at ambient temperature. Predicted cycle life for the four candidate materials is shown on Table IV. OFHC copper was selected for this application because of the good fatigue characteristics and the tolerance to local heating due to the high conductivity.

#### b. Fabrication

Two coaxial injector element assemblies and components for a third were fabricated. A face view and a back view of the completed units are shown in Figure III-1.

The outer housing for the assembly was machined from a 347 stainless steel ring forging and the inner hub for the igniter was machined from tubing. The injector face and back plates were match drilled to interface with the element tubing. The face plate was then end milled to form the hydrogen annulus using the tubing hole as a pilot for proper alignment and finally broached to provide the hydrogen flow area and alignment tabs. The tubing for the elements was cut to length.

The components were assembled and a Nicro braze powder and cement mixture was applied. The braze operations were successfully completed for both units.

#### c. Coaxial Injector Manifold Distribution Tests

Flow tests were conducted to determine the distribution characteristics of the 200-element coaxial injector assembly when installed in the

TABLE IV

INJECTOR FACE FATIGUE LIFE DESIGN PREDICTIONS

<u>Material</u>	<u>Fatigue Life Cycles</u>	<u>Comments</u>
OFHC Copper	$1.5 \times 10^5$	Very low gradient stresses
Nickel 200	$2.0 \times 10^5$	Higher gradients, better High cycle fatigue resistance
Aluminum 6061-T6	$4.0 \times 10^4$	Lower gradients than nickel but is more fully restrained by outer ring due to low modulus
CRES 347	$1.0 \times 10^4$	Lowest fatigue life due to large gradients

### III,A, Injectors (cont.)

ALRC-owned hydrogen and oxygen manifolds. Nitrogen was flowed through the oxygen side and then the hydrogen side of the injector at a flow rate selected to simulate the Mach numbers of rated oxygen and hydrogen flow.

The flow from selected elements was measured by a gas flow meter connected to pickup probes which collected the flow from individual elements. The probes were designed to collect the flow with minimum pressure loss and without allowing recirculation into the opposite propellant manifold.

The objectives of these tests were to identify adverse inlet, manifold or element assembly induced flow conditions and, further, to determine the mixture ratio of each element in the outer ring of the injector for comparison with the results of the scheduled compatibility tests.

The technique used for these tests provided good results with the oxygen side of the element where the sampling probe was fitted around the oxygen tube, providing good sealing and alignment. The hydrogen sampling probe was not as easily aligned or sealed. Ice formed on the injector face during hydrogen circuit flow testing, which also interfered with proper alignment and interfacing of the probe. Flow from 79 elements was sampled. Each of the outer ring elements and every fifth inner ring element were used to define overall manifold distribution characteristics and expected chamber wall mixture ratio.

The outer ring of 47 elements showed an oxygen flow deviation of  $\pm 3.7\%$  with no indication of an adverse effect resulting from the location of the inlet. Fuel flow distribution for these same elements was within  $\pm 10.5\%$ , again with no adverse inlet effects. Figure III-13 shows the mixture ratio profiles for each ring of elements calculated from the cold flow data.

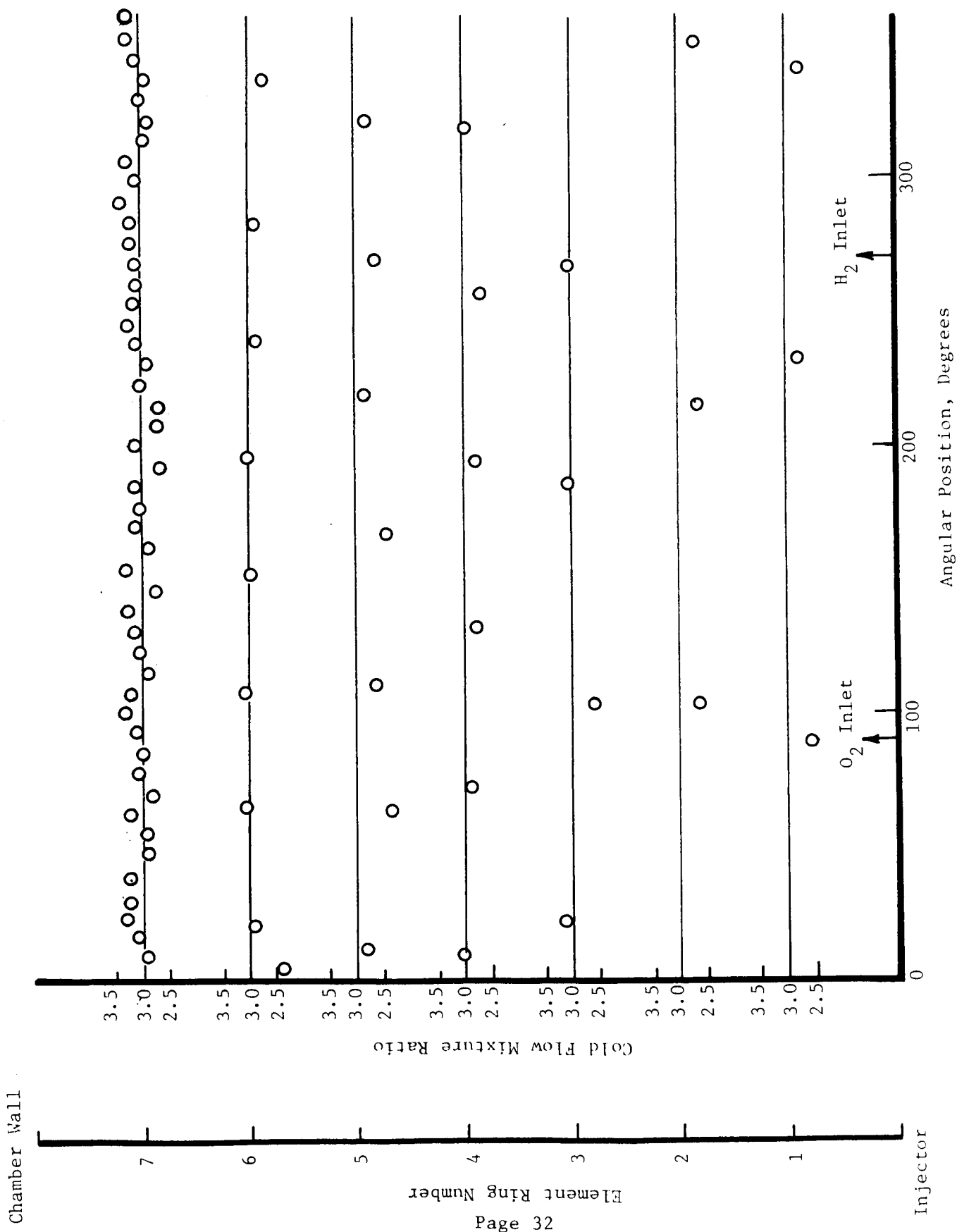


Figure III-13. Mixture Ratio Profiles Based on Cold Flow Data

### III,A, Injectors (cont.)

#### 3. Vaned Injector

##### a. Detailed Design and Analysis

##### (1) Design Description

Precontract Aerojet-sponsored evaluation of coaxial elements for low  $P_c$   $O_2/H_2$  injectors included tests of a design in which an axial flow oxygen stream was impinged by discrete hydrogen jets in a confined space. Single element test hot fire results demonstrated superior  $c^*$  performance for this design when compared to more conventional coaxial elements. Studies showed this propellant mixing concept to be especially suited to an injector design which uses vanes to distribute hydrogen across the injector face. The vanes are spaced to provide passages allowing sheets of oxygen to flow between the vanes where discrete streams of hydrogen, emanating from orifices in the vanes, penetrate and mix with the oxygen.

On this contract a low pressure vaned injector was designed to meet the engine design requirements of Table I and the engine operating conditions shown in Table II. The vaned element assembly interfaces with the ALRC manifold assembly, as did the coaxial element assembly.

The vaned element assembly shown in Figure III-14 consists of a nominal 38 cm (15-in.)-dia hydrogen inlet ring with external surfaces sized to interface and seal to the manifold assembly. The ring is machined to provide attachment surfaces for the formed radial vanes through which hydrogen flows radially inward across the injector face. Two vane lengths were used: long vanes extend to the outside of the igniter hub, while alternate vanes are shorter to provide adequate oxygen flow area. Hydrogen enters the combustion chamber through orifices near the trailing edge of the vanes. Oxygen flows through a distribution plate located on the manifold (or back)



### III,A, Injectors (cont.)

side of the vanes and then between the vanes. The vanes are positioned uniformly by spacers to ensure uniform oxygen flow distribution. A 60-vane design was selected to provide for a low 61 m/sec (200 ft/sec maximum) hydrogen velocity through the vanes and a low 46 m/sec (150 ft/sec maximum) oxygen injection velocity.

#### (2) Vaned Element Cold Flow Testing

As described earlier, oxygen flows between the radial vanes where discrete streams of hydrogen emanate from orifices in the vanes to penetrate and mix with the oxygen. A four-series cold flow test program was conducted to optimize oxygen and hydrogen injection for best mixing efficiency and to determine manifold distribution characteristics. Table V summarizes the hardware configurations, test parameters, and results.

Test Series I evaluated the effect of varying hole size, injection velocities, recess depth, and oxygen flow passage width on the penetration of the hydrogen jet and mixing of the hydrogen and oxygen simulants. The tester consisted of a fuel hole injecting perpendicular to an oxidizer stream representative of the between-vane flow passage. Optical glass sides contained the mixing streams and shadowgraphs were made to observe the density gradients. A nonreacting mixture of room temperature helium for fuel and nitrogen for the oxidizer were used to simulate the momentum ratio of hydrogen and oxygen. Figure III-15 is typical of the data acquired. Nitrogen flow is penetrated by the lower molecular weight helium flow, producing large density gradients near the point of injection. At the extreme left of the figure, a near homogeneous condition prevails, indicating a uniform mixture.

TABLE V

## VANED ELEMENT COLD FLOW TEST SUMMARY

Series	Type of Test	Test No.	Injection Element		Fuel Vel. fps	Oxidizer Vel. fps	Test Result		Series Result
			Dia.	No.			Wall Penetration	Mixing	
IA	Shadowgraph - Jet Penetration and Recess Evaluation	1	.060	1	.1	500	80	Complete	Mechanical
		2				250		Complete	Mechanical
		3				500		None	Good
		4				0		Slight	Good
		5						No fuel flow	-
IB	Shadowgraph - Jet Penetration and Recess Evaluation	6	.060	1	.1	500	80	None	Improved
		7			1000		None	Improved	1. Penetration Excessive Above 1000 fps
		8				96		Reduced	2. Oxidizer velocity increase has small effect
		9				112		Reduced	3. Good mixing requires fuel velocities above 500 fps
		10				64		Heavy	
		11			500		None	Good	
		12				96		Less	
		13					Repeat of # 12	Good	
		14					Repeat of # 12		
		15			1500	80	Slight	Excellent	
		16				96	No Change	No Change	
		17			2000	112	Less	Less	
		18					Heavy	Mechanical	
		19				80	No Change	No Change	
		20				96	No Change	No Change	
IC	Shadowgraph - Jet Penetration and Recess Evaluation	21	.060	1	.3	500	80	None	Excellent
		22			1000		Complete	Mechanical	1. Recess Improves Mixing
		23				96	Reduced	Reduced	2. At recess above .5 inch produces opposite wall attachment
		24				112	None	None	
		25			500	80	None	Excellent	
		26			1000		Slight	Excellent	
		27				96	Reduced	Excellent	
		28				112	Reduced	Reduced	
		29			500		None	Good	
		30				80	Slight	Good	
		31			1000		Slight	Mechanical	
		32				96	Slight	Mechanical	
		33				112	Slight	Mechanical	
		34			500		Homogeneous	Excellent	
ID	Shadowgraph - Jet Penetration and Recess Evaluation	35	.089	1	.1	225	64	None	Poor
		36				80		None	Less
		37				96		None	Less
		38				112		None	Very poor
		39			500		None	Good	
		40				96		Good	
		41				80		Improved	
		42			1000		None	Excellent	
		43				96	Slight	Excellent	
		44			1500	80	Less	Less	
		45				96	Heavy	Mechanical	
		46			2000		Complete	Reduced	



TABLE V (cont.)

Series	Type of Test	Test No.	Injection Element		Fuel Vel. fps Me	Oxidizer Vel. fps Me	Test Result		Series Results
			Dia.	No.			Wall Penetration	Mixing	
ID (Cont.)	Shadowgraph - Jet Penetration and Recess Evaluation	47	.089	1		96	Reduced	Mechanical	
		48			1000	80	None	Excellent	
		49			1500		Complete	Mechanical	
		50				96	Reduced	Mechanical	
		51			500		None	Excellent	
		52				80	None	Homogeneous	
		53			1000		None	Homogeneous	
		54			1500		Slight	Slight Mechanical	
		55			2000		Heavy	Mechanical	
		56					Very Heavy	Mechanical	
		57				96	Heavy	Mechanical	
IE	Shadowgraph - Jet Penetration and Recess Evaluation	58	.125	1	.2	80	None	Good	1. D = .125 Improves Mixing
		59			500		Slight	Excellent	2. Higher Penetration
		60			1000		Heavier	Excellent	3. Recess Restriction @ .5 inch
		61			1500		Less	Excellent	
		62				96	None	Excellent	
		63			1000	112	Reduced	Excellent	
		64			500	80	None	Good	
		65		.5	1000		Slight	Excellent	
		66				96	None	Excellent	
		67		1.0	500	80	None	Excellent	
		68			250		None	Good	
		69				96	None	Good	
		70			1000	112	Poor	Poor	
		71				80	Slight	Excellent	
		72					Poor	Excellent	
		73			250	96	Poor	Poor	
IF	Shadowgraph - Jet Penetration and Recess Evaluation	74	.055x.108	1	.1	.2	None	Excellent	1. Excellent mixing and Penetration
		75			500	80	Less	Good	2. Higher fuel velocities allowed
		76				96	Less	Poor	
		77			1000	112	None	Excellent	
		78				96	None	Excellent	
		79				112	None	Excellent	
		80			1500	80	Slight	Excellent	
		81				96	None	Excellent	
		82			2000	112	None	Excellent	
		83				80	Heavy	Mechanical	
		84				96	Slight	Mechanical	
		85				112	None	Excellent	
II	Shadowgraph - Jet Spreading Distance	86	.125	3	.1	.2	-	Excellent	Complete spreading in recess distance
		87			500	80	-	Excellent	90% spreading in recess distance
		88			1500	250	-	Excellent	90% spreading in recess distance
		89			500	80	-	Excellent	Complete spreading in recess distance
		90				96	-	Excellent	Complete spreading in recess distance
		91				112	-	Excellent	90% spreading in recess distance
		92			250		-	Excellent	90% spreading in recess distance
		93			750		-	Excellent	40% spreading in recess distance
		94			750	80	-	Excellent	50% spreading in recess distance
		95			1500		-	Excellent	70% spreading in recess distance

TABLE V (cont.)

Series	Type of Test	Test No.	Injection Element		Fuel Vel. fps He	Oxidizer Vel. fps N2	Test Result		Series Results
			Dia.	No.			Gap	Recess	
III A.	Vane Flow - Tufts	96	.125	32	.475	.2			Poor Resolution on Tufts
B.	Vane Flow - Pitot Tube	97							Excellent Flow Distribution. Low flow on holes 21, & 30. No flow on # 32
C.	Vane Flow - Ink	98							Excellent Internal Aerodynamic flow Profile
D.	Vane Flow - Injector	99							Fuel Velocity Normal to Oxidizer Flow Direction
E.	Angle	100							Fuel Velocity Vector Slight Cented in Direction of Radial Vane Manifold Flow

Test No. 11

$D_{H_2} = 0.154 \text{ cm (0.060 in.)}$

$V_{H_2} = 153 \text{ m/s (500 fps)}$

$V_{O_2} = 29 \text{ m/s (96 fps)}$

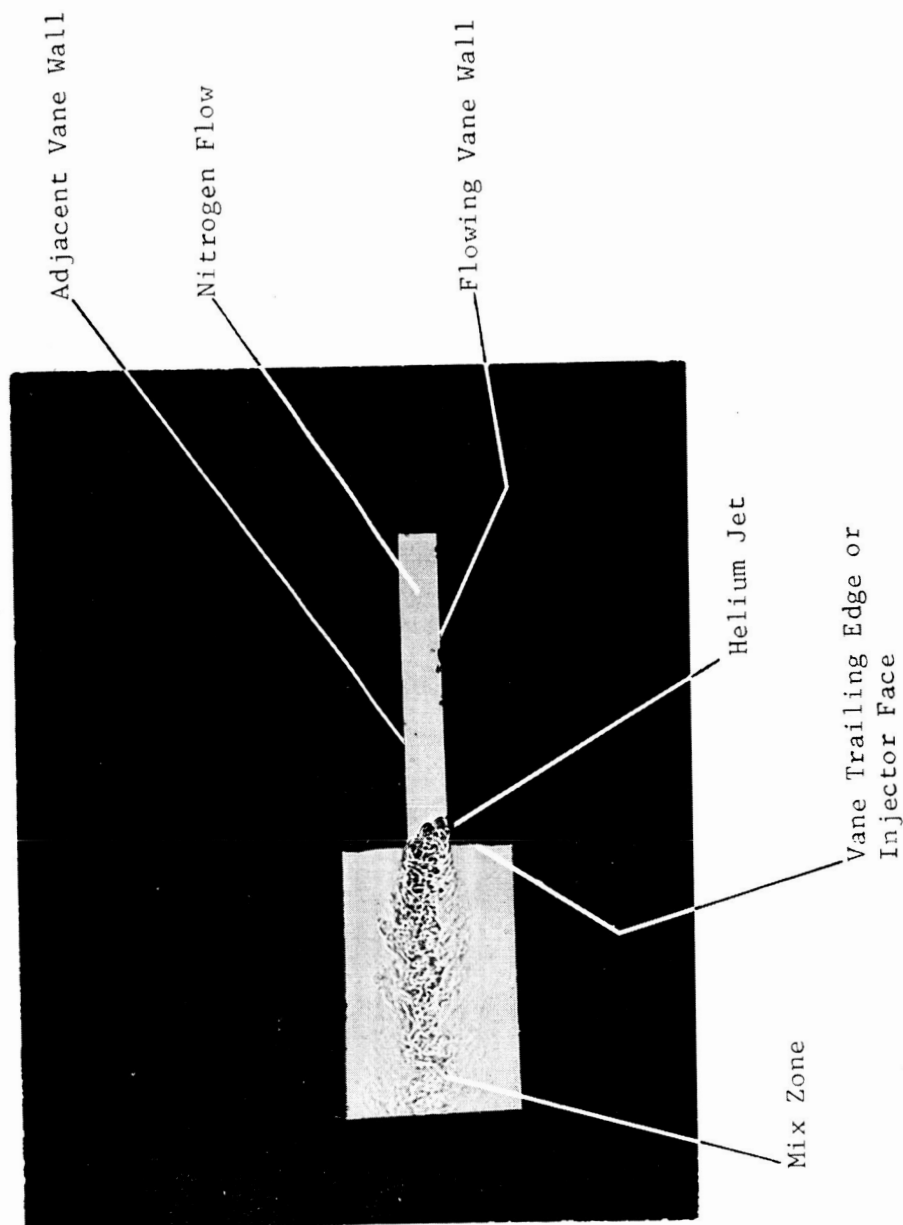


Figure III-15. Typical Shadowgraph

### III,A, Injectors (cont.)

The first subgroup of tests was conducted to evaluate the depth of penetration of a hydrogen jet into an oxygen sheet. A fuel orifice diameter of 0.152 cm (0.060 in.) with an injection velocity of 152 m/sec (500 ft/sec) and an oxygen passage width of 0.25 cm (0.10 in.) were selected for the baseline tests. The results of this test are shown in Figure III-16. The uniform density gradient 1.27 cm (0.5 in.) from the trailing edge of the vane indicates good mixing was achieved. The hydrogen simulant penetrated the oxygen sheet and impinged upon the far side vane wall, and thereby mechanically augmented the mixing. The oxidizer velocity was increased to 49 m/sec (160 fps) and the fuel velocity reduced to 76 m/sec (250 fps) for the next test. The penetration of the hydrogen was reduced, as was the mixing effectiveness. It was concluded from this five-test series that a vane gap greater than .25 cm (0.1 in.) would be required to preclude complete jet penetration to achieve good mixing.

The second subgroup of 15 tests evaluated the jet penetration characteristics for a 0.51 cm (0.2-in.) vane spacing over a range of fuel velocity from 152 to 610 m/sec (500 to 2000 fps). The mixing was improved as the fuel velocity was increased; however, undesirable penetration and far wall attachment was observed at fuel velocities above 301 m/sec (1000 fps). At a fuel velocity of 150 m/sec (500 fps), an unmixed helium core was observed. The effect of helium velocity on penetration and mixing for Tests 8 and 20 is shown in Figure III-17. A fuel velocity of 301 m/sec (1000 fps) just penetrated the oxygen, whereas the 601 m/sec (2000 fps) fuel penetrated and attached to the far wall.

The effect of recess was evaluated by injecting the fuel stream at distances from 0.76 cm (0.3 in.) to 2.54 (1.0 in.) along the direction of oxidizer flow in Tests 21 through 34. Mixing improvement was

Vane Spacing - 0.254 cm (0.1 in.)

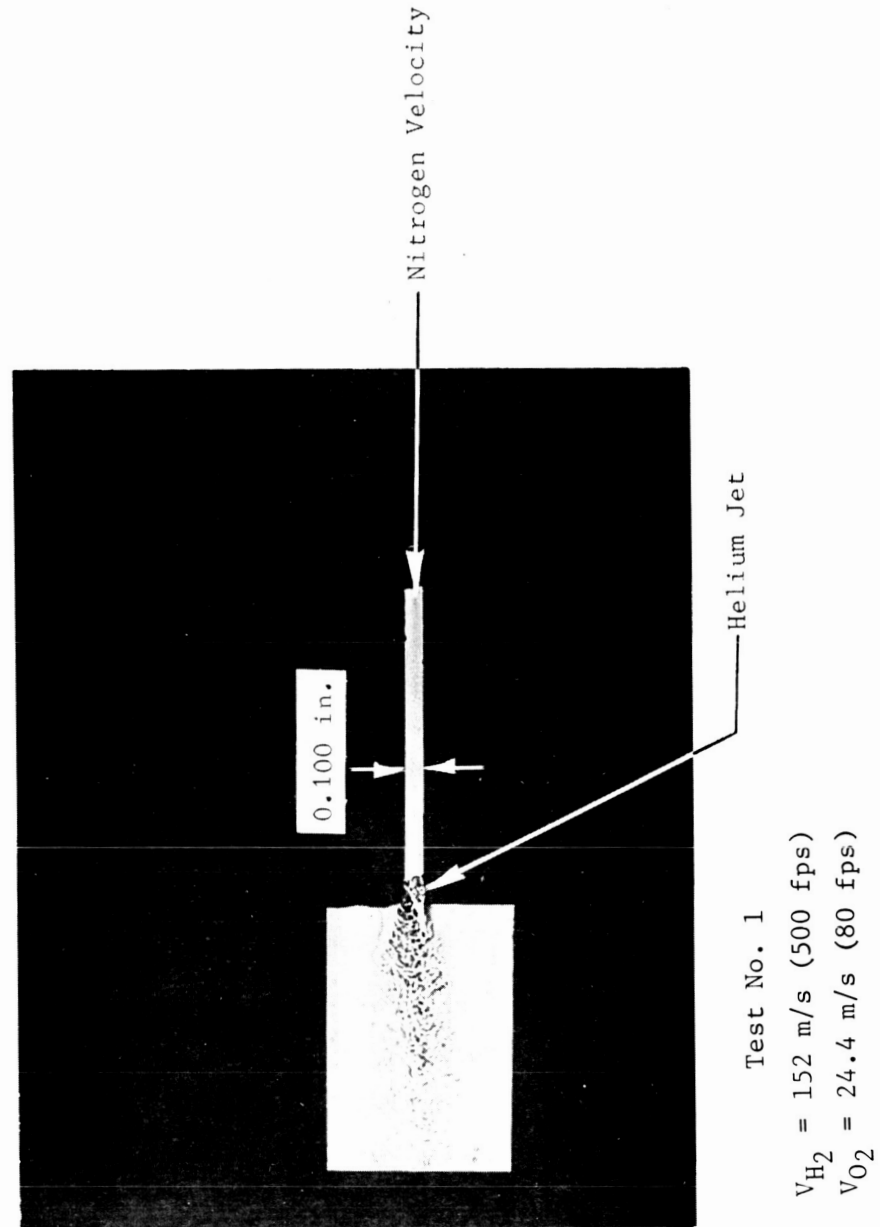
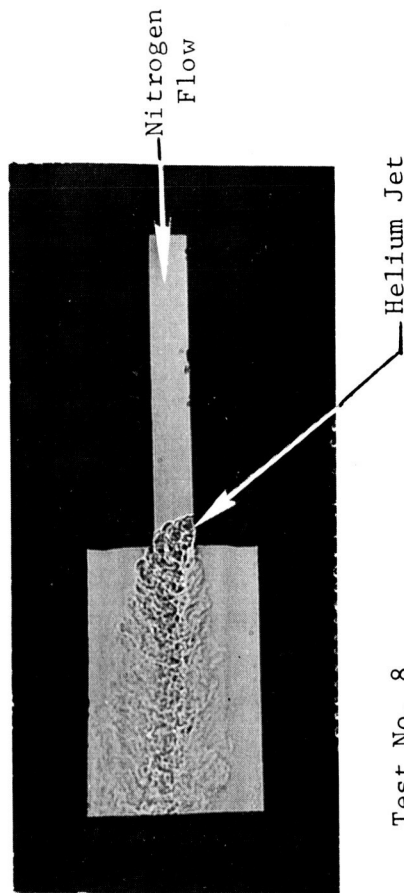


Figure III-16. Penetration Characteristics

$$D_{H_2} = (0.060 \text{ in.}) \cdot 1524 \text{ cm}$$

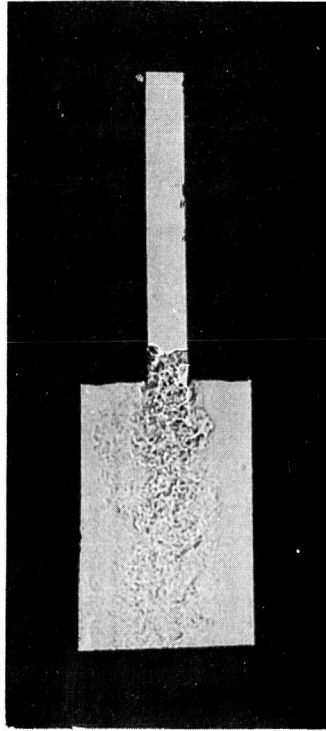


Test No. 8

Recess = (0.1 in.) 0.254 cm

$V_{H_2} = (1000 \text{ fps}) 304.8 \text{ m/sec}$

$V_{O_2} = (96 \text{ fps}) 29.3 \text{ m/sec}$



Test No. 20

Recess = (0.1 in.) 0.254 cm

$V_{H_2} = (2000 \text{ fps}) 610 \text{ m/sec}$

$V_{O_2} = (96 \text{ fps}) 29.3 \text{ m/sec}$

Figure III-17. Velocity Comparisons

### III,A, Injectors (cont.)

noted at recess distances to 1.3 cm (0.5 in.). With recesses greater than 2.54 cm (1.0 in.), the fuel jet tended to attach to the far wall rather than flow homogeneously through the entire slot width. It was concluded from this series that a recess up to 1.3 cm (0.5 in.) would improve mixing.

A larger diameter 0.23 cm (0.090 in.) fuel jet was evaluated over velocities from 152 m/sec (500 fps) to 610 m/sec (2000 fps) and recess to 2.54 cm (1.0 in.). The mixing was improved, but the penetration of the helium jet increased with the larger diameter. For the 0.23 cm (0.090-in.) hydrogen orifice, the maximum fuel velocity for good mixing without penetration to the far wall was 301 m/sec (1000 fps). The mixing was improved as the hydrogen orifice was recessed 1.27 cm (0.5 in.)

When the hydrogen injection orifice was increased to 0.32 cm (0.125 in.) dia, improved mixing was shown compared to the 0.23 cm (0.090-in.)-dia at the same injection velocity. The maximum velocity without penetration of the fuel through the oxidizer was 305 m/sec (1000 fps).

The effect of fuel orifice shape was evaluated by testing a slot 0.274 cm (0.108 in.) wide and 0.14 cm (0.055 in.) deep (injection area comparable to a 0.23 cm (0.090-in.)-dia orifice). Improved mixing and reduced fuel penetration was observed for equivalent fuel velocities.

From these tests it was concluded that round hydrogen orifices flowing at approximately 305 m/sec (1000 fps) would provide good mixing characteristics and that improved mixing was available, if required, by the use of less easily produced slotted fuel injection orifices. The fuel orifice diameter selected was nominally 0.23 cm (0.090 in.), which would provide 60 orifices in each vane.

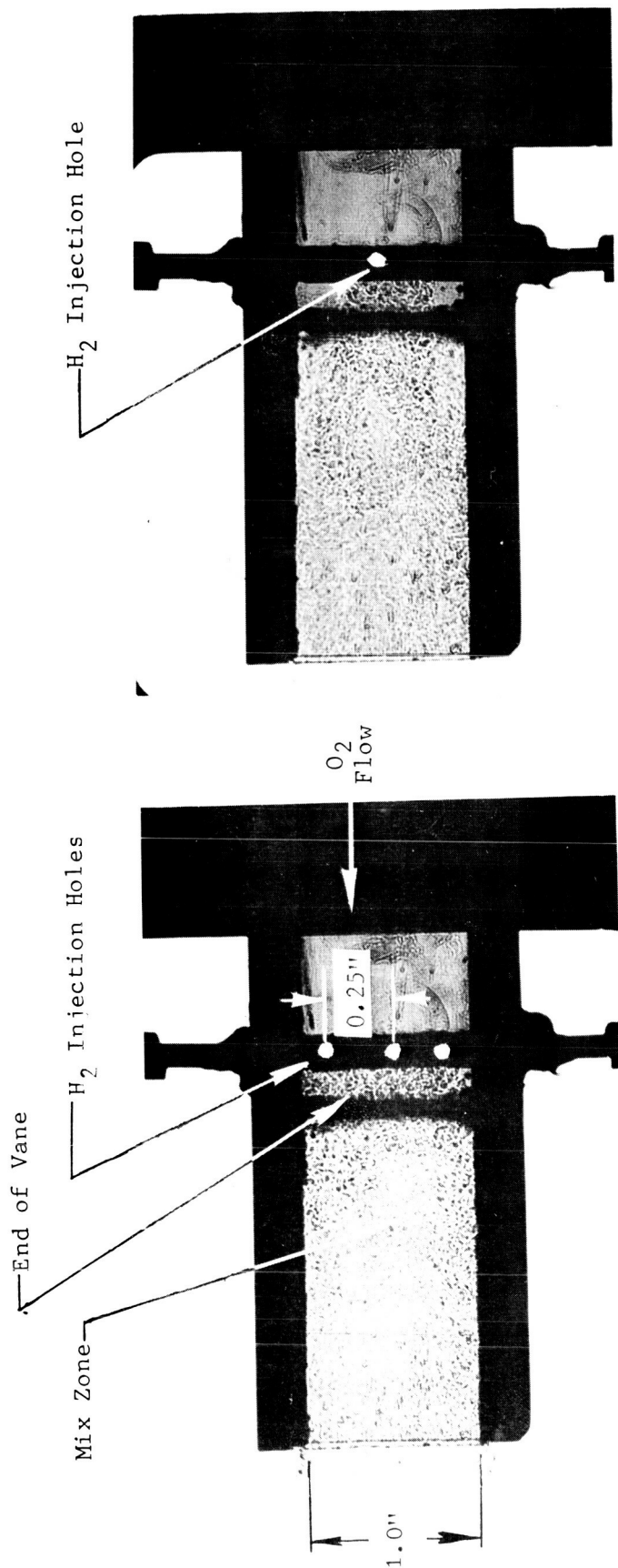
### III,A, Injectors (cont.)

Test Series II was conducted to evaluate the lateral spreading characteristics of the hydrogen jet to evaluate mixing between adjacent jets. A glass shadowgraph model was constructed to examine the spreading characteristics of a fuel jet as shown in Figure III-18. The fuel simulant is injected toward the camera through the sheet of oxidizer that is flowing from right to left at 80 fps across the three fuel jets. The left frame of Figure III-19 shows the spreading characteristics of fuel injected at 152 m/sec (500 fps) into oxidizer flowing at 24.4 m/sec (80 fps). The three fuel orifices were recessed .25 cm (0.1 in.) back from the vane tip. Excellent mixing is indicated by the near homogeneous flow. Tests conducted with a reduced fuel velocity, 76 m/sec (250 fps), and increased oxidizer velocity 34.2 m/sec (112 fps), reduced the spreading width by about 10% from the earlier test. The fuel was injected from the center hole only at a fuel velocity of 229 m/sec (750 fps) for Test 94. The jet spread to a 1.27 (0.5-in.) width at the vane tip 0.254 cm (0.1 in.) from the injection point, indicating that a hole spacing of 1.27 cm (0.5 in.) (center to center) will provide a homogeneous distribution of fuel.

The internal flow characteristics of the vane were evaluated to determine the mass flux distribution over the vane length. The flow from the hydrogen orifices was quantitatively evaluated using a pitot tube collector placed over each hydrogen orifice to determine the orifice-to-orifice flow variation. Figure III-19 shows the measured variation as a percent of nominal along the vane length. There was some flow restriction near the injector center vane end which was corrected by a slight enlargement to increase the flow area.

The last series of tests evaluated the effect of the vane internal "cross velocity" on fuel injection angle. The fuel flows across the vane in a radial direction and must turn at a right angle to flow out the injection orifice. Tufts attached to the outside of the vane were used to show





Test No. 89

Three H<sub>2</sub> Holes Flowing

$V_{H_2} = (500 \text{ fps}) \ 152.4 \text{ m/sec}$

$V_{O_2} = (80 \text{ fps}) \ 24.4 \text{ m/sec}$

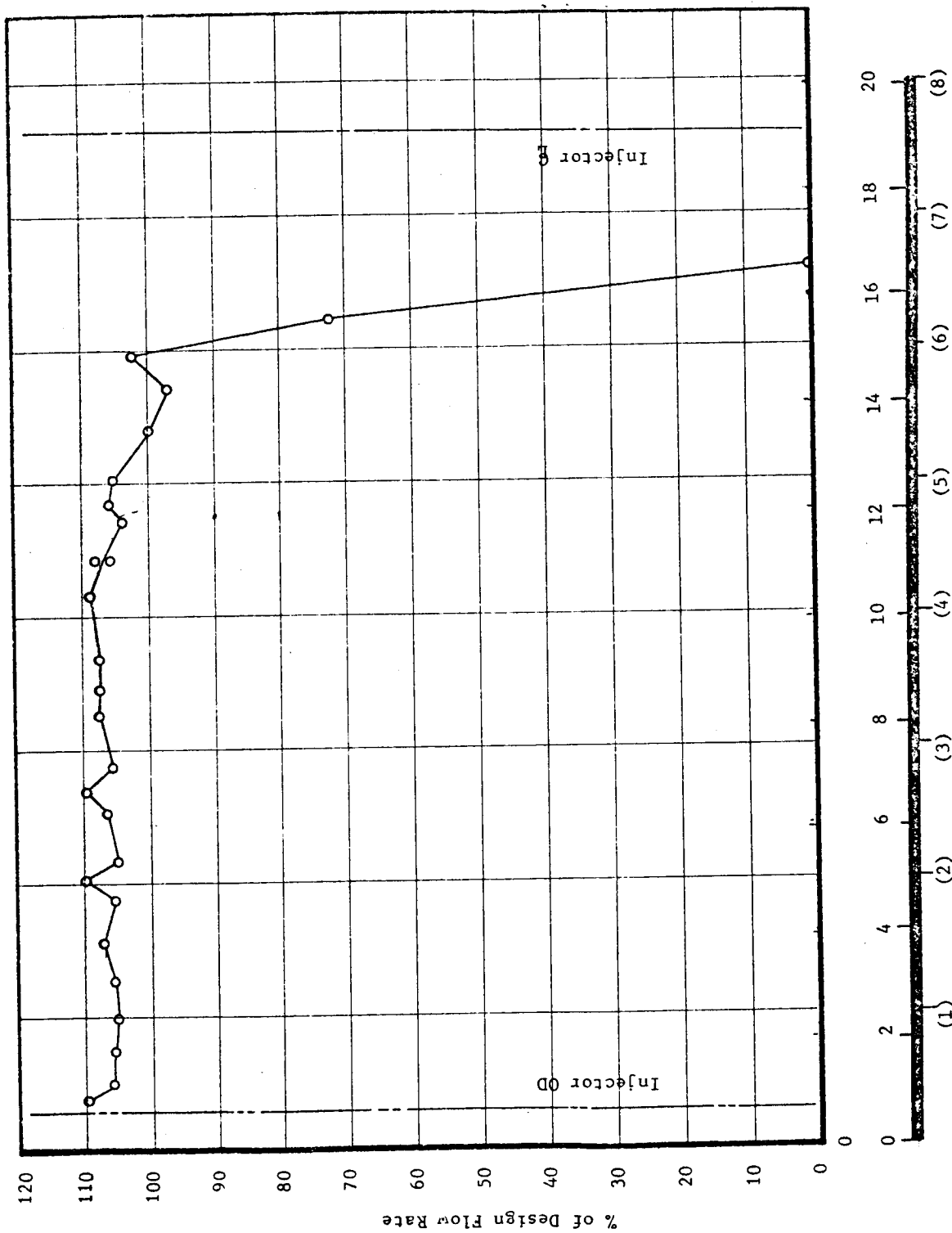
Test No. 94

One Hole Flowing

$V_{H_2} = (750 \text{ fps}) \ 228.6 \text{ m/sec}$

$V_{O_2} = (80 \text{ fps}) \ 24.4 \text{ m/sec}$

Figure III-18. Jet Spreading Characteristics



Vane Radial Distance, cm (in.)

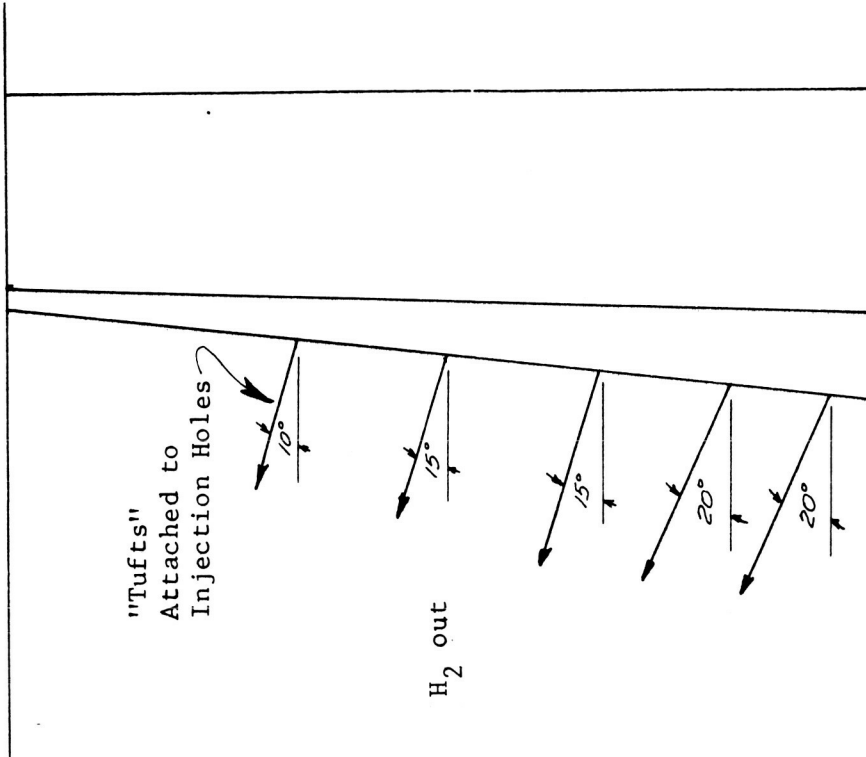
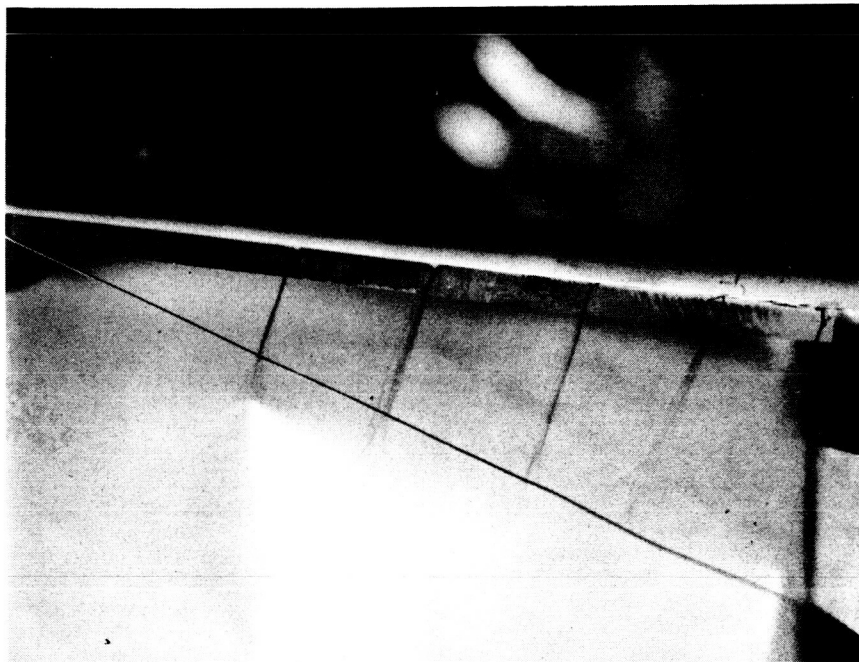
Figure III-19. Vane Flow Distribution

### III,A, Injectors (cont.)

flow direction. The flow viewed normal to the vane looking directly at the fuel injection holes indicated completely perpendicular flow with no axial flow component (axial being toward the chamber throat). The radial flow component resulted in the velocity vectors shown in Figure III-20. Flow tufts were located on selected hydrogen injection holes. Orifices near the injector wall flowed at an angle  $20^\circ$  to a line normal to the vane centerline. The injection angle was reduced to  $10^\circ$  near the injector centerline. The measured angular deviation was acceptable since the resultant displacement was considerably less than the spreading width demonstrated.

In addition to the penetration and spreading tests with single orifices, cold flow testing was also conducted with two complete vanes which constituted a  $1/30$  segment of the vaned injector. A total of 45 tests were run in which flow data was accumulated at two axial stations traversing radially along the centerline between vanes. Figure III-21 shows the flow test setup with the traversing combination pressure and temperature rake.

The first set of tests evaluated the mixture ratio characteristics with the probe located at the trailing edges of the injector vanes, (0.0 in. axial distance). Measurements were made at 3 radial stations along the vane, namely the 16.5 cm (6.5 in.), 11.4 cm (4.5 in.), and 6.3 cm (2.5 in.) radial positions. The resulting profiles are portrayed in the upper portion of Figure III-22. The corresponding centerline mixture ratio is shown in Figure III-23 by the open symbols. Referring first to the radial profile (Figure III-24), a high oxidizer flow is noted over the outer 5.1 cm (2 in.) of the injector where the vane spacing is a maximum. This is believed to be a result of two factors. Most important is the small penetration of the fuel in the flow centerline at the zero axial length. The resulting mixture ratio is therefore high due to inadequate mixing rather than a gross mass flux distribution. Directly below the vanes a fuel rich condition is noted on Figure III-23. Proceeding radially inward the vane spacing diminishes and the mixing is im-



Test No. 100

$V_{H_2} = (1000 \text{ fps}) \ 304.8 \text{ m/sec}$

$V_{O_2} = 0 \text{ fps}$

Figure III-20. Vane Flow Characteristics

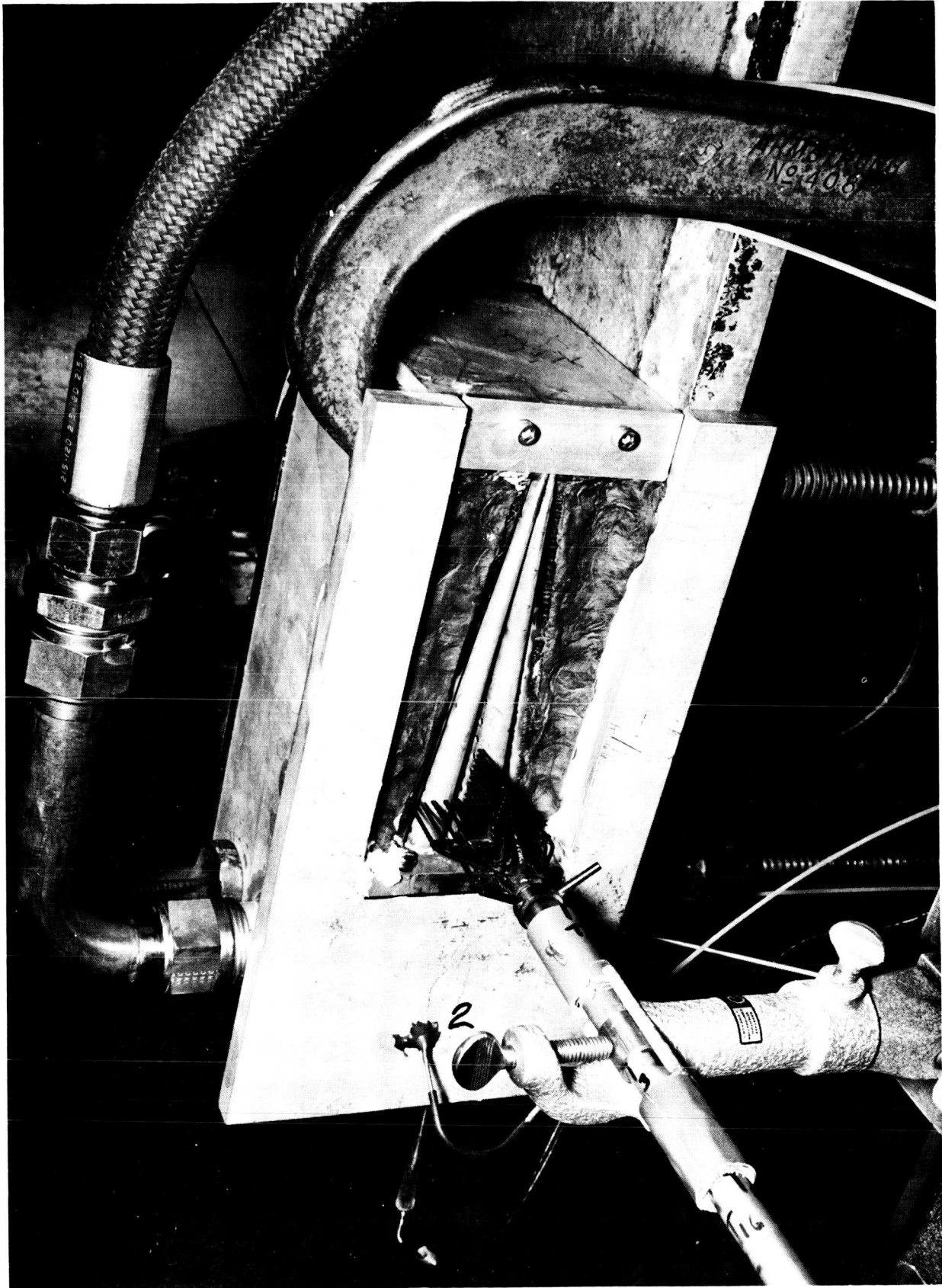


Figure III-21. Segment Mixing and Distribution Model

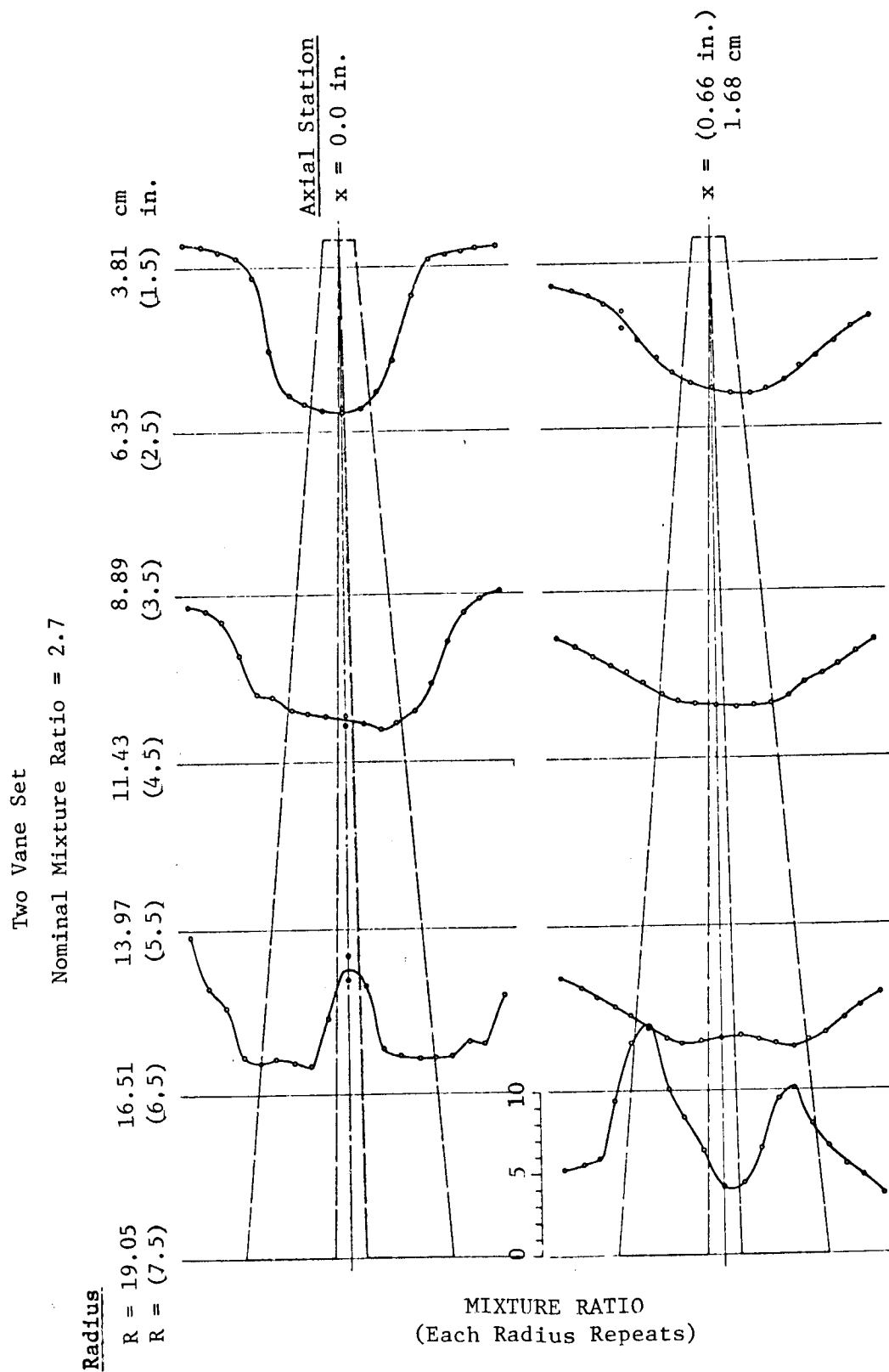


Figure III-22. Radial and Axial Mixture Ratio Profiles - Vane Injector

# VANE INJECTOR

NOMINAL MIXTURE RATIO = 2.7

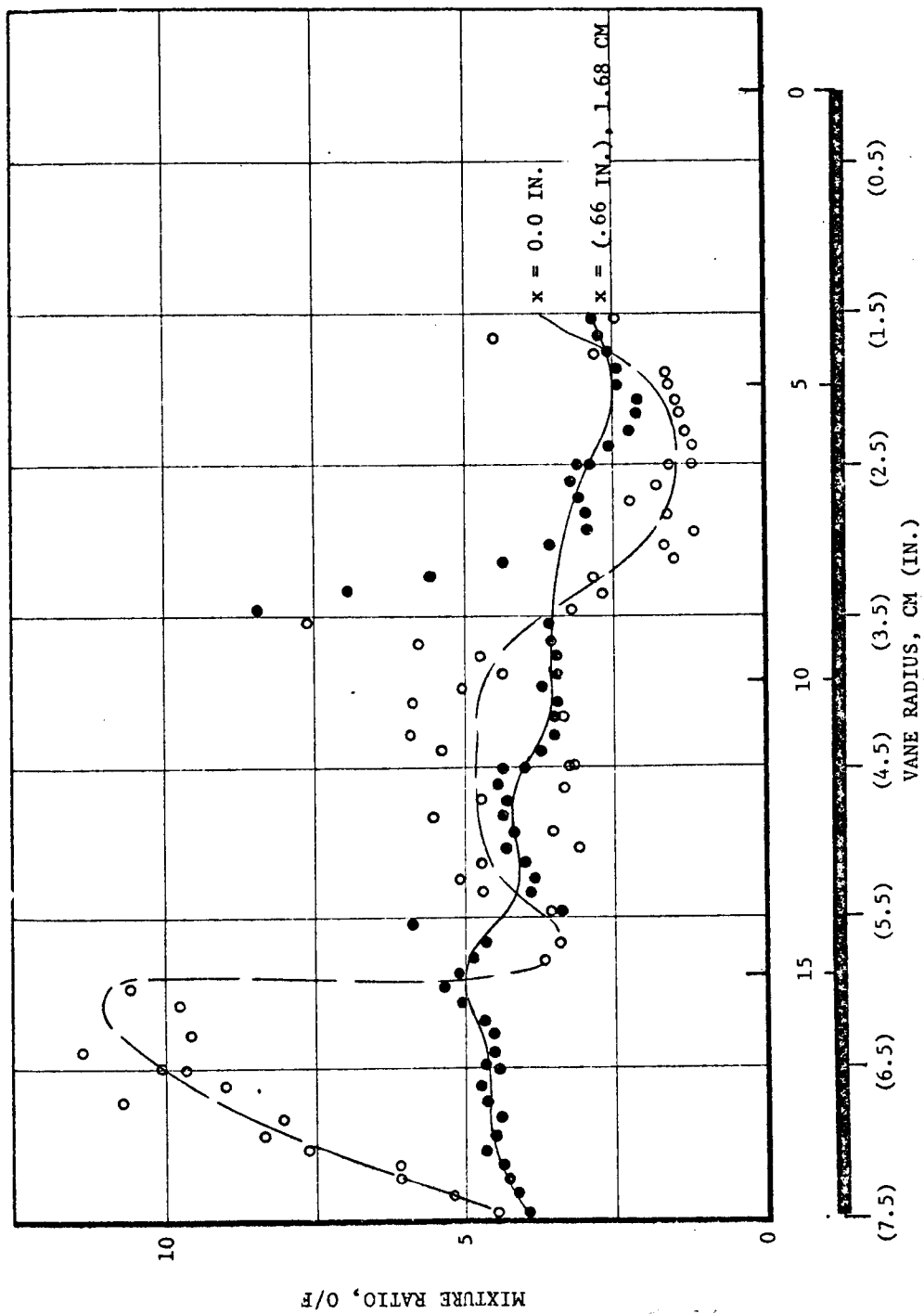


Figure III-23. Radial Mixture Ratio Profile

### III,A, Injectors (cont.)

proved, defining a lower mixture ratio. At these stations a very even mixture ratio profile is noted over the full width of the vane set. Where the vane tips converge, at approximately 6.3 cm (2.5 in.), a lower than desired ox flow is noted due primarily to vane blockage.

Referring next to the 1.7 cm (.66 in.) axial station data, a more complete mixing profile results as indicated by the darkened dots of Figure III-23 but again, with a definite trend toward an oxidizer rich condition at the outer radii. The increased mixing can be directly noted by comparing the upper and lower diagrams of Figure III-22. At a distance of 1.7 cm (.66 in.) the oxidizer rich core between vanes is removed giving a uniform profile across the vane. With this complete mixing characteristic, the radial mixture ratio profile can be inferred. This trend is shown by the closed dots of Figure III-23. A higher to lower mixture ratio trend is evidenced along the two-vane set centerline, with a definite oxidizer rich zone noted at the 8.9 cm (3.5 in.) radius. Since a level fuel distribution was noted in the single vane testing, the resulting trends are attributed to an oxidizer maldistribution. The high mixture ratio zone at 8.9 cm (3.5 in.) occurs where the 2 rows of fuel holes merge to one row. This discontinuity appears to produce an adverse mixture ratio which is most likely coupled with a decreased mixing characteristic. In order to more completely evaluate the seriousness of this discontinuity a hot test evaluation was conducted prior to modification in order to accurately assess the cold flow data.

In summary, these cold flow tests indicate three important characteristics. First, an oxidizer rich zone is noted between vanes near the injector face at the outermost portion of the injector. This apparent maldistribution is due to limited jet penetration and is eliminated at a 1.7 cm (.6 in.) axial distance. Second, a slight mixture ratio variation exists in the radial direction which appears due to oxidizer manifold interactions. Third, a localized high mixture ratio zone is noted at a radius of 8.9 cm (3.5 in.), the severity of which was to be evaluated in segment hot tests.



### III,A, Injectors (cont.)

#### b. Segment Hot Fire Tests

The two vane segment cold flow hardware was test fired to atmospheric pressure to evaluate the vane heating characteristics. The vane segment, shown in Figure III-21, was modified to improve the interpropellant seals and to provide a heat resistant face plate.

The vanes were instrumented with thermocouples interlocked to terminate the test if the temperature reached 1200°F. When hot fired, the tests were terminated by thermocouples located at the transition from the single row of hydrogen orifices to the double row of orifices near the radial center-line of the injector, indicating local overheating in this area. The hydrogen flow in this area appeared to offer less blockage to the oxygen flow resulting in an area of higher than design mixture ratio. A modified vane set was prepared but not fired at the time this activity was curtailed.

#### c. Vaned Injector Fabrication

Vanes were die formed from standard stainless steel tubing prior to orifice machining. Final assembly was to be accomplished by installing the vanes into the mating holes in the outer housing and to alignment slots in the central hub followed by the installation of vane spacers and braze alloy. The assembly was to have been brazed prior to final machining of the seal surfaces.

### 4. Film Coolant Injector

#### a. Description

The film coolant injector design consists of a manifold assembly and removable film coolant sleeves.

The coolant flow into the chamber was through an annular gap between the chamber wall and the outside surface of the sleeve. Three sleeve lengths and three annular gap configurations were designed to allow variation of coolant injection station and coolant injection velocity.

### III,A, Injectors (cont.)

#### b. Fabrication

One coolant manifold and nine coolant sleeves were fabricated. The manifold was fabricated of 347 stainless steel in two parts. An inner ring assembly provided the radial inward flow distribution between the bolts from the manifold to the removable coolant sleeve. A lathe turned ring was milled to provide the radial coolant flow passages and then covered by a brazed plate. A manifold assembly, which incorporated the circumferential distribution plenum and distribution orifices, was welded to the inner ring after flow testing had verified the distribution characteristics.

The film coolant sleeves were fabricated of mild steel. Three coolant sleeve lengths were produced, each with three annular gap dimensions. Sleeve lengths of 1.27 cm (0.5 in.), 7.1 cm (2.78 in.), and 15.2 cm (6.0 in.) were selected to evaluate injector face plane injection, convergent area injection with a 41 cm (16 in.)  $L^*$  chamber, and convergent area injection with a 66 cm (26 in.)  $L^*$  chamber. Coolant annuli were fabricated to provide a coolant velocity equal to the combustion product's velocity at coolant flows of 10, 20 and 30% of the total hydrogen.

### III, Technical Discussion (cont.)

#### B. HEAT SINK CHAMBERS

##### 1. Geometry Evaluation and Selection

###### a. Chamber

###### (1) Contraction Ratio

The selected contraction ratio was 2.65, which is based primarily on injector design and engine pressure schedule considerations. Manifolds for the low density gaseous propellants require large cross-sectional areas and clean aerodynamic flow passages to ensure uniform propellant injection. A large injector diameter would reduce manifold distribution problems by reducing manifold velocities, but also can result in element jet impingement on the chamber walls where the steep chamber wall angle converges to the throat. Weight and size considerations implied that the contraction ratio should be kept to the lowest possible value.

The lower limit for injector contraction ratio was dictated by engine pressure schedule requirements. The allowable system pressure drop of  $3.5 \text{ N/cm}^2$  (5 psi) for valves, lines, and injector required judicious utilization of pressure drop. Momentum pressure losses associated with heat addition (energy release) are minimized by combusting at a low chamber Mach number. This effect, generally termed Rayleigh line momentum pressure loss, results from acceleration of the gases because of density differences encountered by the flow in changing from the initial temperature state to final adiabatic flame temperature. Ten percent of the system pressure drop ( $.35 \text{ N/cm}^2$ ) (0.5 psi) was budgeted for this loss, which required that reaction be complete prior to 2.2 contraction ratio. Combustion downstream of this location, at a lower contraction ratio, will result in larger total pressure losses, reducing deliverable engine thrust.

### III,B, Heat Sink Chambers (cont.)

#### (2) Chamber Contour and Length

The chamber contour was selected to allow tests to be conducted over a range of  $L^*$  from 25 to 102 cm (10 to 40 in.) using a single nozzle design with cylindrical  $L^*$  sections to increase the chamber length. The nozzle convergence, to accommodate the short 25 cm (10-in.)  $L^*$  configuration, was somewhat more rapid than optimum but was considered acceptable since it was expected to provide a somewhat conservative evaluation of film coolant effectiveness. The chamber design with  $L^*$  sections attached is shown in Figure III-24. The length and volumetric configurations available with these parts were:

<u>Injector Face to Throat Length</u>		<u><math>L^*</math> of Combination</u>	
<u>cm</u>	<u>in.</u>	<u>cm</u>	<u>in.</u>
15	6	26	10.4
20	8	40	15.8
30	12	68	26.6
41	16	95	37.4

#### b. Nozzle

Optimization of a nozzle contour entails evaluation of the candidate nozzle lengths, weight, performance, and performance/weight tradeoff factors for the particular vehicle mission. A weight/performance tradeoff factor or a nozzle length limitation was not available for this evaluation. The nozzle contour analysis was, therefore, based on performance within reasonable length limitations.

Four nozzle types were evaluated: short Rao, long Rao, 20° cone, and a 15° cone. The boundary layer and divergence losses were

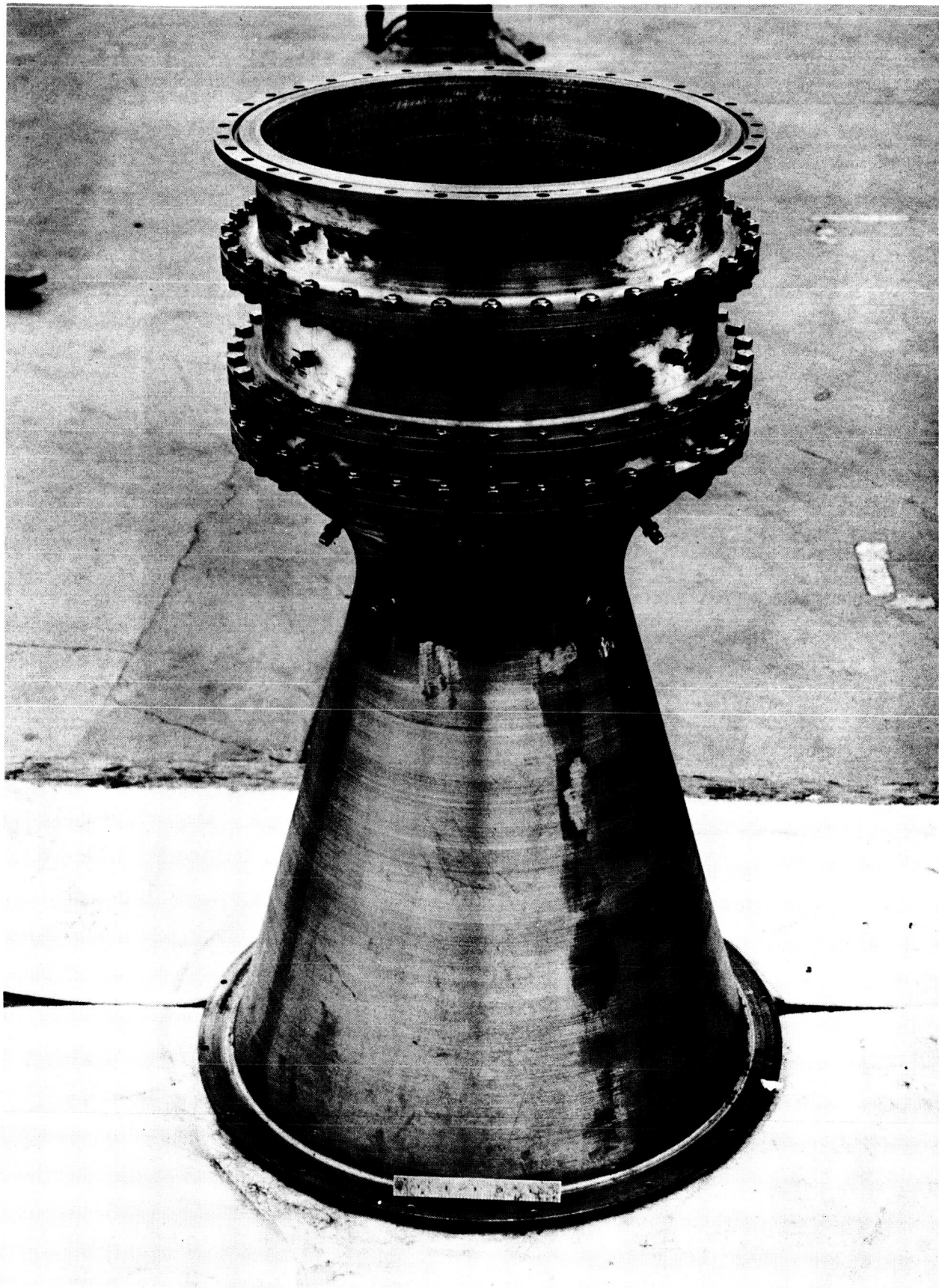


Figure III-24. Workhorse Chamber Assembly

### III,B, Heat Sink Chamber (cont.)

evaluated for the four candidate approaches using ICRPG-recommended techniques. The results of this analysis appear in Table VI. The 15° conical nozzle was found to be 2.8 sec higher performing than a long Rao contour. This performance advantage is somewhat offset by the additional weight of the 10.5 cm (4.1-in.) longer nozzle length. The 15° conical nozzle was selected on the basis of performance potential and fabrication advantages.

TABLE VI

#### NOZZLE OPTIMIZATION SUMMARY

<u>Nozzle Type</u>	<u>Length, in.</u>		<u>Performance Losses in Vacuum Specific Impulse</u>		
	<u>cm</u>	<u>in.</u>	<u>Boundary Layer</u>	<u>Divergence</u>	<u>Total Losses</u>
Short Rao	38	14.8	7.7	17.2	24.9
Long Rao	44	17.3	7.9	9.9	17.8
15-Degree Cone	54	21.4	9.5	5.5	15.0
20-Degree Cone	40	15.8	11.1	10.5	21.6

#### 2. Chamber Design

##### a. Design Description

The heat sink chamber design shown in Figure III-24 consists of a chamber-nozzle to provide a 25 cm (10-in.) L\* chamber and a 15° half angle expansion nozzle with an exit area ratio of 5. Additional chamber length is provided by L\* sections. These L\* sections were final machined as an assembly to minimize gas-side discontinuities which could disrupt coolant flow.

### III,B, Heat Sink Chamber (cont.)

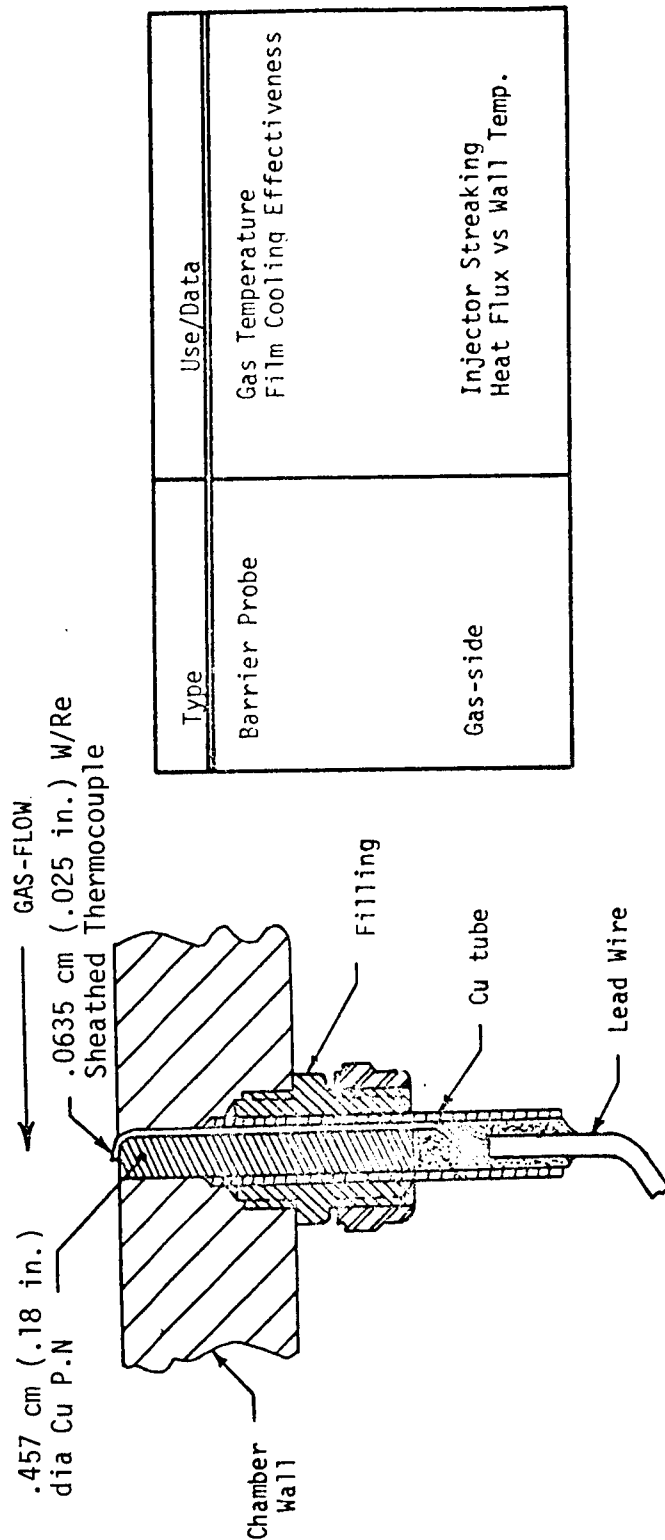
The heat sink chamber components were designed to be of low carbon steel for economy. A 0.63 cm (0.25-in.) wall was adequate to provide heat sink capacity for this low heat flux application. The design incorporated alignment grooves at chamber-nozzle to  $L^*$  section interfaces to ensure that discontinuities were not developed due to chamber heating and cooling. Copper gaskets were used to seal the chamber sections to each other and to the injector. Two chamber pressure ports, fittings for barrier temperature probes, and provisions for installation of gas-side chamber wall thermocouples were included in the design.

The streak chamber design for compatibility testing was provided by applying an ablative material to the inside surface of a heat sink chamber. A silicone rubber ablative was applied to the cleaned and primed nozzle assembly and to selected  $L^*$  sections.

#### b. Thermal Instrumentation

Two types of thermal instrumentation were installed on the heat sink chambers. Thermocouples were brazed into the chamber wall with the thermocouple hot junction located flush with the gas-side surface, and high temperature thermal barrier probes were installed with a thermocouple junction extending into the boundary layer. Chamber wall and film temperature measurements were made to determine film coolant effectiveness, gas-side heat flux, and heat transfer coefficient.

The gas-side thermocouples used were 0.051 cm (0.020-in.) chromel/alumel sheathed probes brazed in place flush with the gas-side wall. A sketch of the installation is shown in Figure III-25. The boundary layer probe is also shown in Figure III-26. The probe consists of a removable copper pin from which a (0.062 cm) 0.025-in. tungsten/rhenium thermocouple protrudes into the gas stream. The device is capable of measuring gas temperatures to 2480°K (4000°F).



Type	Use/Data
Barrier Probe	Gas Temperature Film Cooling Effectiveness
Gas-side	Injector Streaking Heat Flux vs Wall Temp.

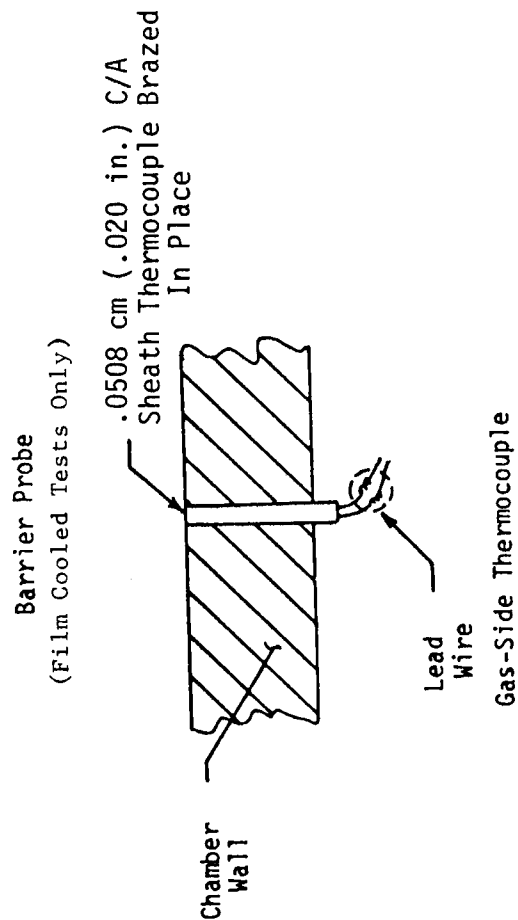


Figure III-25. Thermocouple Installation



### III,B, Heat Sink Chamber (cont.)

Gas-side thermocouples were installed at four angular positions,  $90^\circ$  apart, in each  $L^*$  section and in the convergent section, throat, and at three stations in the exit nozzle. Barrier probes were located at three angular positions in each  $L^*$  section and in the convergent section and throat of the chamber-nozzle assembly.

#### 3. Chamber Fabrication

Two workhorse chamber and  $L^*$  assemblies were fabricated and instrumented. An ablative coating, for streak chamber testing, was applied to one assembly.

The chamber and nozzle assembly components were fabricated of 1010 carbon steel. A rolled and welded conical section was used for the exit nozzle. The nozzle was welded to the convergent section, which was rough machined from a forging, and the assembly was machined to final dimensions using a tracer lathe.  $L^*$  sections were machined from forgings.

After installation of pressure transducer bosses and Swage-Lok fittings for the thermal probes, the inside cylindrical surfaces of the chamber  $L^*$  section and nozzle were final machined as an assembly to minimize the mismatch at these interfaces. Offset pins were installed in the assembly to ensure reassembly in the proper sequence. Gas-side thermal instrumentation was then torch brazed into place.

The streak chamber ablative coating was applied to the second heat sink chamber assembly by test technicians. The inside surfaces of the chamber and nozzle assembly were cleaned and primer was applied to the inside and allowed to dry. The silicone rubber ablative material was then applied by brush to a thickness of approximately 0.127 cm (0.05 in.) over the primed surfaces.

### III, Technical Discussion (cont.)

#### C. COOLED CHAMBERS

##### 1. Cooled Chamber Concept Evaluation

A variety of cooling concepts were analyzed prior to recommendation of two concepts for detailed design. Potential for low weight, high performance, low hydrogen inlet pressure requirements, and flexibility to allow nozzle scarfing to 45 degrees were primary considerations for this comparative evaluation. In deference to the objective of this technology program, distinctly different cooling modes were evaluated to ensure that the cooled chamber concepts were not dependent upon a single cooling technique.

The cooled chamber concepts evaluated for this application are shown on Figure III-26. Three general methods of cooling were considered. These were: a totally film-cooled shell, a fully regeneratively cooled design, and concepts in which a portion of the hydrogen passes through coolant passages in the chamber prior to introduction into the chamber or nozzle extension to serve as a film coolant.

Analysis indicated that all designs would require some hydrogen film coolant at the injector end of the chamber. Coolant quantity and the injection technique for maximum effectiveness were to be determined during the Task XVIII injector test series where coolant injection velocities, quantities, and injection locations were to be evaluated.

The estimated effect of the various cooling concepts on specific impulse is also shown on Figure III-26. The performance differences were considered to be small and were not considered to be a significant factor in the selection process.

### III,C, Cooled Chambers (cont.)

Predicted chamber heat fluxes for the low pressure engine were low, which allowed the use of relatively low conductivity materials to be used for the flame liner without incurring excessive temperature gradients across the liner thickness. Therefore, all concepts were evaluated using a nickel base superalloy as the liner material. This material has high yield strength at elevated temperature, which allows the film-cooled chamber to be operated at low film coolant flow rates (for high performance) and with a thin wall (for low chamber weight).

Conventional double-shell chamber wall construction used for convectively cooled chambers results in high thermal strains on the inner liner due to the constraints against thermal expansion imposed by the cool outer shell. A flame liner of a high yield strength material will minimize plastic deformation of the liner, thereby increasing the number of firing cycles the chamber can withstand.

The relative performance, weight, and inlet requirements for the five concepts evaluated along with general comments regarding specific features are summarized in Figure III-26. A brief discussion of each concept follows.

The film-cooled shell was found to be the lightest and least expensive design. The nozzle is readily scarfed to mate with various vehicle interfaces. This design offers good cyclic life capability even at high wall temperatures because the absence of constraints by an external shell results in low thermal stresses. This concept depends on effective film coolant for satisfactory operation.

The regeneratively cooled design was the heaviest concept and it required more inlet pressure than the pressure schedule provided. As with all double-wall concepts, some barrier coolant was required to limit the flame liner temperatures to acceptable levels for high cycle life operation.

### III,C, Cooled Chambers (cont.)

The other three concepts considered were double-wall dump-cooled designs in which part of the hydrogen was used to cool the chamber prior to injection as chamber or nozzle film coolant. As with the full regenerative design, some film coolant was required at the injector end of these chambers to limit wall temperature and thermal strain.

The internal dump configuration cooled the nozzle extension from an area ratio of 1.6 with about 5% of the total hydrogen. Additional hydrogen was required at the injector face plane to limit chamber area thermal stresses. This concept required the most coolant and also would require effective supersonic injection of the nozzle coolant. Next to the film-cooled shell, this was the lightest weight concept.

The full-length reverse dump concept evaluated was similar to the full regenerative design. The channel coolant was injected into the combustion zone as film coolant to alleviate the high inlet pressure required by the full regenerative design. Weight and the complex design which resulted when the nozzle skirt was scarfed detracted from this concept.

A variation of the full reverse dump-cooled concept was also evaluated. In this design (also shown in Figure III-26), the coolant entered a manifold located 12.7 cm (5 in.) below the throat (at  $\epsilon = 1.6$ ) and, from that point, the coolant flowed through channels to the injector face plane where the hydrogen was then injected as film coolant. Compared with the full reverse dump-cooled concept, the chamber weight was lower and the nozzle skirt could be scarfed without excessively complicating manifold pressure balance. A further advantage of this concept was the flexibility provided to allow different nozzle cooling modes to be evaluated should film coolant introduced in the chamber be ineffective for nozzle cooling. A film-cooled nozzle extension (with or without augmenting hydrogen coolant at  $\epsilon = 1.6$ ) or a double-wall direct dump-cooled nozzle was compatible with this design.

### III,C, Cooled Chambers (cont.)

The film-cooled shell and the reverse dump-cooled chamber with a film-cooled nozzle were recommended and approved for detail design by the NASA project manager with the stipulation that a decision on the cooling mode used on the nozzle for the reverse dump-cooled chamber would await the results of the Task XVIII injector tests.

#### 2. Film-Cooled Designs

##### a. Design Description

The film-cooled chamber design shown in Figure III-27 consists of a simple monolithic stainless steel shell welded onto a flange which mates to the film coolant ring and then to the injector. The film coolant manifold assembly, used for the Task XVIII tests, with an appropriate film coolant sleeve design was scheduled for film-cooled chamber tests. The design was completed prior to the completion of the Task XVIII injector tests and reflects a shorter injector face to throat dimension than would be recommended. From the results of the shortened test program, a 30.5 cm (12-in.) L' would be expected to be more near optimum for both performance and cooling.

As will be seen in the discussion of the structural analyses for the cooled chamber designs, material selections have been made to facilitate fabrication of the essentially one-of-a-kind items. For the experimental portion of this program, the chamber was to be fabricated to the final design configuration but austenitic stainless steel was substituted for the superalloy material to simplify fabrication. The similar thermal properties would not compromise the validity of the thermal data to be gathered. Chambers required to withstand a large number of firing cycles would be fabricated of one of the superalloys, such as Hastelloy X.

	Hydrogen Coolant	Performance Decrease to Film Cooled Shell	Weight Relative to Film Cooled Shell	Inlet Pressure, (psia)	Nozzle Scarfing	Cost
Film Cooled Shell	8% at injector	3.6 sec	1.0	(20) 13.8	No Limita- tions	Low
Internal Dump	8% at injector 5% at = 1.6	6.6 sec	1.2	(20) 13.8	No Limita- tions	Moderate
Reverse Dump	8% in channels and injector	3.6 sec	2.0	(20) 13.8	Difficult	High
Full Regenerative	6% at injector	2.4 sec	3.6	(24) 16.55	Difficult	High
Reverse Dump with Film Cooled Skirt	8% in channels and injector	3.6 sec	1.4	(20) 13.8	No Limita- tions	Moderate

Figure III-26. Cooled Chamber Concepts

- 

QTY	CODE	PART OR	DESCRIPTION	UNIT	QTY
1		- 3	CHAMBER		
1		- 2	FLANGE		
			CRCS		
			QJ-5-765-3041		
			COND A, FINISH 37		

Figure III-27. Film-Cooled Chamber

### III,C, Cooled Chambers (cont.)

#### b. Thermal Analyses

A thermal design analysis of the film-cooled chamber has been used to evaluate concepts and to provide a basis for design and structural analyses and material selection. The most recent ALRC film cooling model of Reference 1 was used for the thermal analysis. This model is based on an entrainment mechanism framework. A new correlation for laboratory data of plane, unaccelerated flow was utilized, and the model's applicability is extended into the supersonic region through the use of a recovery factor for the coolant.

The predicted film temperature profiles for various amounts of fuel film cooling are shown in Figure III-28. This analysis assumed the coolant-to-core velocity ratio to be unity at the injection point and that heat is lost from the gas-side only, by radiation from the nozzle exit. For extended duration operation with a low capacitance chamber wall, the film temperatures are representative of chamber wall temperatures. Based on this analysis, 8 to 10% of the hydrogen was expected to be needed to adequately cool this chamber. The predicted gas-side wall start transient temperature responses during startup for the throat and exit regions of the film-cooled liner are shown in Figure III-29 for chamber walls of various thicknesses.

#### c. Structural Analysis

Design and structural analyses were conducted to identify materials, configuration and thermal operating limits commensurate with 100,000 thermal cycle operation. Nickel base superalloys such as Hastelloy X were found to be near optimum for this application. More easily fabricated but thermally

---

Ref 1. Hydrogen/Film Conductive Cooling, Quarterly Technical Progress Narrative for the Period 29 June through 27 September 1970, Report 14343-Q-1, 12 October 1970.



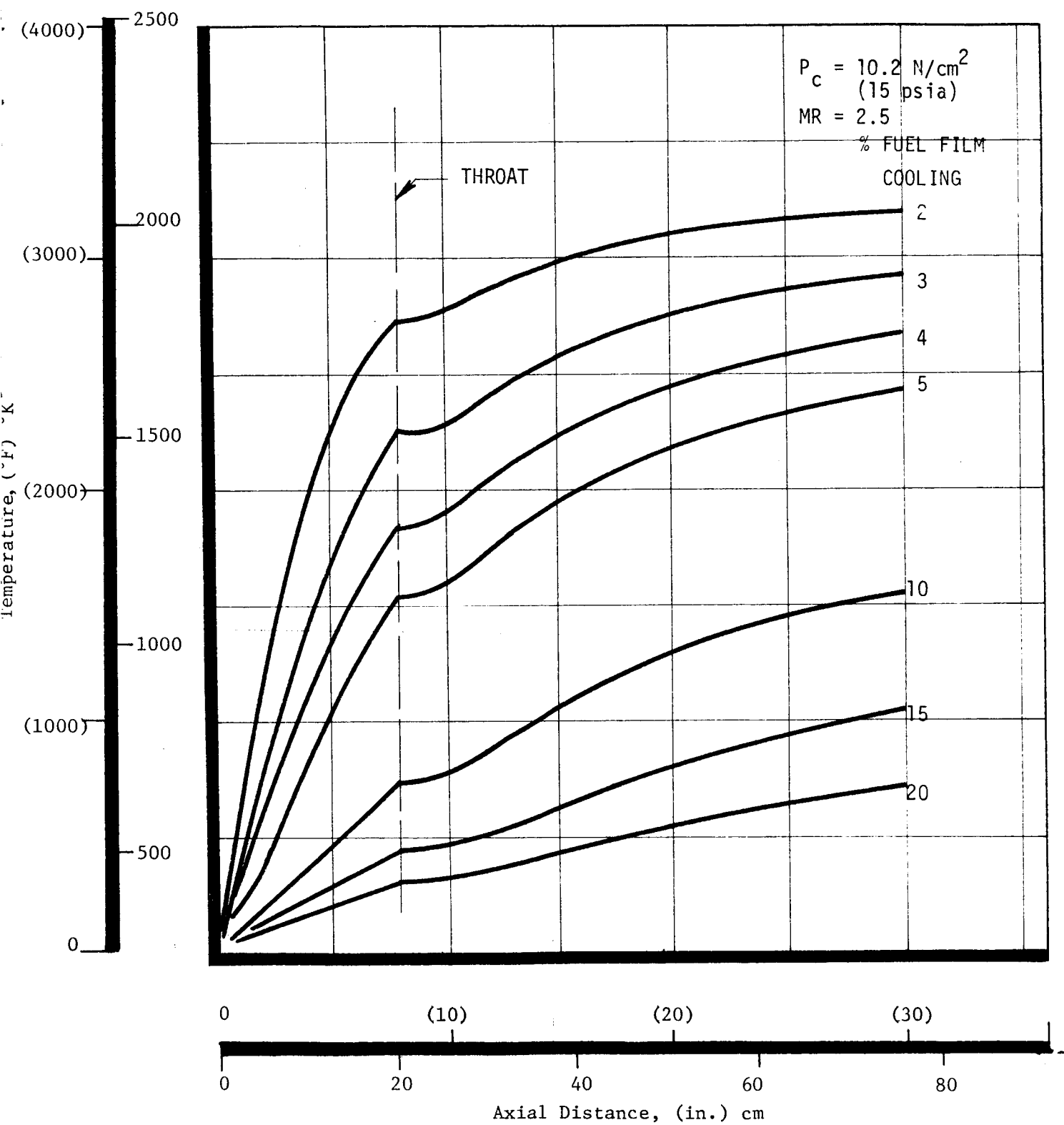


Figure III-28. Predicted Film Temperature Profiles

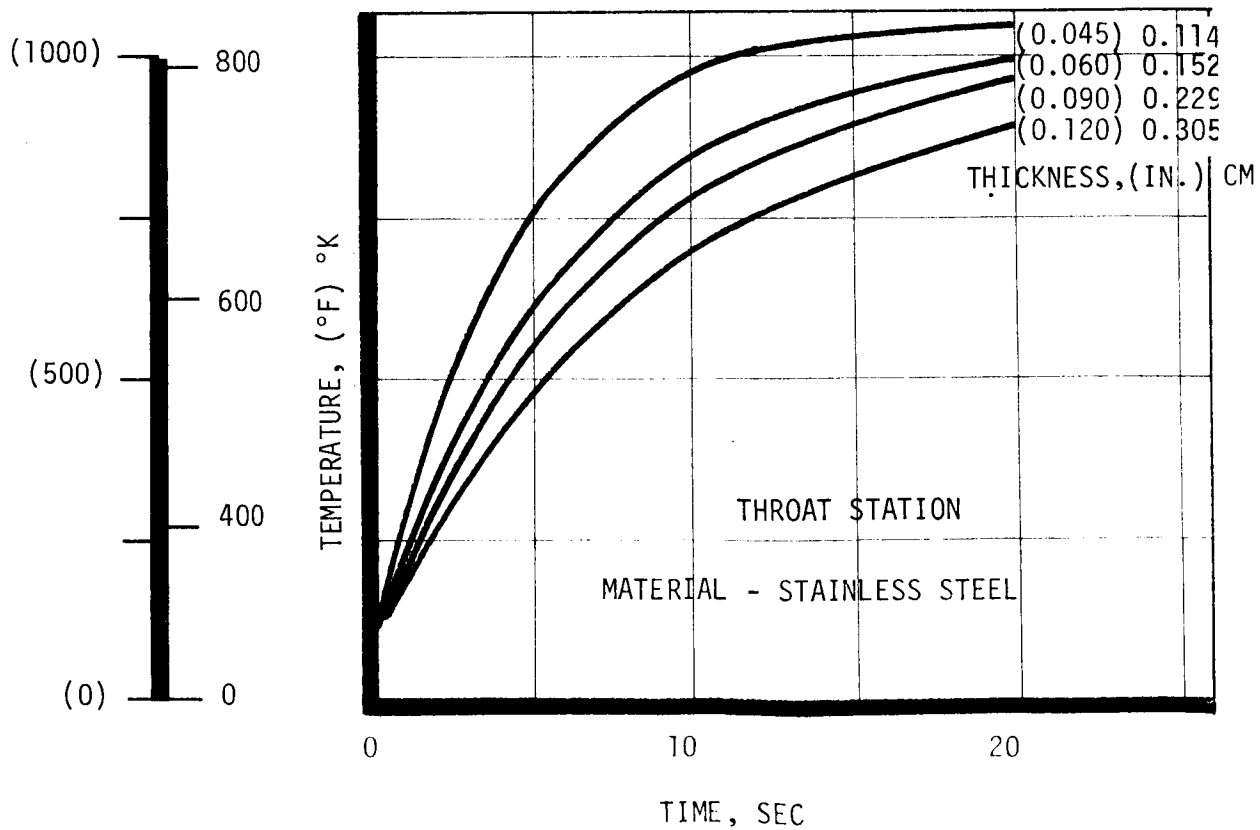
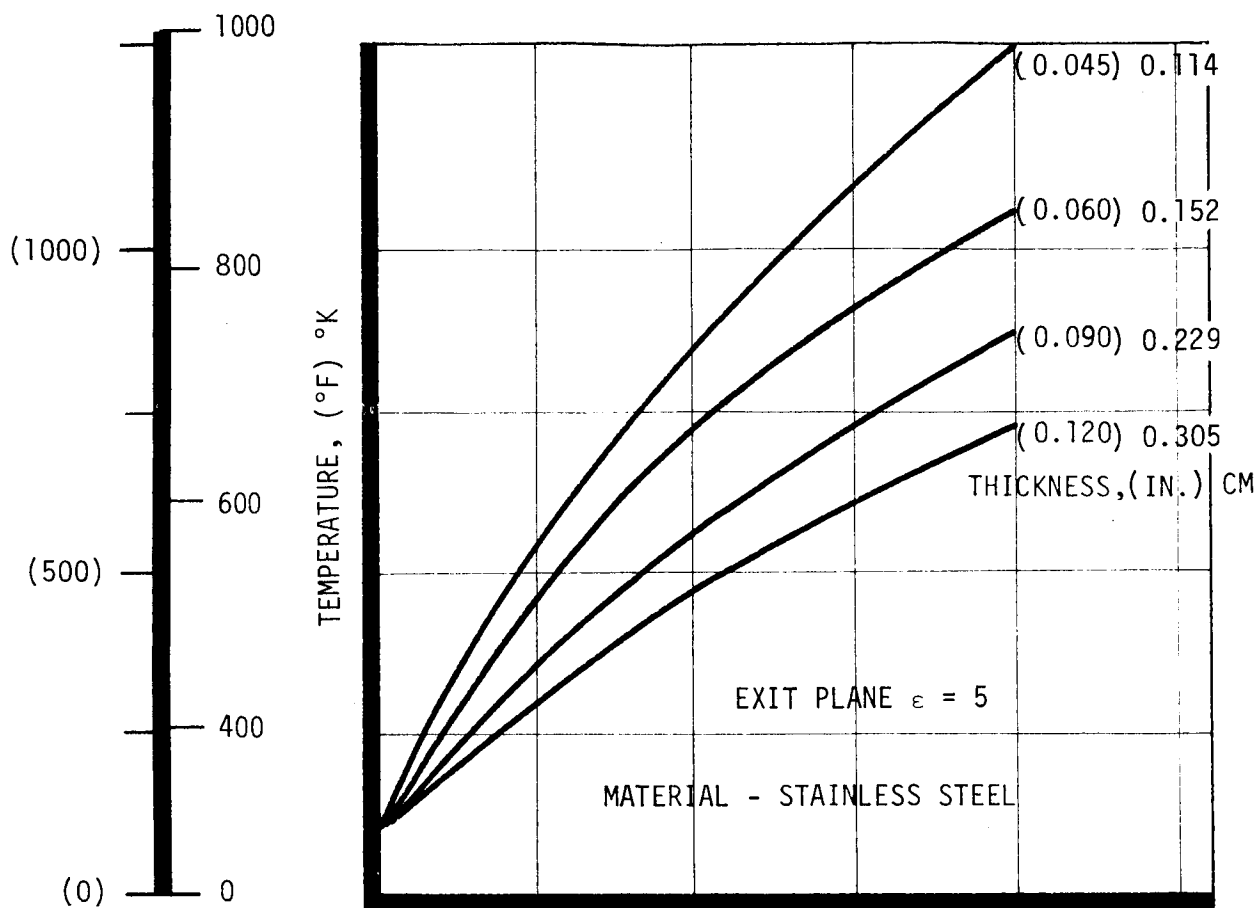


Figure III-29. Predicted Film-Cooled Chamber Gas-Side Transient Temperatures

### III,C, Cooled Chambers (cont.)

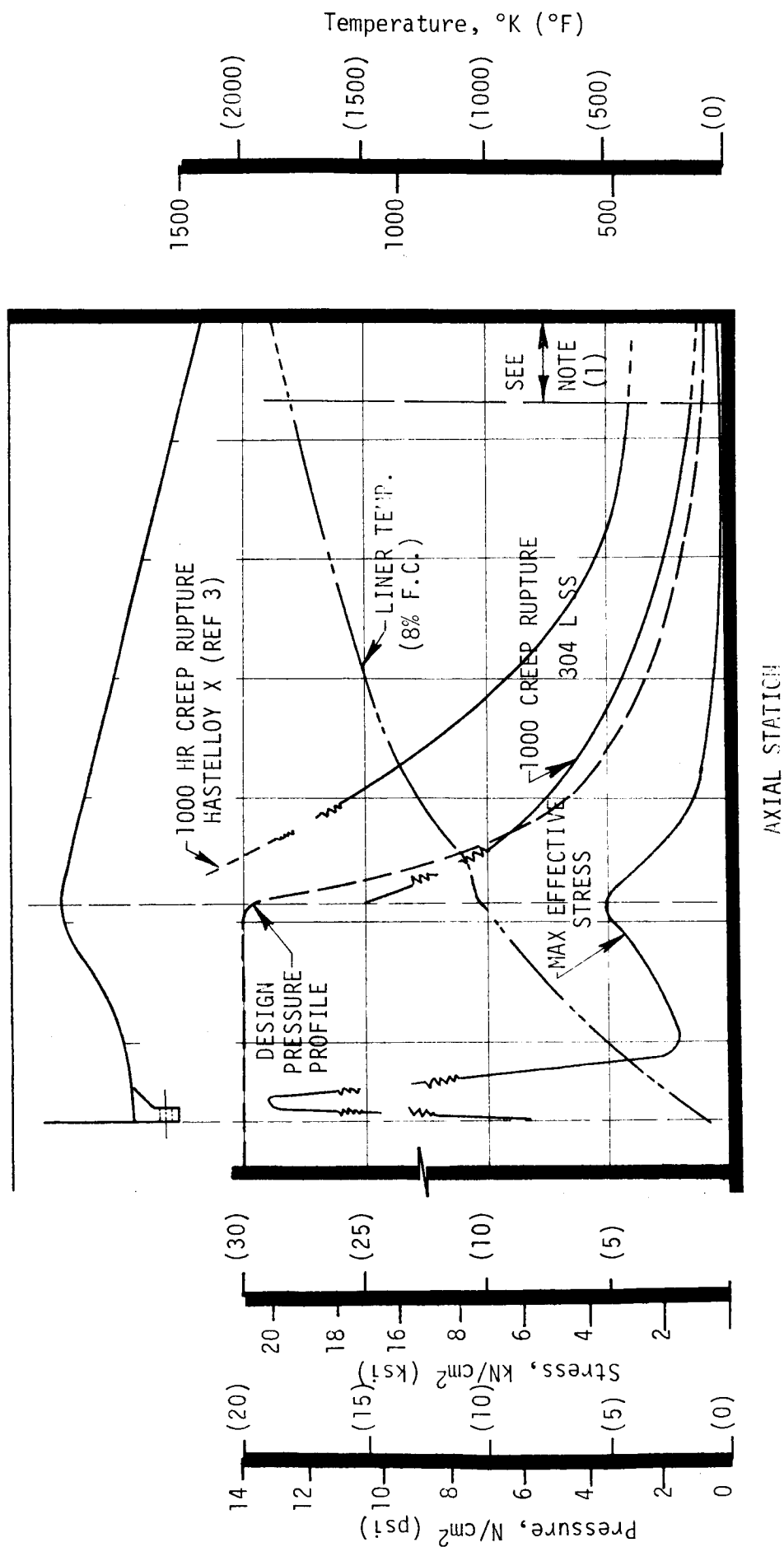
equivalent materials were also evaluated to determine their cyclic operating capability for this technology program. Austenitic stainless steel grade 304L was shown to offer adequate cycle life capability for the demonstration chambers.

The film-cooled chamber shell was analyzed using a finite element computer program developed at ALRC. The loads imposed on the structure were the chamber pressure distribution corresponding to  $12.4 \text{ N/cm}^2$  (18 psi) and the temperature profile shown in Figure III-30. Chamber temperatures expected with 8% film coolant flow were selected for this analysis.

Three major criteria were evaluated: (1) fatigue life, governed by start transient thermal stresses; (2) hoop strength of the shell elevated temperatures; and (3) creep-rupture life of the shell during extended steady-state operation. A profile of the resultant effective stresses for pressure loads is also shown in Figure III-30.

The effective stresses resulting from the thermal gradient across the shell thickness during a start transient were found to be within the elastic limit. With totally elastic strain, the number of cycles to failure were obtained from an S-N curve (stress amplitude vs cycles to failure) for the material of the application.

The maximum effective stress during steady-state operation occurs near the forward flange. In this area the flange and chamber wall temperatures remain relatively cool, resulting in high allowable tensile and compressive stresses. The stresses decrease rapidly toward the exit area and approach creep rupture as a critical failure mode due to the high nozzle temperatures. The applied stresses on the nozzle approach  $830 \text{ N/cm}^2$  (1200 psi); the 1000-hr creep rupture stress limit of 304L stainless is shown in Figure



NOTE (1) CREEP RUPTURE DATA IS NOT AVAILABLE ABOVE 1800°F

Figure III-30. Film-Cooled Chamber Loads and Resultant Stress Profiles

### III,C, Cooled Chambers (cont.)

III-30. Under the same conditions, Hastelloy X has an allowable strength of about  $2560 \text{ N/cm}^2$  (3700 psi), providing an increased positive margin against the failure mode.

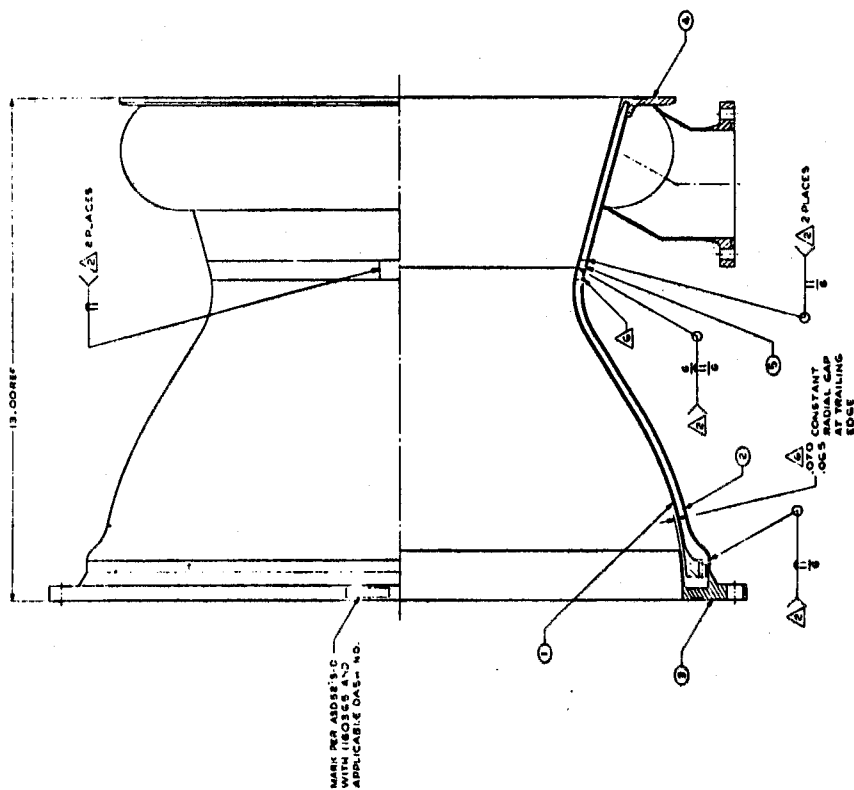
#### 3. Reverse Dump-Cooled Concept

##### a. Design Description

As noted in the comments portion of Figure III-26, each chamber concept that employs coolant channels is limited in allowable operating temperature for high cycle life operation by thermal stress rather than material allowable operating temperature. The internal shell is constrained against thermal expansion by the outer shell when the shells are joined by rigid ribs. This results in adverse strain of the inner liner. Detail design of the double wall, reverse dump-cooled chamber was directed to provide a design that would allow the inner and outer shells to be assembled without a rigid connecting member to resist thermal growth of the inner shell liner. The double wall chamber section of the reverse dump-cooled chamber reflects this approach.

The reverse dump-cooled chamber was designed with a regeneratively cooled chamber section composed of a flame and outer liner, and a thin-walled exit nozzle. Figures III-31 and III-32 show the cooled chamber section and the chamber assembly with nozzle. The two thrust chamber sections were connected with a V-band clamp to provide easy accessibility for installation of other nozzle designs which may have manifolds that obstruct attachment bolts. The hydrogen-cooled chamber section was designed to flow 12% of the fuel, starting at a plane 12.7 cm (5.0 in.) beyond the throat and flowing back to the injector face. At the injector end, the coolant was turned and injected parallel to the chamber wall for film cooling. The length and geometry of the film coolant sleeve for optimum coolant effectiveness and verification of chamber heat flux data were to be obtained from Task XVIII test data. Metering control orifices were used at the entrance of the liner to ensure uniform coolant flow distribution throughout the chamber.

- NOTES
1. **TESTING** 2. **TESTING** 3. **TESTING** 4. **TESTING** 5. **TESTING** 6. **TESTING** 7. **TESTING** 8. **TESTING** 9. **TESTING** 10. **TESTING** 11. **TESTING** 12. **TESTING** 13. **TESTING** 14. **TESTING** 15. **TESTING** 16. **TESTING** 17. **TESTING** 18. **TESTING** 19. **TESTING** 20. **TESTING** 21. **TESTING** 22. **TESTING** 23. **TESTING** 24. **TESTING** 25. **TESTING** 26. **TESTING** 27. **TESTING** 28. **TESTING** 29. **TESTING** 30. **TESTING** 31. **TESTING** 32. **TESTING** 33. **TESTING** 34. **TESTING** 35. **TESTING** 36. **TESTING** 37. **TESTING** 38. **TESTING** 39. **TESTING** 40. **TESTING** 41. **TESTING** 42. **TESTING** 43. **TESTING** 44. **TESTING** 45. **TESTING** 46. **TESTING** 47. **TESTING** 48. **TESTING** 49. **TESTING** 50. **TESTING** 51. **TESTING** 52. **TESTING** 53. **TESTING** 54. **TESTING** 55. **TESTING** 56. **TESTING** 57. **TESTING** 58. **TESTING** 59. **TESTING** 60. **TESTING** 61. **TESTING** 62. **TESTING** 63. **TESTING** 64. **TESTING** 65. **TESTING** 66. **TESTING** 67. **TESTING** 68. **TESTING** 69. **TESTING** 70. **TESTING** 71. **TESTING** 72. **TESTING** 73. **TESTING** 74. **TESTING** 75. **TESTING** 76. **TESTING** 77. **TESTING** 78. **TESTING** 79. **TESTING** 80. **TESTING** 81. **TESTING** 82. **TESTING** 83. **TESTING** 84. **TESTING** 85. **TESTING** 86. **TESTING** 87. **TESTING** 88. **TESTING** 89. **TESTING** 90. **TESTING** 91. **TESTING** 92. **TESTING** 93. **TESTING** 94. **TESTING** 95. **TESTING** 96. **TESTING** 97. **TESTING** 98. **TESTING** 99. **TESTING** 100. **TESTING**



NO.	WELD ROD	MIN. TENSILE STRENGTH
1	MC9951-1 RING	6
2	MC8350-1 LINER ASSY	4
3	MC9354-1 FLANGE	3
4	MC9351-1 LINER	2
5	MC9348-1 LINER	1
6	MC9348-1 LINER	1

**Figure III-31. Reverse Dump Cooled Chamber Section**



### III,C, Cooled Chambers (cont.)

The flame liner of the regeneratively cooled section is free to move axially and radially to compensate for the thermal expansion which will occur during firing. Four rows of deflector vanes were attached to the inside surface of the outer liner at an angle to the centerline of the chamber. These deflectors were used to space the inner and outer liners to provide the proper coolant channel height. The angular orientation of the spacers was designed to create a spiral flow pattern to redistribute any locally heated coolant prior to injection into the chamber for film coolant. A ring at the forward end of the flame liner contains secondary coolant distribution control orifices. It was designed to provide sufficient section modulus to prevent collapse of the thin wall flame liner due to the external coolant pressure. The calculated weight of this assembly, with a nonoptimized chamber to nozzle extension interface, is 18.4 kg (40.5 lb).

#### b. Thermal Analysis

The reverse dump-cooled chamber design utilizes a fraction of the fuel for regenerative coolant; flow is from the exit nozzle, at expansion area ratio 1.6, toward the injector. The regenerative hydrogen coolant is then injected as film coolant near the injector face plane.

The design was analyzed using the HEAT regenerative cooling program in conjunction with the new film cooling model of Reference 1. The predicted maximum (throat) gas-side wall temperatures for 5 and 10% fuel flow, in terms of passage depth and gas-side wall thickness, is shown in Figure III-34. The flow passage was treated as an annulus even though numerous vanes will span the gap between the inner and outer walls. Gas-side wall temperature was almost independent of wall thickness for the range of interest. Regenerative cooling with either 5 or 10% of the hydrogen and no film cooling, as would occur in a streak zone, resulted in a chamber wall temperature increase of nearly



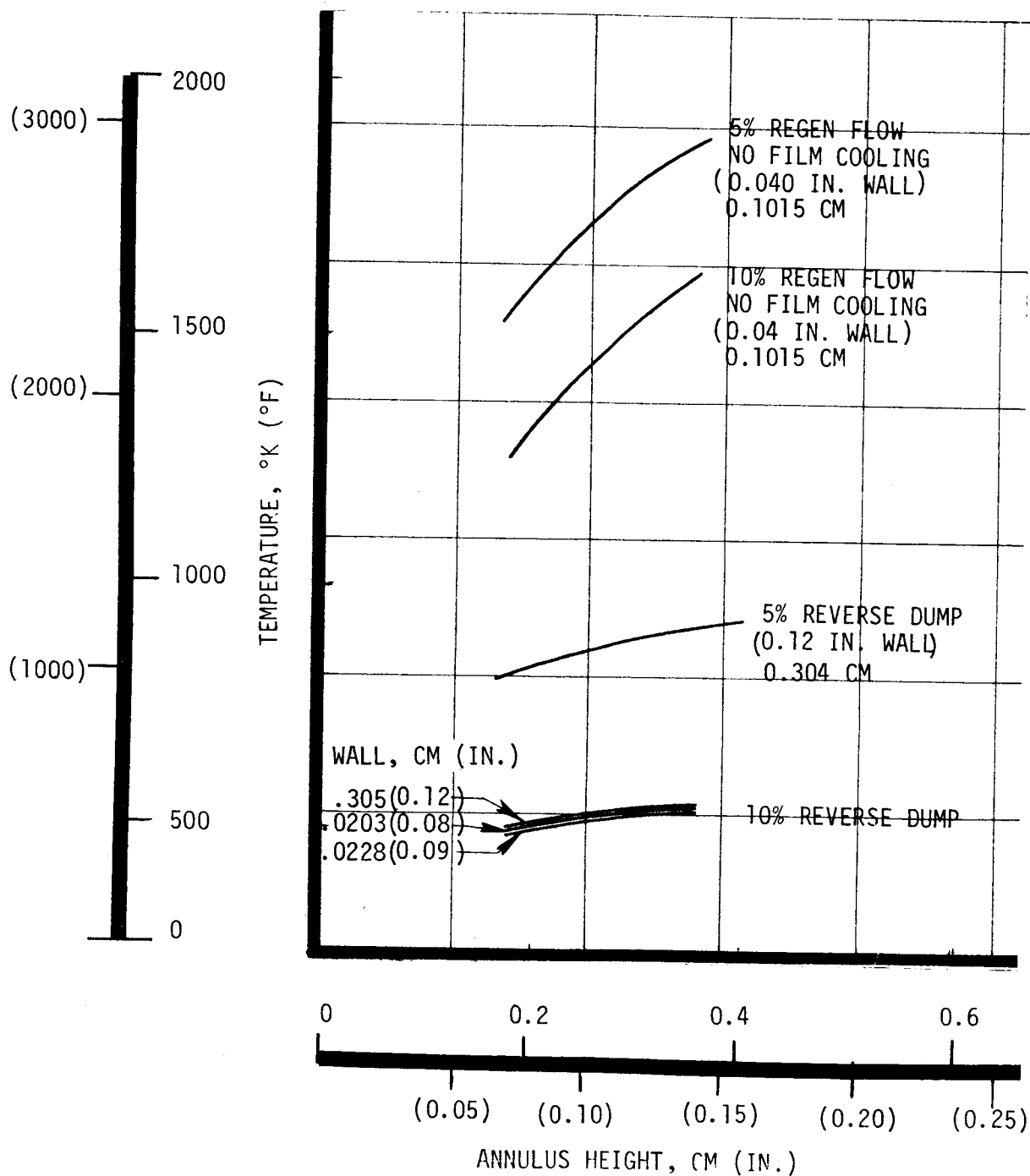


Figure III-33. Predicted Reverse Dump Cooled Chamber Throat Temperature

### III,C, Cooled Chambers (cont.)

830°K (1500°F). Injector-chamber compatibility and effective injection of the hydrogen film coolant are as important with this concept as with the film-cooled design.

The calculated chamber temperature profile used for the structural analysis is shown in Figure III-34. Two related analyses were conducted to define the flange to shell temperature gradient at the aft end of the regenerative section and the maximum collapsing pressure differential between the coolant and the chamber.

The film coolant ring used with either cooled chamber resembles a regeneratively cooled shell which must be film cooled. The predicted gas-side temperature, coolant pressure drop, and velocity in terms of axial length of the film coolant ring for film coolant flow rates on the inner side of the ring of 0 to 5% of the total fuel flow are shown on Figure III-35. These results, used as a guide for detail design, were obtained with a 0.127 cm (0.050-in.)-wide coolant passage flowing 10% of the fuel as regenerative coolant. A short length coolant sleeve or secondary coolant flow to provide a barrier for the coolant sleeve will be required.

#### c. Structural Analysis

The design and structural analyses were conducted to identify materials, configuration, and thermal operating limits commensurate with 100,000 thermal cycle operation. Nickel base superalloys such as Hastelloy X were found to be near optimum for this application. More easily fabricated but thermally equivalent materials were also evaluated to determine their cyclic operating capability for this technology program. Austenitic stainless steel grade 304L was shown to offer adequate cycle life capability for the demonstration chambers.

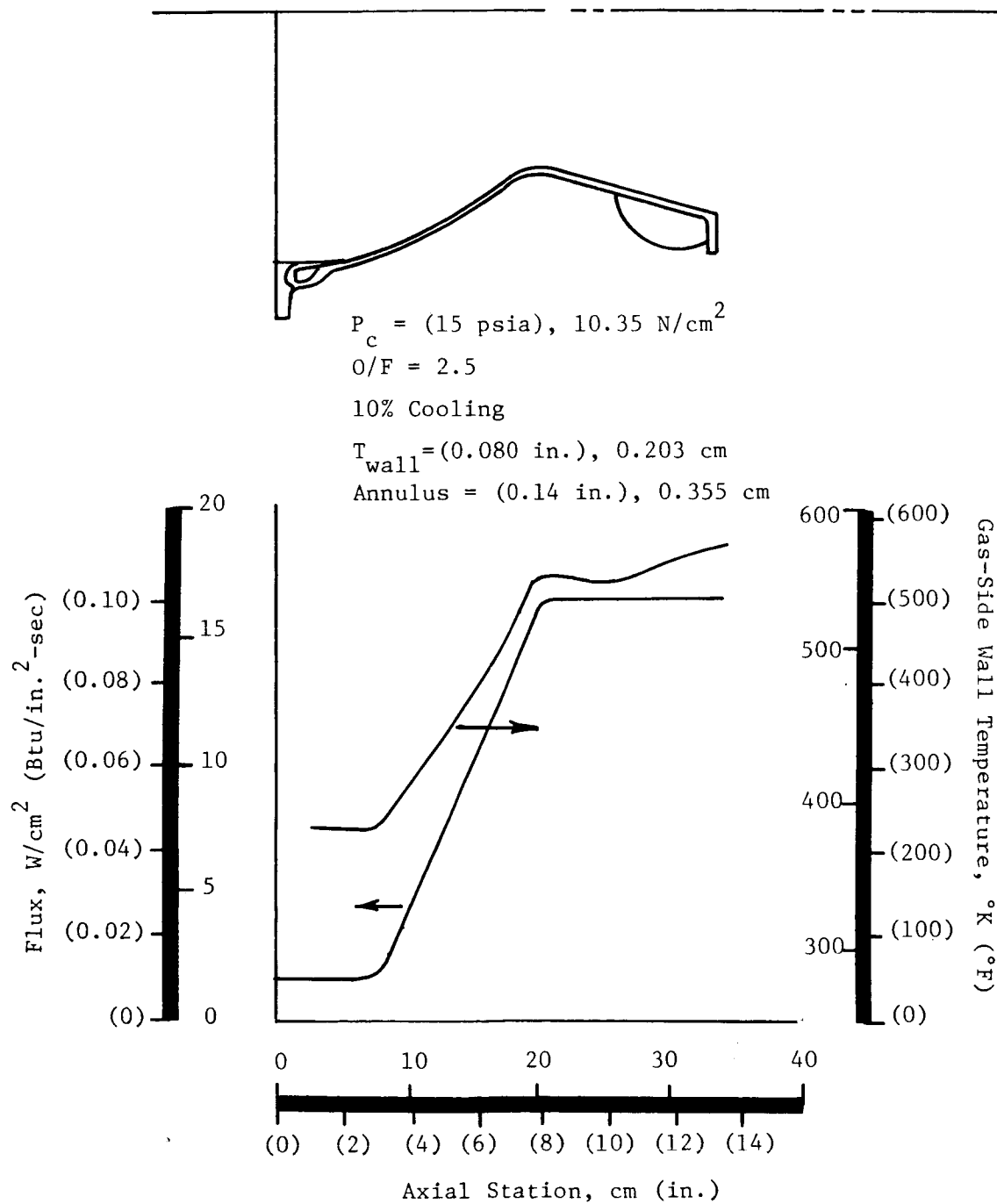


Figure III-34. Reverse Dump Cooled Chamber Temperature Profile

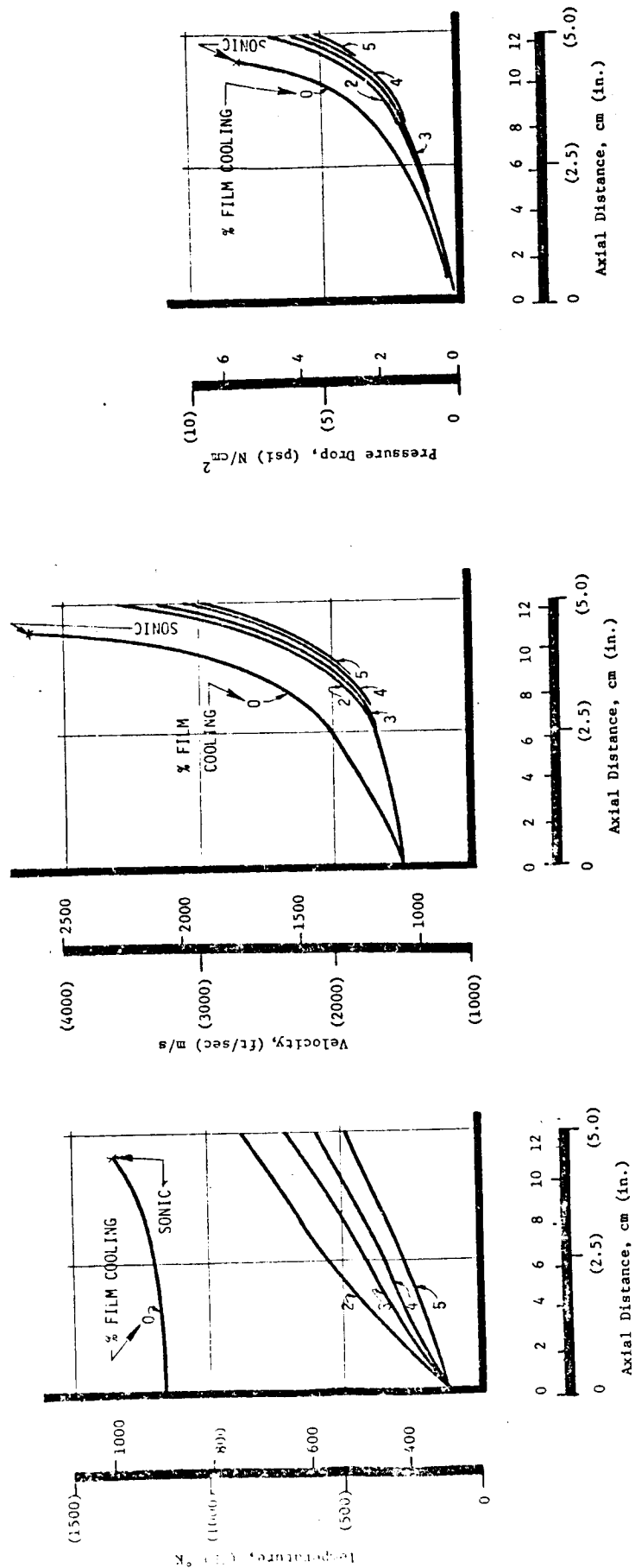


Figure III-35. Predicted Film Coolant Ring Thermal, Hydraulic, and Injection Characteristics

### III,C, Cooled Chambers (cont.)

A stress analysis of the reverse dump-cooled combustion chamber was conducted to investigate three critical failure modes. The failure modes investigated were: buckling of the free-floating inner wall due to the external pressure exerted by the coolant; yielding of the alignment and flow diverting vanes; and the fatigue life of the inner liner at the critical aft flange location. The aft flange would not necessarily be required for a flight configuration; however, the structural effects were considered representative of the condition that would exist with a coolant distribution manifold on a flight configuration.

The calculated minimum margins of safety for selected critical components were:

<u>Item</u>	<u>Mode of Failure</u>	<u>M.S.</u>
Inner liner	Buckling	0.25*
Forward ring of inner liner	Buckling	1.88*
Directional vanes	Yield bending	0.48
Liner fatigue life	Fatigue cracks	$1.2 \times 10^5$ cycles**

The thermal stress profiles of the aft section of the inner liner, where the maximum temperatures occur, are shown on Figure III-36. At the aft attachment flange, the thermal stresses are beyond the elastic limit of the 304L stainless steel liner. The computer analysis calculated an effective strain of 0.21% and an effective stress of  $18,000 \text{ N/cm}^2$  (26,000 psi) for the design configuration and thermal conditions. The effective stress (distortional energy) method was used to compare stresses in a triaxial stress field to uniaxial material properties. The predicted fatigue life for this

---

\*Based on an external pressure of  $20.7 \text{ N/cm}^2$  (30 psi),  $13.8 \text{ N/cm}^2$  (20 psi x 1.5 factor of safety) and an internal liner temperature of 925°K (1200°F).

\*\*Based on the structural properties of 304L.

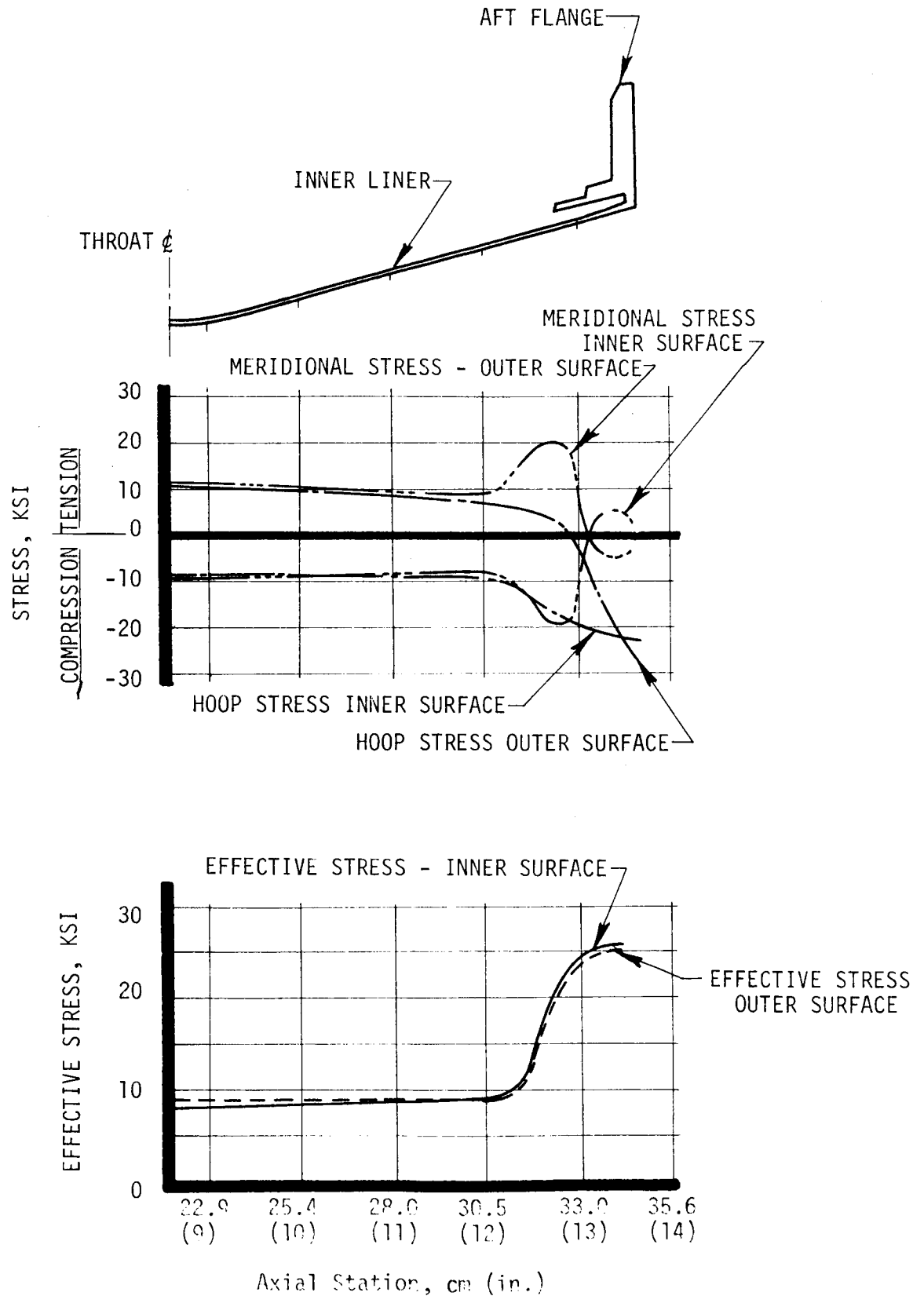


Figure III-36. Reverse Dump Cooled Chamber Liner Thermal Stress

### III,C, Cooled Chambers (cont.)

strain was 120,000 cycles for the 304L stainless steel liner as shown in Figure III-37. The high cycle fatigue life of the liner is improved by use of a higher yield strength material such as Hastelloy X. The higher yield strength of the Hastelloy results in cyclic operation within the elastic range after an initial plastic strain of the liner. This operating mode increased the predicted fatigue life of the inner shell to over  $10^6$  cycles as shown in Figure III-37.

#### d. Hydraulic Analysis

A flow distribution analysis of the reverse dump-cooled chamber design was conducted. Nominal chamber design conditions used in this analysis were as follows:

Chamber coolant medium	Gaseous hydrogen
Coolant inlet temperature	300°K (540°R)
Coolant outlet temperature	340°K (615°R)
Coolant inlet pressure	13.1 N/cm <sup>2</sup> (19 psia)
Chamber pressure	10.3 N/cm <sup>2</sup> (15 psia)
Coolant flow rate	0.062 Kg/sec (0.137 lbm/sec) (12%)

The calculated pressure losses for the coolant are shown in Table VII.

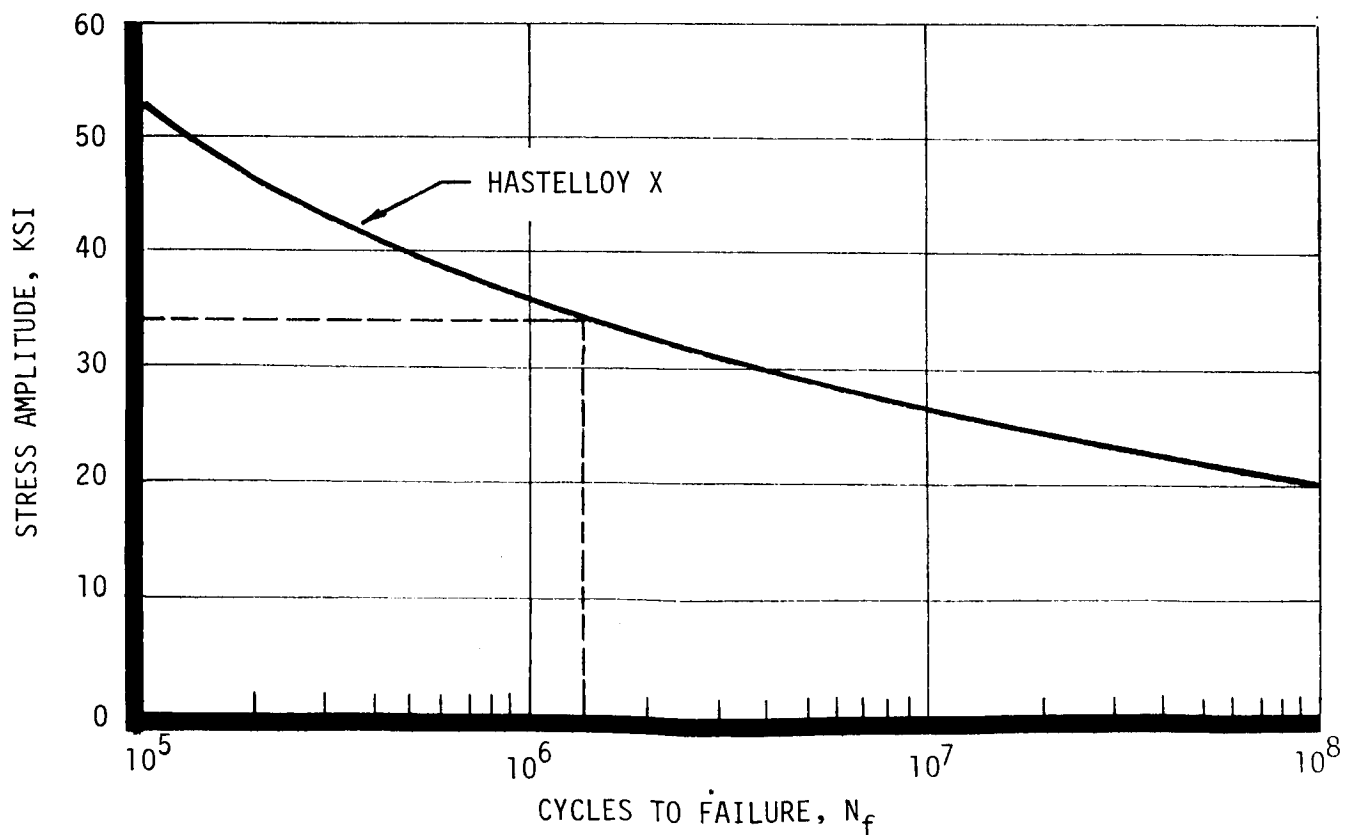
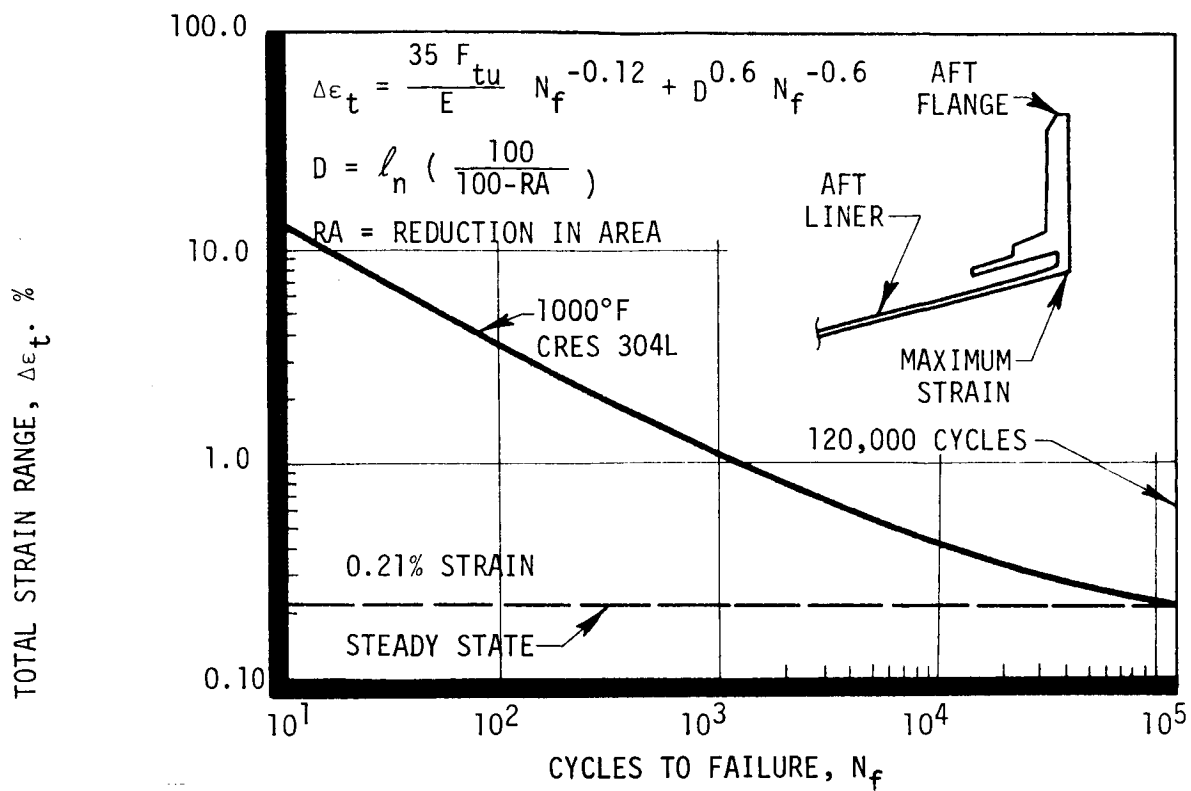


Figure III-37. Effect of Applied Strain on Cycle Life of Reverse Dump Cooled Liner



### III,C, Cooled Chambers (cont.)

TABLE VII

REVERSE DUMP COOLED CHAMBER PRESSURE LOSS DISTRIBUTION

	<u>N/cm<sup>2</sup></u>	<u>psia</u>
Chamber Inlet	0.070	0.1
Inlet Manifold	0.14	0.2
Inlet Metering Orifice	0.21	0.3
Chamber Friction & Turning Turbulence	0.69	1.0 (approximate)
Exit Metering Orifice & Forward Flange Plenum	0.55	0.8
<hr/>		
Total Circuit	1.66	3.3

The design philosophy for this chamber was to introduce the fuel coolant at a low velocity to minimize dynamic head effects at the distribution circuit inlet. A moderate pressure loss was introduced at the inlet metering orifice to obtain positive flow control to achieve a uniform circumferential coolant distribution in the chamber coolant passages. The chamber coolant passage pressure drop was assumed to be uniform as a result of the uniform circumferential flow distribution. A higher pressure drop was taken at the exit metering orifice at the forward flange to maintain a uniform chamber internal (hot gas side) film coolant distribution.

The criterion for hydraulic design was to progressively increase the gas velocity. Other ALRC gas/gas injector and chamber distribution manifolds have employed this technique with success.

### III,C, Cooled Chambers (cont.)

This analysis was conducted for equal chamber wall and film coolant sleeve temperatures. If the coolant sleeve is heated relative to the chamber wall, the thermal expansion will reduce the injection gap, thereby increasing the injection velocity and the injection pressure drop. Thrust chamber coolant flow will be balanced for steady-state coolant sleeve temperatures.

#### 4. Thrust Chamber Fabrication

Work on the Low  $P_c$  program was terminated before any cooled chamber fabrication work was performed.

### III, Technical Discussion (cont.)

#### D. CATALYTIC IGNITER

##### 1. Design Description

The catalytic igniter was designed as a staged combustion device which flowed only a small portion of the igniter propellants through the catalyst bed. The remainder of the igniter propellants are injected into the bed effluent. The staged mixing technique was used to keep the size of the catalyst bed and the bed pressure drop small and to initiate rapid reaction with the catalyst effluent under controlled conditions.

The catalytic igniter design shown in Figure III-38 employed Shell 405 as the catalyst for a nominal O/F = 1 mixture of oxygen and hydrogen. The secondary oxygen was introduced into the reactants through an annular orifice to provide a uniform transition from oxygen at the outer wall to an overall chamber mixture ratio of 50. Hydrogen was used to convectively cool the chamber and throat to provide extended duration operating capability and to provide fuel for further reaction of the 5 oil mixture ratio.

Each propellant flow into the igniter entered a plenum in a valve adapter assembly. The propellant flow was then divided with a portion of the flow going to the injector and then through the catalyst bed. The remainder of the oxygen entered the chamber area to mix with the catalyst bed effluent and the remainder of the hydrogen flowed around the chamber as coolant. Flow proportioning for the primary (catalyst bed) and secondary circuits was accomplished with balance orifices.

Propellant distribution and mixing were accomplished with an injector similar in concept to the high pressure program impinging element injector. Nineteen through-flow oxygen streams were impinged by hydrogen flowing through a metering and distribution platelet. The propellant mixture from each element was then impinged on a plate and redistributed through four smaller orifices near the catalyst pack inlet.

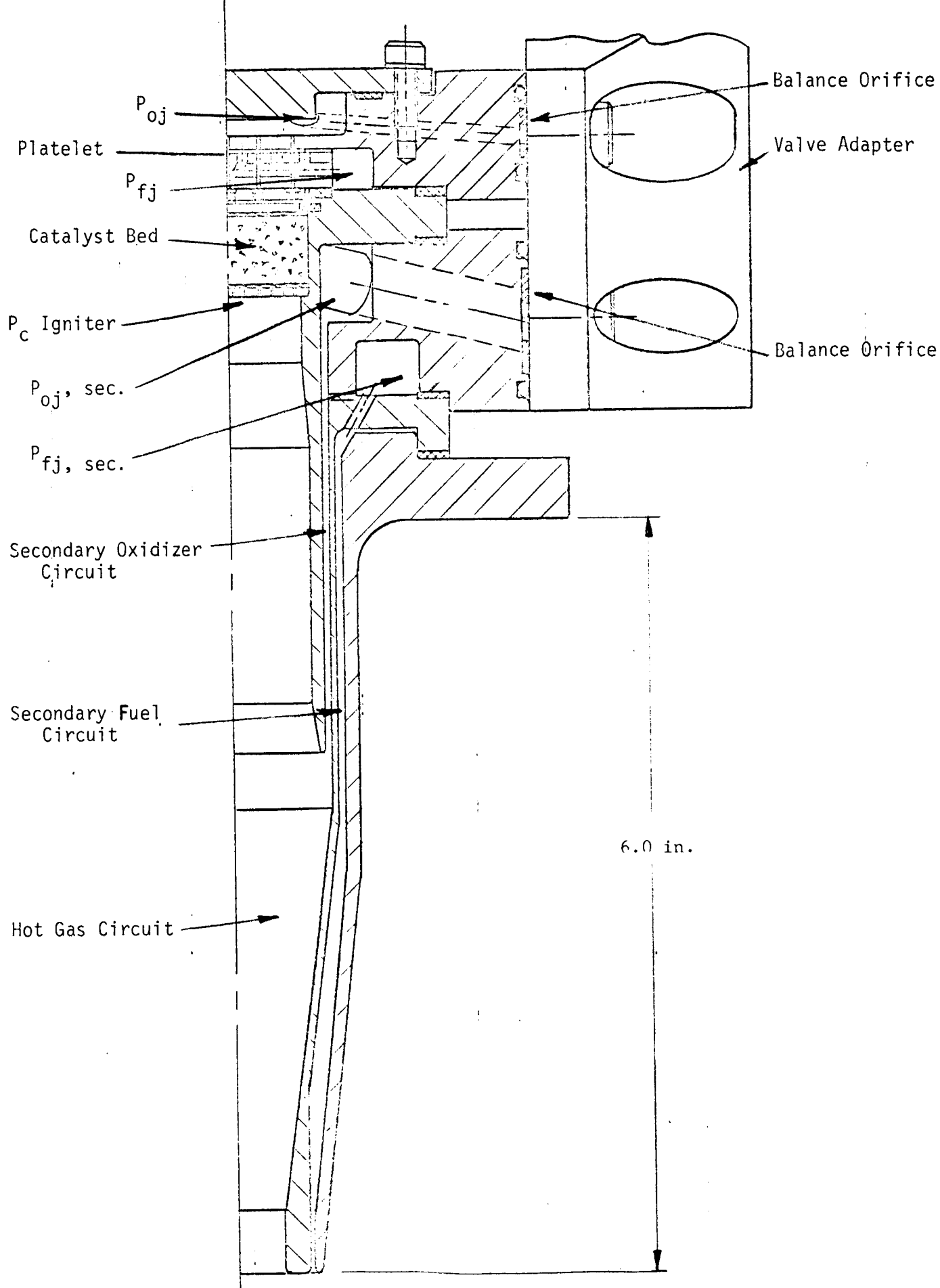


Figure III-38. Catalytic Igniter Assembly

### III, D, Catalytic Igniter (cont.)

The catalyst pack assembly was formed by an "aft trap" (a perforated plate used to support the bed), a screen, the catalyst, and an inlet screen. These components and materials were assembled into a flanged sleeve which also served to form the secondary oxygen flow annulus. The sleeve length was designed to introduce the secondary oxygen midway between the igniter chamber throat and the catalyst bed. Increased mixing of the secondary oxygen is accomplished, if required, by remachining the sleeve to introduce the secondary oxygen nearer the catalyst bed.

The igniter assembly was designed to be interchanged with the electrical igniter of Contract NAS 3-14348 without injector hardware changes. Features of the design are summarized below:

Type:	Catalyst bed pilot with secondary oxygen augmentation
Catalyst:	Shell 405, 14-18 mesh
Injector:	Brazed stainless steel with premix elements
Catalyst Bed:	3.2 cm (1.26 in.) dia by 1.27 cm (0.5 in.) long. Length can be increased to allow use of additional catalyst or an inert premix and distribution bed.
Propellant Flows:	Through catalyst - $\dot{w}_O = 0.000568 \text{ Kg/sec}$ (0.00125 lb/sec) $\dot{w}_F = 0.000568 \text{ Kg/sec}$ (0.00125 lb/sec)  Augmenting oxygen - 0.0278 Kg/sec (0.06126 lb/sec)  Hydrogen coolant - 0.0052 Kg/sec (0.00115 lb/sec)
Steady-State Effluent Temperature:	Through catalyst pack = 1280°K (2300°R) (O/F = 1.0)  Secondary oxygen introduction location can be varied consistent with chamber heating and secondary reaction requirements.

### III, D, Catalytic Igniter (cont.)

#### 2. Thermal Analysis

A thermal analysis of the hydrogen-cooled igniter chamber was conducted to determine the steady-state operating temperatures. The peak igniter chamber gas-side wall temperature was predicted to be 700°K (800°F) at the throat station.

#### 3. Hydraulic Analysis

A hydraulic analysis of the catalytic igniter was performed to size the secondary fuel coolant circuit, the secondary oxidizer circuit, and the hot gas core for design flow rates, pressures, and mixture ratios. The analysis was conducted for two conditions: with and without back pressure due to main chamber combustion. The design technique used was to size circuits for design flow rates in the zero back pressure case (core and fuel coolant annulus throats choked), and then check the change in flow splits (mixture ratio shift) caused by finite back pressure (core and fuel coolant annulus throats unchoked). The objective of this analysis was to identify any potentially adverse operating conditions which would not be shown by igniter-only tests.

The back pressure case analysis was conducted for two basically different system designs. Initially, a "soft" constant feed pressure system was assumed, i.e., the oxidizer and fuel flow rates were reduced when the back pressure reached its steady-state value. The reductions were calculated and the core and overall mixture ratios examined for any variance from the design values. The second phase of the back pressure analysis considered a system in which there were "critical" nozzles upstream of the oxidizer and fuel inlet valves. The nozzles ensure constant fuel and oxidizer flow rates through the system with and without back pressure. This phase of the analysis determines if a core mixture ratio shift will occur for the constant flow rate system after steady-state engine chamber pressure is developed.

### III, D, Catalytic Igniter (cont.)

A system schematic showing the basic interrelated hydraulic considerations for this analysis is shown in Figure III-39.

The results of the igniter hydraulic analysis showed, when chamber pressure develops with the variable flow "soft" system, the fuel coolant flow rate is reduced to approximately 68% of design value, while the core flow rate is reduced to approximately 72% of design value. The mixture ratio through the catalyst and the mixture ratio after the secondary oxygen is introduced are maintained at the initial design conditions. A slight increase in overall mixture ratio results from the reduction of hydrogen coolant.

The constant flow rate system showed an increase of throat inlet stagnation pressure as back pressure developed. The fuel flow through the catalyst bed was calculated to be approximately 2% of the design fuel coolant flow rate, which would lower the bed mixture ratio to a value of approximately 0.85. Satisfactory operation of this igniter is anticipated with both fixed flow and fixed pressure feed systems with and without back pressure.

#### 4. Fabrication

Components for one igniter assembly with spare seal gaskets, balance orifices, and catalyst bed screens and support plates were fabricated. A mounting adapter, to simulate the injector interfaces, was also produced. The completed igniter assembly is shown in Figure III-40.

The igniter injector design employed a precision fuel distribution and metering platelet bonded between a fuel manifold plate and the injector face plate. This platelet was produced by the photoetch process and was then bonded into the injector assembly. Other components were produced by lathe, mill, and drill operations.

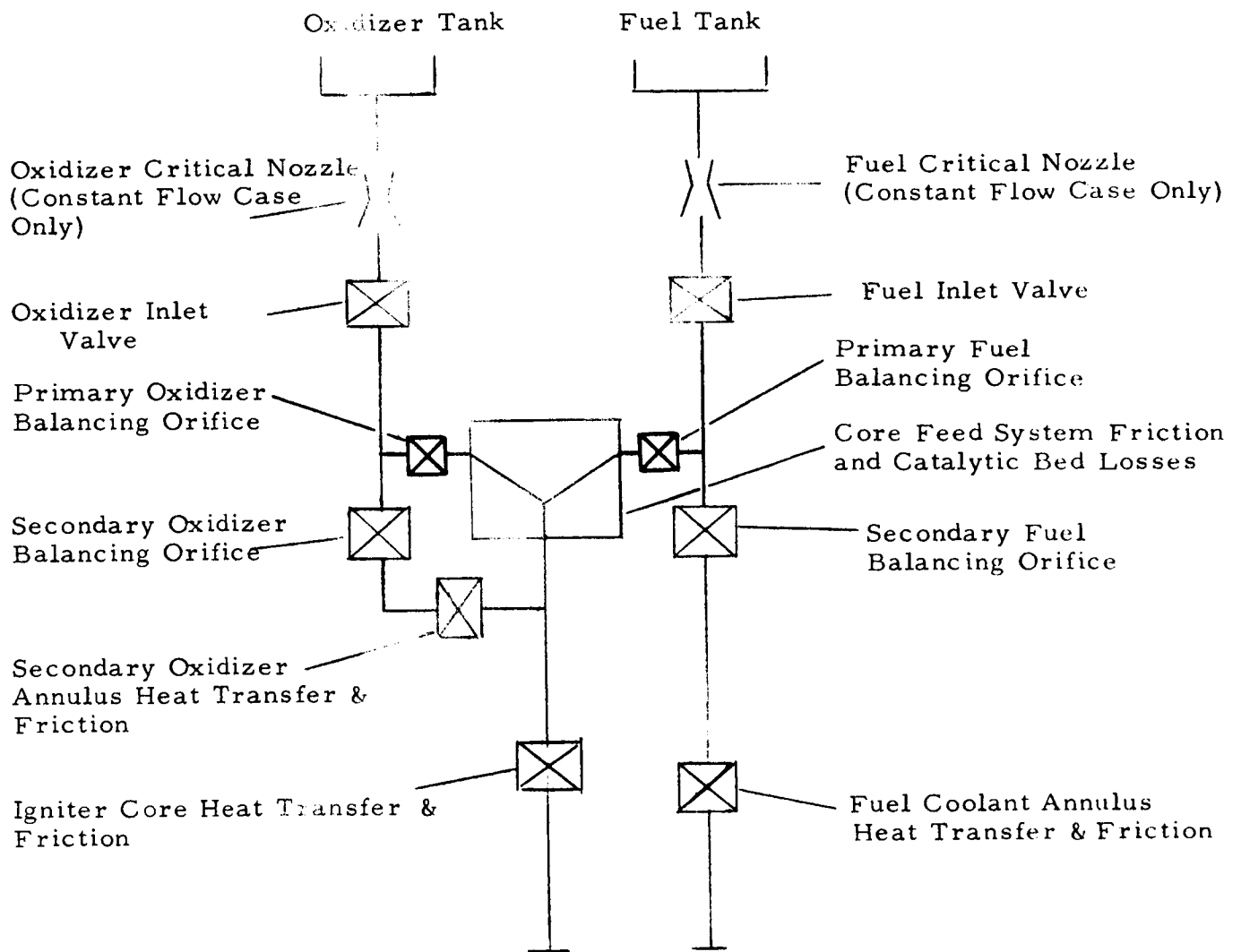


Figure III-39. Catalytic Igniter Hydraulic Analysis Schematic



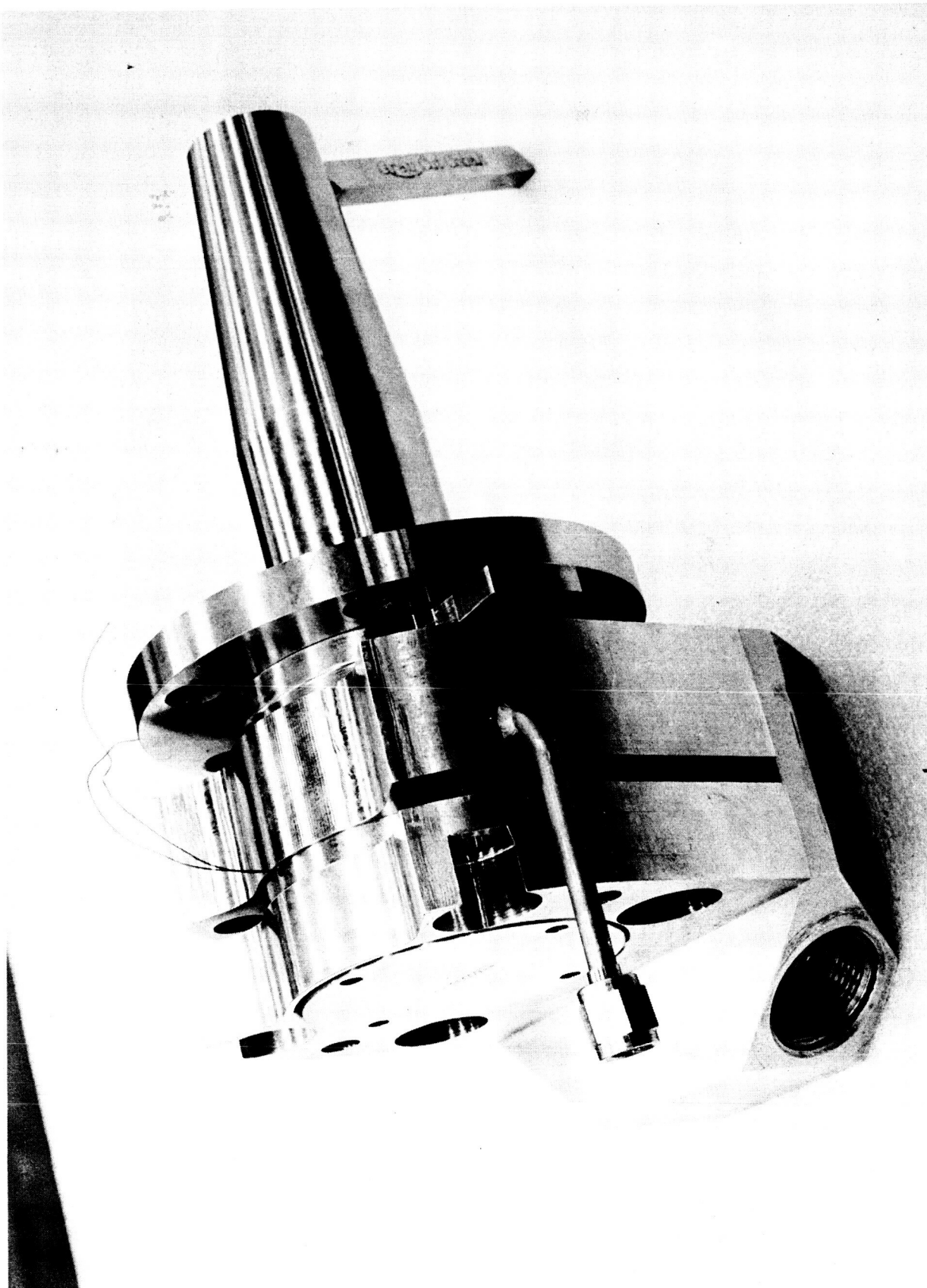


Figure III-40. Catalytic Igniter Hardware

### III, D, Catalytic Igniter (cont.)

#### 5. Test Results

Subsequent to completion of fabrication, the low  $P_c$  catalytic igniter was prepared for testing. Preparations consisted of assembly of the components, installation of the flow "split" balance orifices, and packing of the catalyst bed. The igniter test position in Bay 1 of the Physics Laboratory was modified to accept the catalytic unit. The modifications required consisted of the rerouting of propellant lines, repositioning of the igniter valves, and installation of instrumentation and the associated electrical cabling. Before testing was begun, each propellant circuit was cold flowed for calibration. A propellant simulant was used for the flow calibrations (i.e., nitrogen simulating the oxygen and helium simulating the hydrogen), so combustible mixtures of gases would not accumulate in the vacuum system. When enough flow data were available from the calibration tests and each circuit was considered balanced, testing was initiated.

The test program consisted of seven test series, including two series where the effects of cold hardware and cold propellants were investigated. A total of 151 tests were performed.

Because of the number of tests conducted and the quantity of data measured, the following discussion of the testing and the results have been divided into seven test sections. A description of the tests and the test results are contained in the following paragraphs.

#### Test Series 1 - Checkout Tests

The initial investigations with the Low  $P_c$  catalytic igniter consisted of five tests conducted to evaluate operating characteristics. The data resulting from these tests is presented in Table VIII. The upstream bed thermocouple (nearest to the injector face) did not respond during the first

TABLE VIII

## CATALYTIC IGNITER DATA - TEST SERIES 1 AND 2

Test Number IG-2C-	$\dot{w}_{O_2}$ -T, lbm/sec	$\dot{w}_{H_2}$ -T, lbm/sec	MR, Overall	$\dot{w}_{O_2}$ -Bed, lbm/sec	$\dot{w}_{H_2}$ -Bed, lbm/sec	MR, Bed	$P_c$ , psia	Duration, sec	Delay, sec
<u>Test Series 1</u>									
101	0.063	0.013	4.85	0.002	0.002	1.0	--	0.2	--
102	0.063	0.013	4.85	0.002	0.002	1.0	--	0.2	--
103	0.063	0.013	4.85	0.002	0.002	1.0	--	1.0	--
104	0.063	0.013	4.85	0.002	0.002	1.0	--	5.0	--
105	0.084	0.017	4.94	0.003	0.003	1.0	--	2.0	0.760
<u>Test Series 2</u>									
106	0.084	0.017	4.94	0.003	0.003	1.0	--	2.0	--
107	0.084	0.017	4.94	0.003	0.003	1.0	--	2.0	--
108	0.125	0.013	9.62	0.004	0.002	2.0	--	2.0	1.64
109	0.156	0.013	12.00	0.005	0.002	2.5	--	2.0	0.09

\*NOTE: The ignition delay is defined as the time from first action in the oxidizer manifold (i.e., the lagging propellant) to first indication of involvement of the secondary oxygen in a combustion process.

### III, D, Catalytic Igniter (cont.)

two tests, reached 356°K (181°F) at the end of Test 103, and 495°K (431°F) at the end of Test 104; the test durations are shown in Table VIII. These results indicate a very low level of propellant reaction within the bed and no involvement of the secondary oxygen in the combustion process.

The total propellant weight flow was measured for Test 105 and it behaved quite differently. For the first 760 msec, the traces indicate a very low level of bed activity with PoJ-2 running at  $11.2 \text{ N/cm}^2$  (16.3 psia). The upstream bed thermocouple responded very early in the test and indicated a temperature of 426°K (307°F) at 760 msec. At that point, the photocell indicated ignition and PoJ-2 rose to  $12.4 \text{ N/cm}^2$  (18.0 psia). The bed thermocouple indicated a gradual temperature rise to 523°K (481°F) at the end of 2.0 sec. The bed responded to the increased propellant flow rate and reached a higher temperature in 2.0 sec (523°K, 481°F) than it did in the 5.0 sec of the previous test (495°K, 431°F). Once again, a low level of propellant reaction in the bed is indicated. The photocell indicates that the secondary oxygen became involved at 760 msec into the test.

Posttest inspection of the igniter revealed neither damage to any component nor evidence of heating within the igniter. In preparation for the next series of tests, the catalyst was replaced with fresh material as a precautionary measure, four holes were drilled in the inner sleeve immediately downstream of the bed to introduce secondary oxygen nearer to the catalyst bed, and a thermocouple was installed in the combustion chamber and a second was positioned on the igniter nozzle as additional witness instrumentation.

#### Test Series 2 - Evaluation of Drilled Sleeve

This series consisted of four tests and was conducted primarily to evaluate the introduction of secondary oxygen nearer to the catalyst bed. The data from these tests is also presented in Table VIII. Testing commenced with

### III, D, Catalytic Igniter (cont.)

the flow rates and mixture ratios the same as those which resulted in ignition during Test Series 1, Test 105. As the data show, ignition was not achieved, so the test was repeated. Again, there was no secondary reaction. The third test (Test 108) was conducted with the mixture ratio doubled and the oxygen content increased in an attempt to improve responsiveness. Secondary oxygen reaction occurred at 1.6 sec. The overall MR was further increased and secondary oxygen reaction occurred at 0.09 sec.

Posttest inspection of the igniter revealed neither damage nor unwanted heating of interior components. Because the holes drilled in the chamber sleeve did not appear to enhance operation, they were welded closed.

#### Test Series 3 - Weight Flow and Mixture Ratio Evaluation

This series consisted of 11 tests conducted with progressively increasing propellant weight flows and mixture ratios. The resulting data are shown in Table IX. The trend of data from these tests indicated that either higher than design values of propellant flow rate or mixture ratio were required for proper operation of the igniter. The catalyst bed temperatures, which were reached near the end of the test periods, were lower than expected, indicating that the catalyst bed mixture ratio was lower than designed.

Posttest inspection of the igniter revealed some damage to the igniter injector face plate. The damage was limited to the final distribution plate which was removed prior to the next test series. With this plate removed, the propellants will be injected into the bed more coarsely than originally designed. Also with this plate removed, the hydraulic calibration and propellant "splits" between the bed and secondary circuits are no longer valid. The next series of tests was initiated to examine operation of the catalyst bed alone for bed response and calibration data.

TABLE IX

## CATALYTIC IGNITER DATA - TEST SERIES 3

Test Number	$\dot{w}_{O_2}$ -T, lbm/sec	$\dot{w}_{H_2}$ -T, lbm/sec	MR, Overall	$\dot{w}_{O_2}$ -Bed, lbm/sec	$\dot{w}_{H_2}$ -Bed, lbm/sec	MR, Bed	$P_c$ *** psia	Duration, sec	Delay,* sec
110	0.063	0.013	4.85	0.002	0.002	1.0	--	0.3	--
111	0.063	0.013	4.85	0.002	0.002	1.0	--	0.3	--
112	0.063	0.013	4.85	0.002	0.002	1.0	--	2.0	--
113	0.093	0.019	4.89	0.003	0.003	1.0	--	2.0	--
114	0.093	0.019	4.89	0.003	0.003	1.0	7.5	2.0	0.74
115	0.093	0.019	4.89	0.003	0.003	1.0	7.7	2.0	0.25
116	0.093	0.019	4.89	0.003	0.003	1.0	7.9	2.0	0.68
117	0.093	0.013	7.15	0.003	0.002	1.5	8.4	2.0	0.59
118	0.110	0.013	8.46	0.004	0.002	2.0	9.2	2.0	0.12
119	0.110	0.016	6.88	0.004	0.002	2.0	10.3	2.0	0.39
120	0.110	0.016	6.88	0.004	0.002	2.0	10.8	2.0	0.03**

\*NOTE: The ignition delay is defined as the time from first action in the oxidizer manifold, i.e., the lagging propellant, to first indication of involvement of the secondary oxygen in a combustion process.

\*\* Hot-bed restart.

\*\*\* Inferred from PoJ2.

### III, D, Catalytic Igniter (cont.)

#### Test Series 4 - Catalyst Bed Evaluation

This series consisted of 26 tests conducted with propellant flow to the catalyst bed alone. A set of small critical-flow venturis were installed in the propellant feed circuits to meter fuel and oxidizer to the bed only. The secondary circuits were "blanked off" for these tests. The data resulting from these tests are presented in Table X.

A posttest disassembly of the igniter revealed evidence of heating on the combustion chamber sleeve, but otherwise the igniter components were undamaged. In preparation for the next test series, the bed was repacked with fresh catalyst and the proper orifice was installed to achieve the correct flow proportioning between the catalyst bed and secondary oxygen circuit. The secondary hydrogen circuit was left closed for these tests. A thermal analysis indicated that there was sufficient margin of safety to test the igniter, without cooling, for short durations. The igniter was reassembled and mounted in place in preparation for the next test series.

#### Test Series 5 - Secondary Oxygen Injection Evaluation

Twenty-one tests were conducted during this series to evaluate secondary oxygen injection. The data are presented in Table XI. Testing was started with both propellant flow rates set at the design values. The first tests resulted in a low level of bed activity, i.e., the bed thermocouples measured temperatures not greater than 589°K (600°F) (Tests 147 through 151). The flow rate of oxidizer was increased and bed activity improved as the bed temperatures reached approximately 812°K (1000°F) during the next four tests (Tests 152 through 155). As testing progressed, the oxidizer flow rate and bed mixture ratio were steadily increased until secondary reactions were obtained (Tests 160 through 167). Catalyst bed temperatures were in the range of 922°K to 1255°K (1200 to 1800°F) during these tests.

TABLE X

## CATALYTIC IGNITER DATA - TEST SERIES 4

Test Number IG-2C-	$\dot{w}_{O_2}$ -B, lbm/sec	$\dot{w}_{H_2}$ -B, lbm/sec	MR, Bed	Duration, sec	Test Results
121	0.0013	0.0013	1.00	0.15	No reaction in catalyst bed (1)
122	0.0013		1.00	0.15	No reaction in catalyst bed (1)
123	0.0014		1.08	0.25	Reaction obtained
124	0.0011		0.85	0.25	No reaction (2)
125	0.0011		0.85	0.25	No reaction (2)
126	0.0013		1.00	0.25	Reaction obtained
127	0.0013		1.00	0.50	Reaction obtained (3)
128	0.0012		0.92		
129		0.0013	0.92		
130		0.0012	1.00		
131		0.0013	0.92		
132					
133					
134					
135					
136					
137					
138					
139					
140					
141					
142					
143	0.0012		0.92	0.50	
144	0.0013		1.00	1.50 (4)	
145	0.0013		1.00	1.50 (4)	
146	0.0013	0.0013	1.00	1.50 (4)	Reaction Obtained (3)

- (1) Bed reactions were not obtained because a later data review revealed that the oxidizer valve did not open.
- (2) Reactions were not obtained within the test duration at low mixture ratio, i.e., less than 1.0.
- (3) Bed temperatures, during the repeat tests, and the 1.50 sec tests did not rise higher than 1800°F.
- (4) The longer durations resulted in the same bed temperatures, so thermal equilibrium had been reached.



TABLE XI

## CATALYTIC IGNITER DATA - TEST SERIES 5

Test Number	$\dot{w}_{O_2}$ -T, lbm/sec	$\dot{w}_{O_2}$ -sec, lbm/sec(2)	$\dot{w}_{O_2}$ -Bed, lbm/sec(2)	$\dot{w}_{H_2}$ -Bed, lbm/sec(3)	MR, Bed	Duration, sec	$P_c$ psia	Delay, sec(4)
147	0.063	0.061	0.0020	0.0022	0.91	0.80	Bed	Reaction Only
148	0.063	0.061	0.0020	↑	0.91	0.80	Bed	Reaction Only
149	0.070	0.068	0.0022		1.00	0.80	Bed	Reaction Only
150	0.070	0.068	0.0022		1.00	0.80	Bed	Reaction Only
151	0.070	0.068	0.0022		1.00	0.80	Bed	Reaction Only
152	0.080	0.078	0.0026		1.18	0.90		
153	0.080	0.078	0.0026		1.18	↑		
154	0.080	0.078	0.0026		1.18			
155	0.080	0.078	0.0026		1.18	↓		
156	0.100	0.097	0.0032		1.45			
157	0.100	0.097	0.0032		1.45	0.90		
158	0.100	0.097	0.0032	↓	1.45	1.00	Bed	Reaction Only
159	0.080	0.078	0.0026		1.18	↑	15.1	
160	0.080	0.078	0.0026		1.18			
161	0.100	0.097	0.0032		1.45	↓	Bed	Reaction Only
162	0.115	0.111	0.0037		1.68		17.4	0.095
163	0.117	0.113	0.0038		1.73	↓	17.8	0.090
164	0.112	0.108	0.0036	0.0022	1.64		17.4	0.075
165	0.102	0.099	0.0033	0.0020	1.65	↓	15.6	0.075
166	0.102	0.099	0.0033	0.0020	1.65		15.5	0.075
167	0.102	0.099	0.0033	0.0020	1.65	1.00	15.6	0.065 (5)

- (1) Total oxidizer flow,  $\dot{w}_{O_2}$ -T, was measured
- (2) Bed and secondary oxidizer flows were calculated based upon cold flows and previous tests.
- (3) Fuel flow to the bed,  $\dot{w}_{H_2}$ -Bed, was measured.
- (4) Bed reactions were monitored and verified by thermocouples buried in the bed. The secondary reaction was monitored and verified by a photocell and by thermocouples.
- (5) The fast response was obtained with a fast restart of the hot bed.

### III, D, Catalytic Igniter (cont.)

After successfully achieving repeatable secondary reactions, the igniter and facility were prepared for cold tests, including replacement of the catalyst bed.

#### Test Series 6 - Low Temperature Catalyst Bed Evaluation

The purpose of these tests was to evaluate the effect of bed temperature on the igniter start transient. Eighteen tests were conducted in this series and the resulting data are presented in Table XII. These tests were conducted with the coolant hydrogen circuit "blanked" off and the oxygen flow proportional to the primary and secondary circuits. The plan was to test the igniter at ambient conditions first to provide baseline data at ambient conditions for comparison with the results to be obtained from a cold bed.

The first test resulted in a malfunction because the oxidizer valve did not open; however, the flow of hydrogen alone served to activate the bed because the next test was successful and the response was rapid, i.e., 135 msec to secondary reaction (Test 169). The next two tests resulted in bed reactions only; so for the next test (Test 172), the oxidizer flow rate was increased, resulting in secondary reaction. Three more tests were conducted at slightly reduced oxygen flow to ensure that the catalyst was operating properly. When the igniter appeared to be responding well (Test 175), the oxidizer flow rate was adjusted to the value desired for the cold tests and three tests were conducted for baseline data (Tests 176, 177 and 178).

The outside of the igniter was soaked in  $\text{LN}_2$  in preparation for the first cold test. The attempt resulted in a very low level bed reaction with no secondary reaction occurring within the 1.0-sec test duration. Another test was tried immediately, which resulted in another low level bed reaction only but accompanied with increased temperature activity within the bed. Note the pretest bed temperature had risen by  $31^\circ\text{K}$  ( $55^\circ\text{R}$ ) above that for the previous test. A third test (Test 181) resulted in a high level bed reaction accompanied by a

TABLE XII

## CATALYTIC IGNITER DATA - TEST SERIES 6

Test Number	$\dot{w}_{O_2}$ -T, lbm/sec(1)	$\dot{w}_{O_2}$ -Bed, lbm/sec(1)	$\dot{w}_{H_2}$ -Bed, lbm/sec(2)	MR, Bed	$P_c$ , psia	Duration, sec	Delay sec	$T_{Bed}$ , °R(3)	Propellant Conditions
168	0.102	0.0031	0.0019	1.63	Oxidizer valve did not open				
169	0.102	0.0031	0.0019	1.63	15.0	1.0	0.135	Amb	Amb
170	0.102	0.0031	0.0019	1.63	9.0	1.0	Bed Reaction Only		
171	0.102	0.0031	0.0019	1.63	9.0	1.0	Bed Reaction Only		
172	0.112	0.0036	0.0019	1.89	16.0	1.0	0.275	Amb	Amb
173	0.107	0.0034	0.0019	1.79	15.9	1.0	0.55	↑	↑
174	0.107	0.0034	0.0019	1.79	15.9	1.0	0.185		
175	0.107	0.0034	0.0019	1.79	15.9	1.0	0.165		
176	0.102	0.0031	0.0019	1.63	15.0	1.0	0.140		
177	0.102	0.0031	0.0019	1.63	15.2	1.0	0.230	↓	↓
178	0.102	0.0031	0.0019	1.63	15.1	1.0	0.220		
179	0.102	0.0031	0.0019	1.63	8.2(5)	1.0	-	Amb	Amb
180	↑	↑	↑	↑	8.2(6)	↑	-	310	Amb
181					14.9		-	365	↑
182					15.1		0.560	395	
183					15.0		0.540	390	
184(4)	↑	↑	↑	↑	15.4	↑	0.190	410	
185					1.63		0.410	426	↓
	0.102	0.0031	0.0019	1.63	15.0	1.0	0.210	443	Amb

(1) Total oxygen flowrate,  $\dot{w}_{O_2}$  -T, was measured, and the oxygen flow to the bed,  $\dot{w}_{O_2}$  -Bed, was calculated based upon previous calibrations.

(2) hydrogen flow to the bed,  $\dot{w}_{H_2}$  -Bed, was measured.

(3) Bed temperature measurements were obtained just prior to each test from thermocouples located in the catalyst bed.

(4) The fuel valve opened erratically causing slow igniter response.

(5) Bed reaction only, but hardly any temperature rise.

(6) Bed reaction only, detectable temperature rise.

### III, D, Catalytic Igniter (cont.)

secondary reaction which was delayed by 560 msec. The next tests were not conducted until the catalyst bed temperature had returned to the desired chilled condition. The long ignition delay of Test 184 (i.e., 410 msec), in comparison with the results from companion tests, was caused by an erratic fuel valve which did not open fully during the test. Because the data appeared to give the results desired, no further tests were conducted in this series.

Upon disassembly of the igniter, some damage to the catalyst bed was observed. The downstream portion of the bed, near the aft trap, contained slag and there was a hole through the bed, approximately 0.25-in.-dia, on the side closest to the inlet to the oxidizer manifold. There was also evidence of heating of the inner sleeve, but no damage.

The damage to the bed was caused by an oxygen maldistribution due to the reduced pressure drop which resulted when the injector face plate was removed. To improve distribution, a pressure drop plate was installed over the oxygen orifice inlets. A plate was also installed between the injection orifices and the catalyst bed to break up the oxidizer-rich streams from the modified injector.

The results of these tests indicate that bed activity is sensitive to temperature. The bed had been run several times before the cold tests were begun and appeared to be operating reproducibly. Also, enough test time had been accumulated to eliminate the possibility that contaminants in the bed had confused the results obtained with the chilled bed.

The results obtained at this point seemed to indicate that the condition of the catalyst bed may have caused a major portion of the low level bed reactions. All test series resulted in no secondary oxygen ignitions during the initial tests. To evaluate the effect of catalyst preconditioning, the repacked catalyst bed remained in a vacuum oven at 366°K (200°F) for approximately 30 hours and was returned to atmospheric pressure under a blanket of hydrogen gas before the next test series.

### III, D, Catalytic Igniter (cont.)

#### Test Series 7 - Low Temperature Propellant Evaluation

The initial tests of this series were conducted at ambient conditions to evaluate the effect of the pretest catalyst conditioning. The resulting data are presented in Table XIII. As the data show, bed response was slow during the first test, better during the second, and responded well during each following test. Some improvement in initial test catalyst response resulted from the special precautions.

These initial tests at ambient conditions were also accompanied by sporadic secondary reactions, even though the test conditions remain unchanged for blocks of tests and the bed response was adequate in each test to cause an ignition.

The next 11 tests (Tests 203 through 213) were conducted with chilled propellants and the igniter bed at ambient temperature. The tests were conducted at intervals of propellant chilling to evaluate the effect on igniter response of cold propellants entering the ambient temperature catalyst bed. Each test resulted in good bed response, i.e., bed temperature increasing to approximately 1255°K (1800°F) directly after entrance of the propellants into the bed. Four tests resulted in no secondary reactions, possibly due to the method of secondary oxygen injection with this design. The results of these tests indicate that good bed reaction can be achieved with incoming propellant temperatures below 167°K (300°R). The tests were terminated at this temperature level because the oxygen was approaching saturation conditions at the upstream venturi pressure.

The last tests were conducted with both the propellants and igniter chilled. The intent of these tests was to find a lower limit where bed reactions cease to be effective. The test technique used was to chill the hardware to the lowest level possible, stop chilling, and then attempting

TABLE XIII

DATA OBTAINED FROM TESTS WITH THE LOW  $P_c$  CATALYTIC IGNITER DURING  
TESTS WITH COLD PROPELLANTS, TEST SERIES 7

Test Number IG-20C-	General Test Conditions	$\dot{V}_{O_2}$ -T, $\dot{V}_{O_2}$ -sec, $\dot{V}_{O_2}$ -Bed, $\dot{V}_{H_2}$ -Bed, lbm/sec lbm/sec lbm/sec lbm/sec			MR, Bed Sec	$T_{ign}$ , °R	$T_{Tot}$ , °R	$T_{Pt}$ , °R	$P_c$ , psia	Dur., sec	Delay sec	Remarks
		(1)	(2)	(3)								
186	Prepurge Bed with $CH_4$	0.102	0.099	0.0031	0.0019	1.63	53.7	Amb	9.5	1.0	-	Low Level Bed Response
187	Repeat Test	0.102	0.099	0.0031	0.0019	1.63	53.7	↑	9.5	↑	-	Better Bed Response
188	Increase $\dot{V}_{O_2}$ and MR	0.114	0.110	0.0036	0.0021	1.71	54.4	↑	16.1	16.1	0.175	Good Bed Response
189	Repeat Test	↑	↑	↑	↑	1.73	↑	↑	16.0	16.0	0.210	Good Bed Response
190	Repeat Test	↑	↑	↑	↑	↑	↑	↑	16.1	16.1	0.165	Good Bed Response
191	Repeat Test	↑	↑	↑	↑	↑	↑	↑	-	-	-	Bed Response Same as Prev. Test
192	Repeat Test	↑	↑	↑	↑	↑	↑	↑	-	-	-	Bed Response Same as Prev. Test
193	20 msec Fuel Lead	↑	↑	↑	↑	↑	↑	↑	15.9	15.9	0.170	Good Bed Response (4)
194	Repeat Test	↑	↑	↑	0.0021	1.73	54.4	↑	-	-	-	Good Bed Response (4)
195	Reduce Fuel Flowrate	↑	↑	↑	0.0020	1.80	57.0	↑	-	-	-	Good Bed Response (4)
196	Repeat Test	↑	↑	↑	↑	↑	↑	↑	16.0	16.0	0.342	↑
197	Repeat Test	↑	↑	↑	↑	↑	↑	↑	-	-	-	↑
198	Use $CH_4$ Prepurge	↑	↑	↑	↑	↑	↑	↑	-	-	-	↑
199	Repeat Test	↑	↑	↑	↑	↑	↑	↑	16.1	16.1	0.128	↑
200	Prepurge and Wait 30 sec	↑	↑	↑	↑	↑	↑	↑	16.1	16.1	0.250	↑
201	Prepurge and Wait 1 min	↑	↑	↑	↑	↑	↑	↑	-	-	-	↑
202	Repeat Test	0.114	0.110	0.0036	0.0020	1.80	57.0	Amb	16.0	16.0	0.370	Good Bed Response (4)

(1) Total oxidizer flow,  $\dot{V}_{O_2}$  -T, was measured.

(2) Primary and Secondary oxidizer flowrates,  $\dot{V}_{O_2}$  -Bed and  $\dot{V}_{O_2}$  -sec, were calculated.

(3) Total Fuel Flow,  $\dot{V}_{H_2}$  -Bed, was measured.

(4) Bed temperature rise started immediately upon arrival of propellants at bed.

During these tests they reached approximately 1900°F within 0.500 sec whether-or-not there was a secondary reaction.

TABLE XIII (cont.)

Test Number IG-2C-	General Test Conditions	$\dot{V}_{O_2}$ -T, $\dot{V}_{O_2}$ -sec, $\dot{V}_{O_2}$ -Bed, $\dot{V}_{H_2}$ -Bed, $\dot{V}_{H_2}$ -Bed		MR, Bed	MR, Bed	$T_{Bed}$ , °R	$T_{OT}$ , °R	$T_{PT}$ , °R	$P_c$ , psia	Dur., sec	Delay, sec	Remarks		
		(1)	(2)	(3)	(4)									
<u>Tests with Propellants-Only Chilled</u>														
203	Initial Test, Cold Prop.	0.114	0.110	0.0036	0.0020	1.80	57.0	Amb	443	443	-	1.0	Good Bed Response (4)	
204	Repeat Test								429	429	-	-		
205									429	429	-	-		
206									425	425	16.0	0.405		
207									428	419	15.0	0.075		
208									400	388	16.0	0.185		
209									336	361	12.0	0.075		
210									340	343	17.0	0.065		
211									281	280	14.0	0.085		
212									282	278	-	-		
213	Repeat Test	0.114	0.110	0.0036	0.0020	1.80	57.0	Amb	288	283	12.5	1.0	Good Bed Response (4)	
<u>Tests with Propellants and Igniter Chilled</u>														
214	Initial Test, Cold System	0.114	0.110	0.0036	0.0020	1.80	57.0	290	288	285	13.0	1.0	Good Bed Response (4)	
215	Repeat Test								300	288	285	13.0	0.091	Good Bed Response (4)
216									350	288	284	7.0	-	Good Bed Response (4)
217									400	288	283	-	-	Slightly Delayed Response
218									288	284	-	-	-	Poor Bed Response
219									288	285	-	-	-	
220									288	285	-	-	-	
221									290	285	-	-	-	
222	Repeat Test	0.114	0.110	0.0036	0.0020	1.80	57.0	400	291	286	7.0	1.0	-	Poor Bed Response

### III, D, Catalytic Igniter (cont.)

ignition as the temperature increased. This approach was used to preclude the need for cooling to remove the heat from reactions expected at higher temperatures. Bed response and secondary oxygen reaction was achieved with the first two tests, at the coldest bed temperatures. Good bed response but no secondary oxygen reaction occurred with a bed temperature of 195°K (350°R) followed by poor bed response with increasing bed temperatures.



### III, Technical Discussion (cont.)

#### E. THRUST CHAMBER VALVES

##### 1. Selection

A review of commercial valves and ALRC-designed valves during the proposal phase resulted in selection of the Titan II first-stage 12.7 cm (5-in.) oxidizer butterfly valve for this application. Test experience was available for 7.6 cm (3 in.) and 10.2 cm (4 in.) line size valves of this type using  $H_2$  and  $O_2$  propellants. A 12.7-cm (5-in.) valve had been tested for 1500 cycles with an all-metal seal; a potential advantage for pulse mode testing should heat soak to the valves be significant. Air flow tests were conducted with the 12.7-cm (5-in.) valve to evaluate the gas flow characteristics. The results were converted to equivalent  $GH_2$  and  $GO_2$  flows as shown on Figure III-41. The calculated pressure drops were  $0.90 \text{ N/cm}^2$  (1.30 psi) at the  $GH_2$  rated flow of 0.52 Kg/sec (1.14 lb/sec) and  $0.38 \text{ N/cm}^2$  (0.55 psi) at the  $GO_2$  rated flow of 1.3 Kg/sec (2.86 lb/sec) at nominal inlet conditions of  $13.8 \text{ N/cm}^2$  (20 psia) and  $300^\circ\text{K}$  ( $540^\circ\text{R}$ ) temperatures.

##### 2. Design Description

The thrust chamber valve design consists of a Titan butterfly valve operated by a commercially available, double-acting actuation cylinder which drives the butterfly gate through a bell crank and link. Belleville spring sets were used to snub the valve motion near the end of travel. Facility pilot control valves were used to control the fluid to the actuator.

##### 3. Test Results

The thrust chamber valves were assembled, leak checked, functionally tested, and used for facility checkout and igniter testing on Contract NAS 3-14348 prior to Task XVIII engine tests. Response testing at

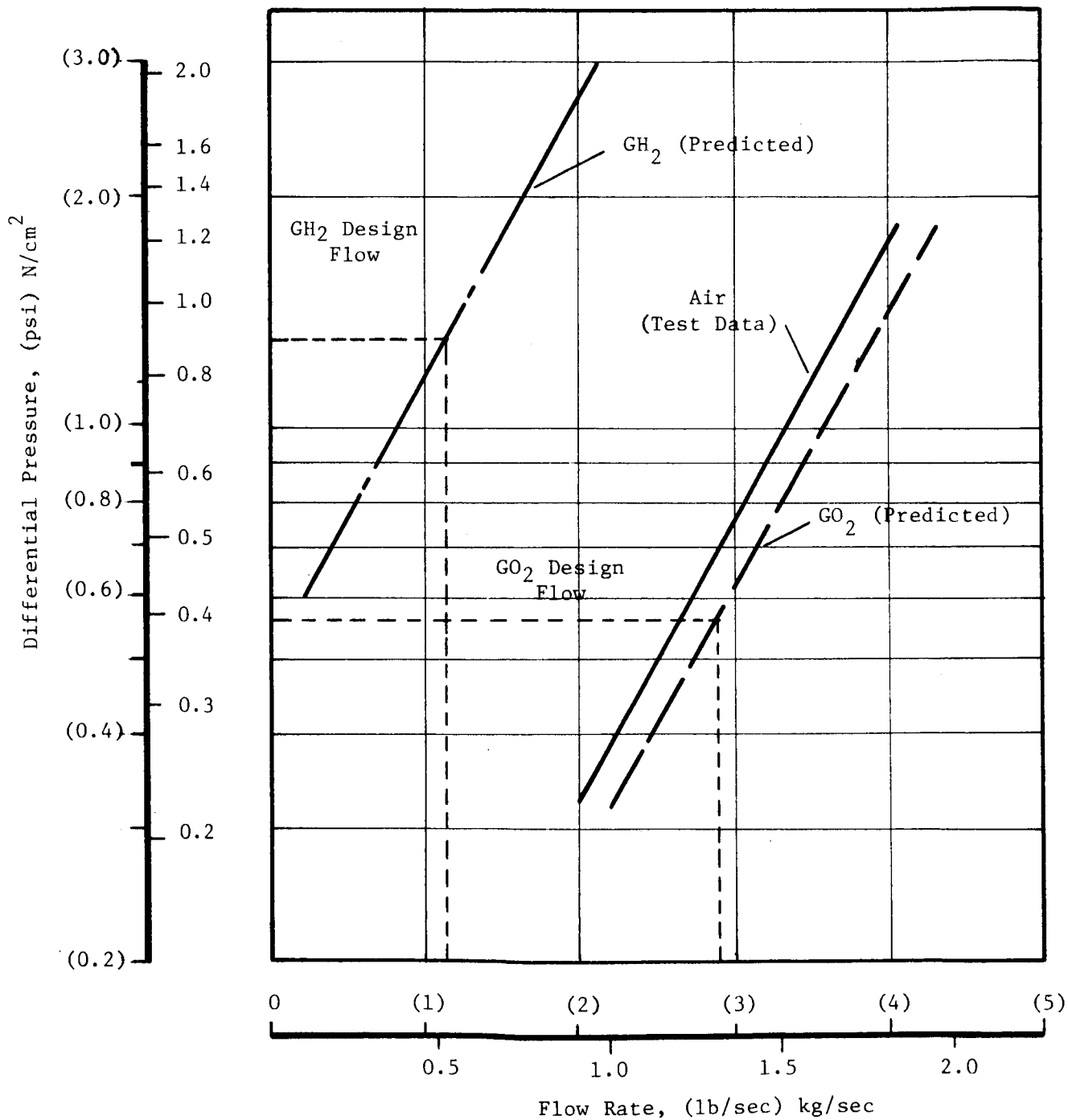


Figure III-41. Flow Characteristics of Titan Valve

### III, E, Thrust Chamber Valves (cont.)

the extremes of propellant temperatures was scheduled to be conducted just prior to hot or cold propellant testing.

Leak tests of the assembled valves were conducted using  $69 \text{ N/cm}^2$  (100 psig) gaseous nitrogen. No bubbles were observed over a 5-min period with either valve assembly. Qualitative leak tests of the valves, made after 16 engine tests (and numerous system flow tests) had been conducted, indicated no pressure decay in the inlet line segment after a 5-min hold period.

The response characteristics measured for the functional checkout tests are shown on Figures III-42 and III-43. Figure III-42 shows the travel times of the 12.7-cm (5-in.) butterfly valves from initial motion to full open position for opening and closing of each valve. Figure III-43 shows the time required to shuttle the pilot control valves, pressurize the actuator cavity, and initiate travel of the propellant valves on opening and closing.

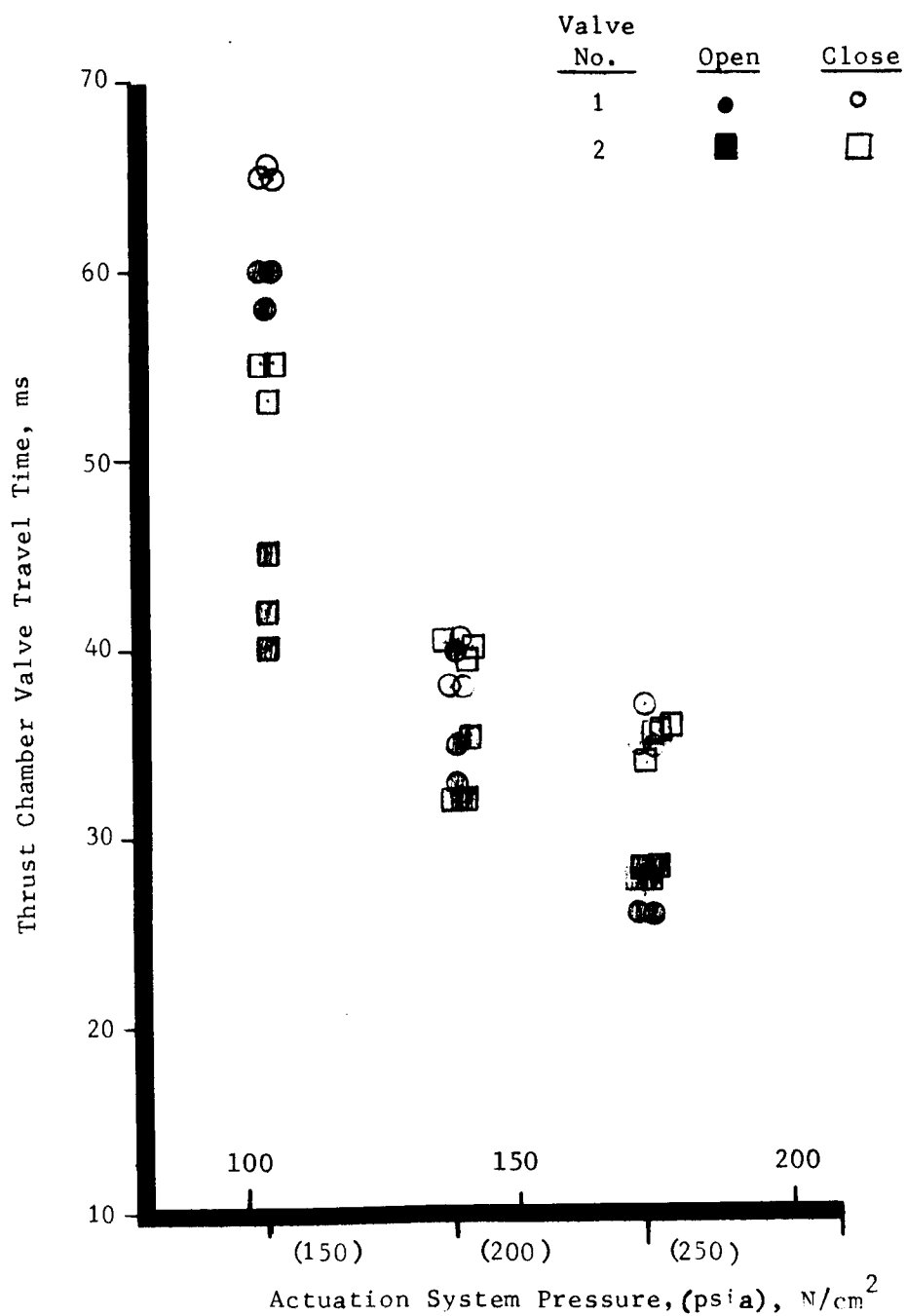


Figure III-42. Thrust Chamber Valve Travel Time

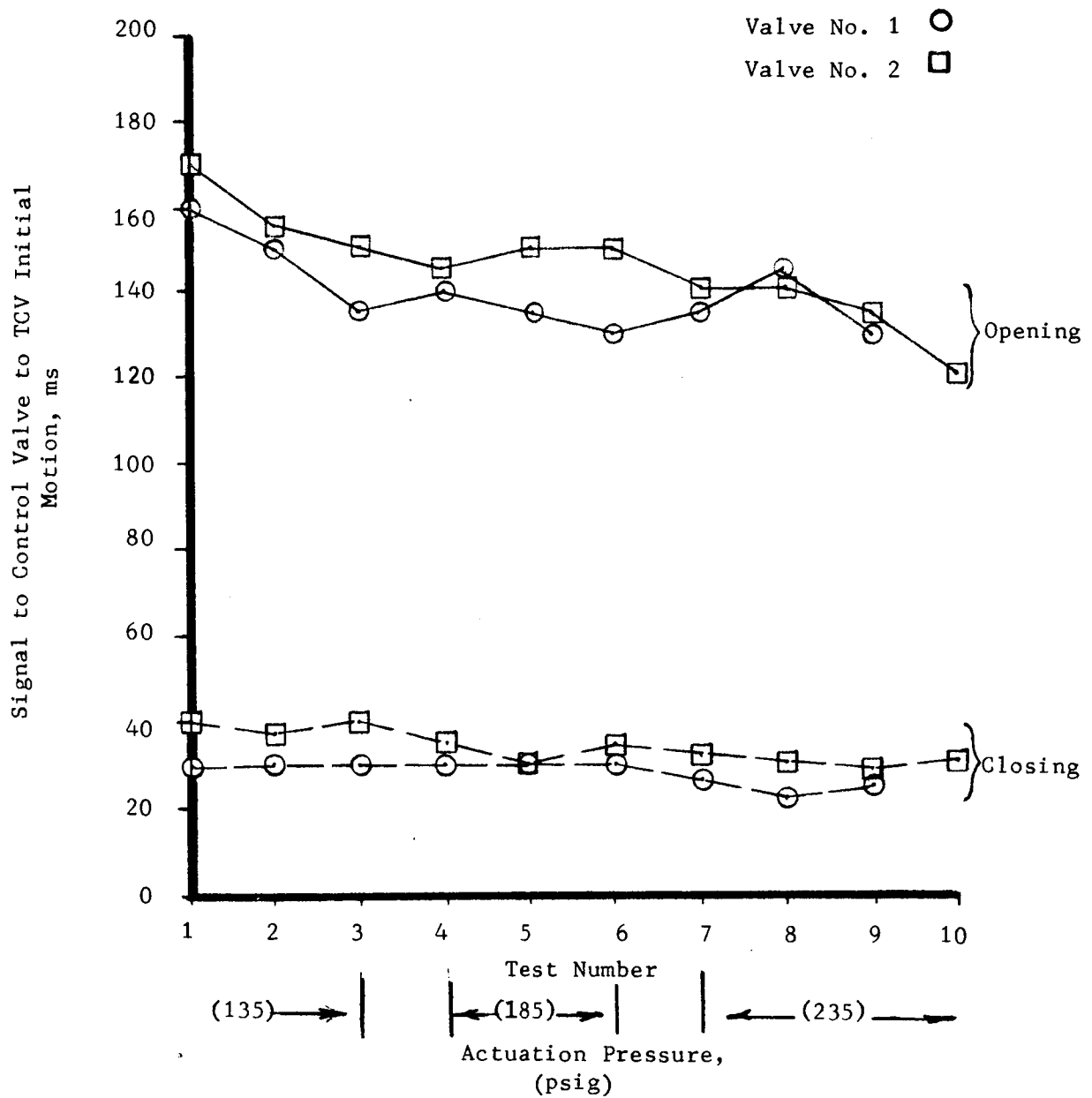


Figure III-43. Thrust Chamber Valve Control System Response  
Page 113

### III, Technical Discussion (cont.)

#### F. INJECTOR TESTING (TASK XVIII)

##### 1. Test Summary

The contract stop work order stopped all effort related to the vaned injector testing and reduced the scope of the coaxial injector testing to four test series for performance and thermal data. Thirty-four tests were conducted. Ten tests were to checkout igniter and engine hardware and to adjust the safety interlocks which were used to ensure engine operation to preclude introduction of excessive quantities of hydrogen into the closed altitude facility. The final 24 tests were valid thruster tests. The operating conditions and results of the engine tests are summarized in Table XIII.

The initial sequence of Tests 1680-D02-OA-001 through -022 were conducted in the J-3 altitude simulation facility using the J-3 steam ejector system. For the final test series (-023 through -034), the higher capacity J-4 steam ejector system was used to minimize cell pressure buildup, thereby increasing the allowable test duration. The longer test durations were required to improve the quality of the thermal data obtained during the tests.

All tests were conducted using the SN 001 coaxial element injector. Chamber  $L^*$ 's of 41 and 66 cm (16 and 26 in.) were evaluated. Three film coolant injection sleeves were tested to evaluate the effect of coolant injection location. A streak chamber was prepared and tested.

The accumulated firing duration of the 24 engine tests was 170 sec. Test conditions included chamber pressure excursions from 4.1 to 13.8 N/cm<sup>2</sup> (9 to 20 psia), mixture ratios from 2 to 4, and fuel coolant fractions to 30% of the total fuel. All tests were conducted using ambient temperature propellants.

### III, F, Injector Testing (Task XVIII) (cont.)

The first series of tests was conducted for a nominal duration of 5 sec using a 66-cm (26 in.) L\* chamber and a 20% film coolant ring (designed for a coolant-to-gas velocity ratio of 1) that was 7.05 cm (2.78 in.) long. The matrix for these tests was planned to evaluate coolant quantity (30, 20, and 10%) at a fixed engine O/F of 2.5, followed by an evaluation of engine O/F (4 to 2) with the nominal 20% coolant flow.

For the second series of tests, the film coolant sleeve was removed and uncooled tests were conducted at three O/F ratios (2.0, 2.5 and 4.0) at the nominal  $10.4 \text{ N/cm}^2$  (15 psia) chamber pressure, followed by two tests at the chamber pressure extremes ( $6.9$  and  $13.8 \text{ N/cm}^2$ , 10 and 20 psia) at a nominal 2.5 O/F ratio.

For the third series, the ablative lined chamber was installed and a 5-sec streak test was conducted without film cooling.

The fourth test series was conducted using the 7.05 cm (2.78 in.) long, 10% nominal design flow coolant ring. Nominal coolant flows of 20, 10 and 5% of the fuel were selected for these tests. The injector flow balance was adjusted for each test to provide a nominal overall engine O/F ratio of 2.5. These tests were conducted for a duration of 10 sec to improve the quality of the thermal data.

The sixth series of tests continued the use of the 66 cm (26 in.) L\* chamber but with a short, film coolant sleeve designed for optimum injection velocity at 20% coolant flow. This short coolant sleeve introduced the hydrogen coolant 1.27 cm (0.5 in.) from the injector face plane. As with the preceding coolant tests, the overall engine O/F ratio was held at 2.5 during coolant flows of 10, 20, and 30% of the total fuel flow.

### III, F, Injector Testing (Task XVIII). (cont.)

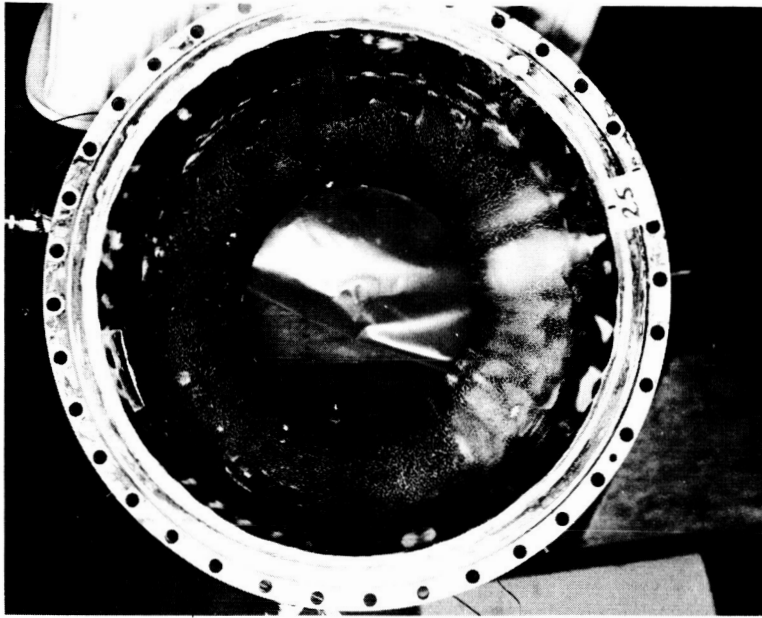
The seventh and final series of tests evaluated the effect of  $L^*$  and coolant injection station on performance and coolant effectiveness. The chamber  $L^*$  was reduced to 41 cm (16 in.) and the 7.05 cm (2.78 in.) long nominal 10% coolant sleeve was installed. The configuration then injected the coolant at the point where the chamber begins to converge toward the throat. As with the earlier tests using this coolant sleeve configuration, 20, 10, and 5% of the fuel was flowed through the annulus formed by the sleeve while the overall engine O/F was maintained at a nominal value of 2.5. This concluded the revised injector test series.

#### 2. Streak Chamber Test

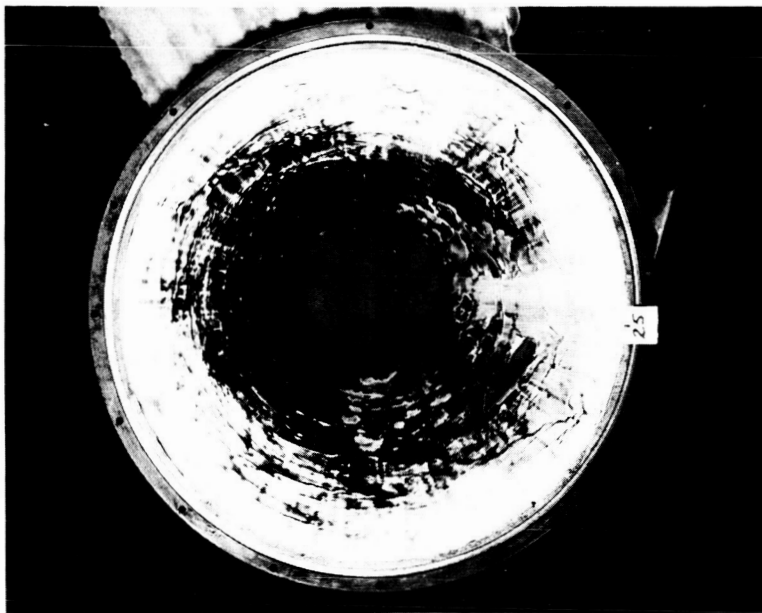
As part of the test series, a streak chamber was fired to evaluate the chemical and thermal compatibility of the injector. This test (-022) was run with the silicon rubber ablative lined chamber described in Section III,B,3. The test was run at a  $P_c$  of  $10.8 \text{ N/cm}^2$  (15.7 psia) with an overall mixture ratio of 3.2. The higher than nominal mixture ratio was intended to simulate the mixture ratio at which the injector would run if the engine were operating at an  $MR = 2.5$  with approximately 20% of the fuel being used as film coolant. In addition, the use of the higher mixture ratio would accentuate any compatibility problems which might exist with the unit.

The postfire condition of the ablative material is shown in Figure III-44. This figure shows the chamber as viewed from both the injector and the nozzle exit. With the exception of the light streak (virgin material) at the location marked "25", the chamber discoloration is very uniform, reflecting a high degree of uniformity in the combustion products. The color (not apparent in the photo) was that characteristic of a fuel-rich gas. The light streak, which is apparent in both the combustion chamber and the exit cone, occurred at the lowest spot in the thruster. Apparently, what happened was that moisture from the steam-driven altitude facility condensed inside the thrust





Combustion Chamber



Nozzle Exit

Figure III-44. Streak Chamber - Postfire Condition

### III, F, Injector Testing (Task XVIII) (cont.)

chamber and injector prior to the firing. The resulting small puddle of water acted as film coolant, protecting the ablative liner material. In the combustion chamber, the ablative material in line with the cold streak was virgin and only a small amount of degradation was apparent in the skirt. It is also interesting to note that the heat flux near the nozzle exit was so low that no degradation of the silicon rubber occurred during the 5-sec firing.

#### 3. Performance Evaluation

All Low  $P_c$  APS altitude tests were evaluated using a slightly modified version of the ICRPG simplified performance evaluation procedure. This technique allows identification of the real engine performance losses which can be associated with the propellant combination, impurity level, operating point, reaction kinetics, propellant maldistribution, thruster geometry, and boundary effects. The remaining losses, due to incomplete injector energy release and the utilization of fuel film cooling, are then determined by deduction. The latter two operations form the primary deviations from the referenced procedure. With the JANNAF technique, the cooling loss is computed as a mixture ratio distribution loss without thermal exchange. The energy release loss is then computed by reducing the heat of formation of the incoming propellants until the predicted performance, which includes all the component losses, matches the actual test data. For the low  $P_c$  test data analysis, the energy release efficiency was determined by subtracting out the known losses from the uncooled MR survey test series and establishing an energy release loss (ERL) versus mixture ratio for the injector/chamber combination. When cooling was introduced, the ERL loss was identified from this history and the remaining performance loss was charged to cooling (FCL).

### III, F, Injector Testing (Task XVIII) (cont.)

#### a. Impurity Loss (IL)

Propellant impurity losses resulted due to the use of MIL Spec propellants which contain 0.5% impurity by weight. Including this specie when computing the one-dimensional equilibrium and kinetic performance allows determination of an impurity performance loss.

#### b. Kinetics Loss (KL)

Kinetic losses were computed using the JANNAF approved one-dimensional kinetics computer model, ODK, for each of the operating points conducted. When film cooling was employed, the additional kinetics loss due to core mixture ratio shift was included as part of the coolant loss.

#### c. Mixture Ratio Maldistribution Loss (MRDL)

Mixture ratio maldistribution losses resulted due to the employment of an ignition torch which operated at a lower mixture ratio than the core. A mass weighted stream tube analysis identified the magnitude of this loss.

#### d. Boundary Layer Loss (BLL)

Boundary layer losses were evaluated taking into account test operating point values together with the measured heat flux as experimentally determined by the chamber wall temperature response. This loss therefore includes boundary layer heat transfer and wall skin friction and was computed using the JANNAF turbulent boundary layer computer model.

### III, F, Injector Testing (Task XVIII) (cont.)

#### e. Curvature-Divergence Loss (DL)

Nozzle divergence losses for the 15-degree conical chamber were computed from JANNAF nozzle charts for each test operating point.

#### f. Energy Release Loss (ERL)

The injector energy release loss was deduced by removing the aforementioned known losses from the difference between theoretical and measured specific impulse. This evaluation was performed for Tests -017 through -023, thus enabling the injector off-design (ERL) performance characteristics to be identified.

#### g. Film Cooling Loss (FCL)

Film coolant losses were then deduced on the film-cooled tests by subtracting an injector energy release loss corresponding to the core mixture ratio in conjunction with the remaining computed losses. This loss results due to a combination of three factors: off-design injector kinetics (KL), unequal stream tube specific impulse (MRD), and heat removal from the injector core. The latter factor includes the specific impulse reduction which occurs in the core gases as the film coolant is heated along the chamber and nozzle walls. Comparison of this resulting loss is made with Thermal Exchange Film Coolant Performance Model which analytically considers these three factors.

### 4. Performance Test Results

All testing on the Low  $P_c$  APS was accomplished in the J-3 altitude facility at ambient pressures corresponding to altitudes of 60,000 to 165,000 feet. A summary of the resulting performance data is included in Table XIV. Performance measurements were made in terms of characteristic exhaust

## ENGINE TEST DATA AND PERFORMANCE SUMMARY

**NOTES:**

Test No.	Sleeve Length (in.)	Sleeve Design Coolant Flow (% of Total Fuel)
1	1.0	100
2	1.0	100
3	1.0	100
4	1.0	100
5	1.0	100
6	1.0	100
7	1.0	100
8	1.0	100
9	1.0	100
10	1.0	100
11	1.0	100
12	1.0	100
13	1.0	100
14	1.0	100
15	1.0	100
16	1.0	100
17	1.0	100
18	1.0	100
19	1.0	100
20	1.0	100
21	1.0	100
22	1.0	100
23	1.0	100
24	1.0	100
25	1.0	100
26	1.0	100
27	1.0	100
28	1.0	100
29	1.0	100
30	1.0	100
31	1.0	100
32	1.0	100
33	1.0	100
34	1.0	100
35	1.0	100
36	1.0	100
37	1.0	100
38	1.0	100
39	1.0	100
40	1.0	100
41	1.0	100
42	1.0	100
43	1.0	100
44	1.0	100
45	1.0	100
46	1.0	100
47	1.0	100
48	1.0	100
49	1.0	100
50	1.0	100
51	1.0	100
52	1.0	100
53	1.0	100
54	1.0	100
55	1.0	100
56	1.0	100
57	1.0	100
58	1.0	100
59	1.0	100
60	1.0	100
61	1.0	100
62	1.0	100
63	1.0	100
64	1.0	100
65	1.0	100
66	1.0	100
67	1.0	100
68	1.0	100
69	1.0	100
70	1.0	100
71	1.0	100
72	1.0	100
73	1.0	100
74	1.0	100
75	1.0	100
76	1.0	100
77	1.0	100
78	1.0	100
79	1.0	100
80	1.0	100
81	1.0	100
82	1.0	100
83	1.0	100
84	1.0	100
85	1.0	100
86	1.0	100
87	1.0	100
88	1.0	100
89	1.0	100
90	1.0	100
91	1.0	100
92	1.0	100
93	1.0	100
94	1.0	100
95	1.0	100
96	1.0	100
97	1.0	100
98	1.0	100
99	1.0	100
100	1.0	100

2. The following chambers were employed:

Test No.	Chamber Length, in.	Chamber Characteristic Length, in.
1	1.0	1.0
2	1.0	1.0
3	1.0	1.0
4	1.0	1.0
5	1.0	1.0
6	1.0	1.0
7	1.0	1.0
8	1.0	1.0
9	1.0	1.0
10	1.0	1.0
11	1.0	1.0
12	1.0	1.0
13	1.0	1.0
14	1.0	1.0
15	1.0	1.0
16	1.0	1.0
17	1.0	1.0
18	1.0	1.0
19	1.0	1.0
20	1.0	1.0
21	1.0	1.0
22	1.0	1.0
23	1.0	1.0
24	1.0	1.0
25	1.0	1.0
26	1.0	1.0
27	1.0	1.0
28	1.0	1.0
29	1.0	1.0
30	1.0	1.0
31	1.0	1.0
32	1.0	1.0
33	1.0	1.0
34	1.0	1.0
35	1.0	1.0
36	1.0	1.0
37	1.0	1.0
38	1.0	1.0
39	1.0	1.0
40	1.0	1.0
41	1.0	1.0
42	1.0	1.0
43	1.0	1.0
44	1.0	1.0
45	1.0	1.0
46	1.0	1.0
47	1.0	1.0
48	1.0	1.0
49	1.0	1.0
50	1.0	1.0
51	1.0	1.0
52	1.0	1.0
53	1.0	1.0
54	1.0	1.0
55	1.0	1.0
56	1.0	1.0
57	1.0	1.0
58	1.0	1.0
59	1.0	1.0
60	1.0	1.0
61	1.0	1.0
62	1.0	1.0
63	1.0	1.0
64	1.0	1.0
65	1.0	1.0
66	1.0	1.0
67	1.0	1.0
68	1.0	1.0
69	1.0	1.0
70	1.0	1.0
71	1.0	1.0
72	1.0	1.0
73	1.0	1.0
74	1.0	1.0
75	1.0	1.0
76	1.0	1.0
77	1.0	1.0
78	1.0	1.0
79	1.0	1.0
80	1.0	1.0
81	1.0	1.0
82	1.0	1.0
83	1.0	1.0
84	1.0	1.0
85	1.0	1.0
86	1.0	1.0
87	1.0	1.0
88	1.0	1.0
89	1.0	1.0
90	1.0	1.0
91	1.0	1.0
92	1.0	1.0
93	1.0	1.0
94	1.0	1.0
95	1.0	1.0
96	1.0	1.0
97	1.0	1.0
98	1.0	1.0
99	1.0	1.0
100	1.0	1.0

### III, F, Injector Testing (Task XVIII) (cont.)

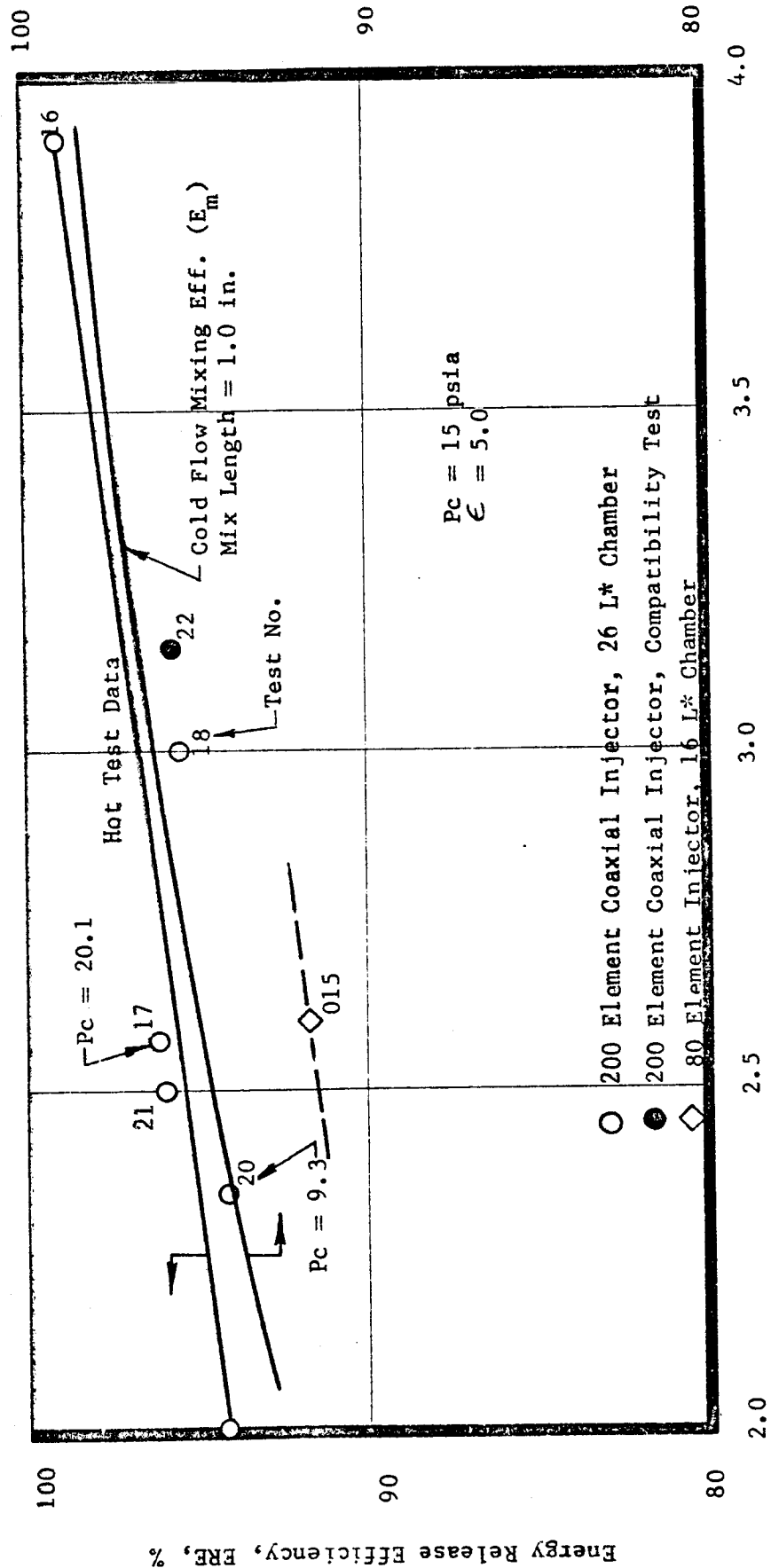
velocity and vacuum specific impulse. Flow rate measurements were made using critical flow nozzles, calibrated at Colorado Engineering Institute against accepted standards. Flow determination was then accomplished using upstream chromel-alumel (C-A) thermocouple data and absolute pressure measurements, in conjunction with Johnson real gas coefficients and the critical nozzle thermodynamic flow area. Thrust measurements were taken using precalibrated twin bridge load cells, the values from which were averaged to increase measurement accuracy. Thruster temperature and pressure measurements were obtained using C-A thermocouples and strain gage absolute pressure transducers. The combined performance instrumentation accuracy is 0.664%, 2 sigma, on vacuum specific impulse. Altitude measurements were made with a Beratron altitude pressure transducer which delivers extremely accurate measurements from 0.034 to 1.03 N/cm<sup>2</sup> (0.05 to 1.5 psia).

#### a. Injector Performance

Performance losses directly attributable to the injector design and chamber configuration were evaluated on ten tests as a function of the operating point. With these tests, the performance variability with respect to mixture ratio, chamber pressure, element quantity, and chamber length were defined. In some instances, these correlations were made on limited data samples since contract redirection was initiated prior to the desired repeat testing.

Injector performance was evaluated by computing the performance penalty solely dependent on incomplete injector energy release. The results of this analysis are portrayed in Figure III-45 in terms of energy release efficiency. This performance parameter is defined as the delivered performance efficiency in the absence of other performance losses and is computed by:

Test Series 1680-D02-0A-XXX



Mixture Ratio, O/F, Overall

Figure III-45. Injector Energy Release Performance

### III, F, Injector Testing (Task XVIII) (cont.)

$$\text{ERE} = \frac{I_{\text{sp}}(v_T) - \text{ERL}}{I_{\text{sp}}(v_T)} \times 100$$

where:

ERE	= energy release efficiency, %
$I_{sp}(v_T)$	= theoretical one-dimensional vacuum specific impulse, sec, at the overall mixture ratio
ERL	= energy release loss, sec

Seven of the altitude tests (Nos. -017 through -023) were conducted at various chamber pressures and mixture ratios without film cooling to define the performance characteristics of the 200-element coaxial injector. An uncooled steel chamber of 30.5 cm (12 in.) length and 66 cm (26 in.) L\* was employed. The last test was conducted with a "painted" material on the chamber and nozzle walls to identify the chemical compatibility of the injector core gases with the nozzle walls and hydrogen fuel film coolant.

The data trend indicated increasing performance with increasing mixture ratio, similar to the data from cold flow studies conducted at a one-inch mixing length (see Figure III-5). The noted performance improvement with mixture ratio was interpreted to be due to an increased swirl component of the oxygen at higher mass flows, thus reducing the potential core mixture ratio and providing a higher momentum exchange with the hydrogen. This characteristic is apparent by comparing the cold flow mass and mixture ratio profiles shown in Figure III-6. The cold flow mixing efficiency data cannot be directly compared to energy release since the former only identifies the deviation in mixture ratio while the latter denotes hot fire performance deviation from theoretical. The trends with mixture ratio are important, however, denoting the mixing characteristics of the element design. Comparable efficiency levels for cold flow at 2.54 cm (1.0 in.) and hot test at 30.5 cm (12 in.) can be partially explained by noting the inhibiting influence of propellant interface combustion which isolates oxygen and hydrogen rich zones. In addition, with



### III, F, Injector Testing (Task XVIII) (cont.)

combustion, the products proceed down the chamber at high velocities with respect to cold flow, reducing the stay time within the chamber. The factor of 12 on length is therefore a gross comparator and may vary with element design and operating point, which is induced by reaction chemistry influences.

Three other performance characteristics were interpreted based on a limited data sample. These characteristics are portrayed with respect to the independent variables of chamber pressure, chamber length, and element quantity as shown in Figure III-46. Chamber pressure influences were demonstrated on Tests -017, -020, and -021 at 2.5 mixture ratio and a 30.5 cm (12 in.) chamber length. At  $6.9 \text{ N/cm}^2$  (10 psia), a performance reduction of 1.5% was noted while at  $13.8 \text{ N/cm}^2$  (20 psia), only a minor improvement was noted. This characteristic is interpreted to be due to reduced oxidizer swirl momentum at the lower chamber pressure exhibiting an effect similar to low mixture ratio shift at constant chamber pressure. Lower reaction rates may also induce an influence, the magnitude of which is uncertain.

Chamber length influence was evaluated on two tests (Tests -024 and -032) where the chamber length was changed from 20 to 30.5 cm (8 to 12 in.) with identical mixture ratios, film coolant ring and coolant fractions. No uncooled tests with length changes were conducted. The noted length influence for the 200-element injector is approximately one second per inch of chamber length. It must be stated, however, that the shorter length chamber may induce a different cooling loss per percent coolant, since the angled convergent portion of the chamber is 10.2 cm (4 in.) closer to the injector face, which may introduce more chemical interactions between the core and the coolant. If this were the case, the computed cooling loss would be less, which would have the effect of increasing the inferred energy release loss over the one second per inch value previously quoted. Therefore, this value is considered a minimum.

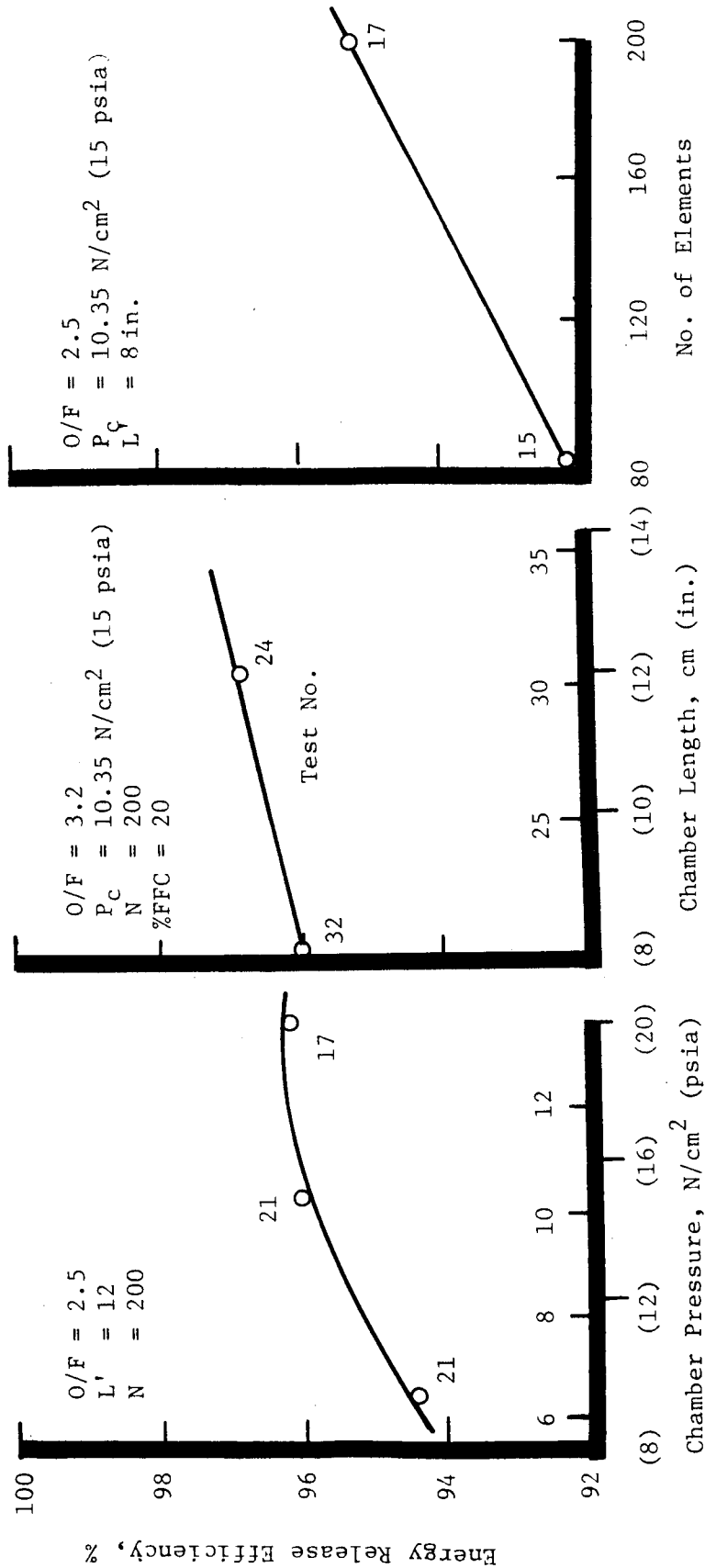


Figure III-46. Influence of Design Parameters of Injector Performance

### III, F, Injector Testing (Task XVIII) (cont.)

The influence of element quantity is portrayed on the third graph of Figure III-46. Here, an 80-element injector designed during a company-sponsored program is compared to the 200-element optimized coaxial element. A 3% improvement is noted with the finer pattern together with the removal of the oxidizer potential core with the swirler.

#### b. Cooling Performance

The last 11 altitude tests were performed using hydrogen film cooling injected from three coolant ring geometries. Three series of cooling tests were conducted. The first series evaluated the influence of overall mixture ratio at a constant coolant fraction of 20% of the total hydrogen flow. The corresponding coolant loss was then deduced by subtracting the calculated performance losses and the empirically determined energy release loss at the core mixture ratio from the difference between measured and theoretical specific impulse using the following expression:

$$FCL = (I_{sp}(V_T) - I_{sp}(v_T)) - (IL + KL + MRDL + DL + BLL) - ERL_c$$

where: FCL = fuel film cooling loss, sec

$I_{sp}(V_T)$  = theoretical one-dimensional vacuum specific impulse at the overall mixture ratio, sec

$I_{sp}(v_T)$  = measured vacuum specific impulse, sec

IL = propellant impurity loss, sec

KL = kinetics loss, sec

MRDL = mixture ratio maldistribution loss, sec

DL = nozzle divergence loss, sec

BLL = boundary layer loss, sec

$ERL_c$  = mass weighted energy release loss (sec) evaluated at the core mixture ratio (Figure III-46)

### III, F, Injector Testing (Task XVIII) (cont.)

The results of these loss determinations are portrayed in Figure III-47 as percent of theoretical. All tests utilized a 66-cm (26-in.)  $L^*$  chamber and either the 10 or 20%, 7.1 cm (2.78 in.) length coolant ring. The percentage refers to the coolant fraction for which the ring was designed while the length refers to the injection distance from the injector face. For the purposes of comparison, this figure also shows the performance loss predicted on the basis of the Thermal Exchange Coolant Performance Model. This model assumes heat is extracted from the injector core uniformly and is added to the coolant. This creates a reduced enthalpy core product stream and a high temperature hydrogen coolant stream, which are assumed not to mix. Mass weighting the stream tube specific impulse values and comparing to a uniform mixture theoretical specific impulse identifies the coolant loss magnitude.

Departures from the thermal exchange model are believed a result of two factors. At high mixture ratios ( $MR = 4$ ), the possibility of local oxidizer-rich core zones increases the potential of chemical reaction with the coolant, thereby reducing the apparent coolant loss. At the fuel-rich condition ( $MR = 2$  and lower), the core flame temperature is greatly reduced, producing a lower coolant specific impulse stream tube and therefore a greater performance loss. This loss mechanism approaches a no-energy-exchange stream tube condition.

The second coolant series evaluated the coolant loss associated with changes in the coolant fraction from 10 to 30% and is shown in Figure III-48. The Thermal Exchange Coolant Performance Model prediction is also portrayed for comparison. Three coolant ring geometries were evaluated during these tests: the two previously mentioned and a 1.27-cm (0.5-in.) long 20% ring. In general, the performance loss followed the prediction model with the exception of Test -029. This test, with the 1.27-cm (0.5-in.) length ring, required the coolant to travel 29.2 cm (11.5 in.) along the chamber wall without mixing in order to be comparable with the assumptions of the cooling model.

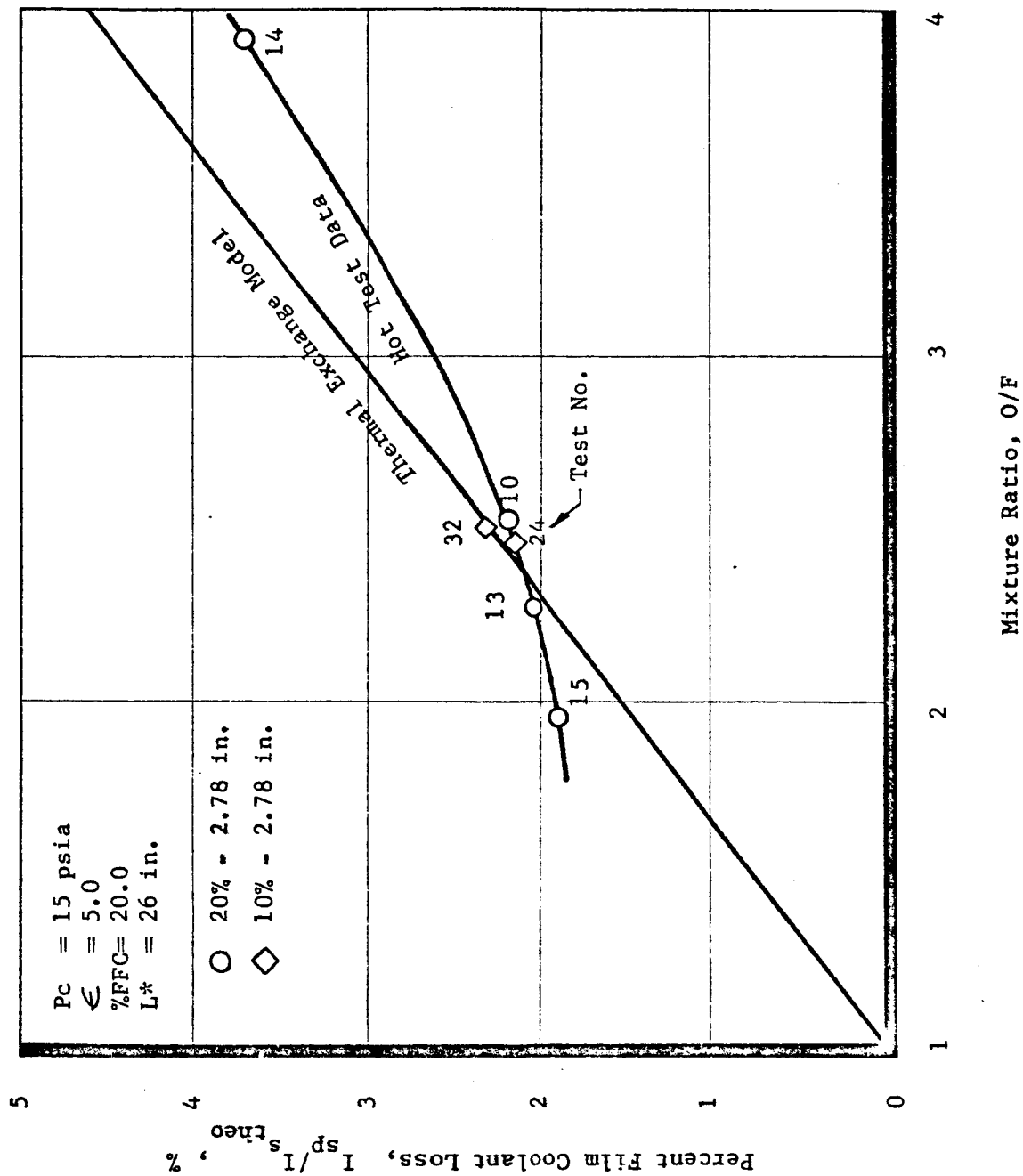


Figure III-47. Film Cooling Performance Loss vs Mixture Ratio

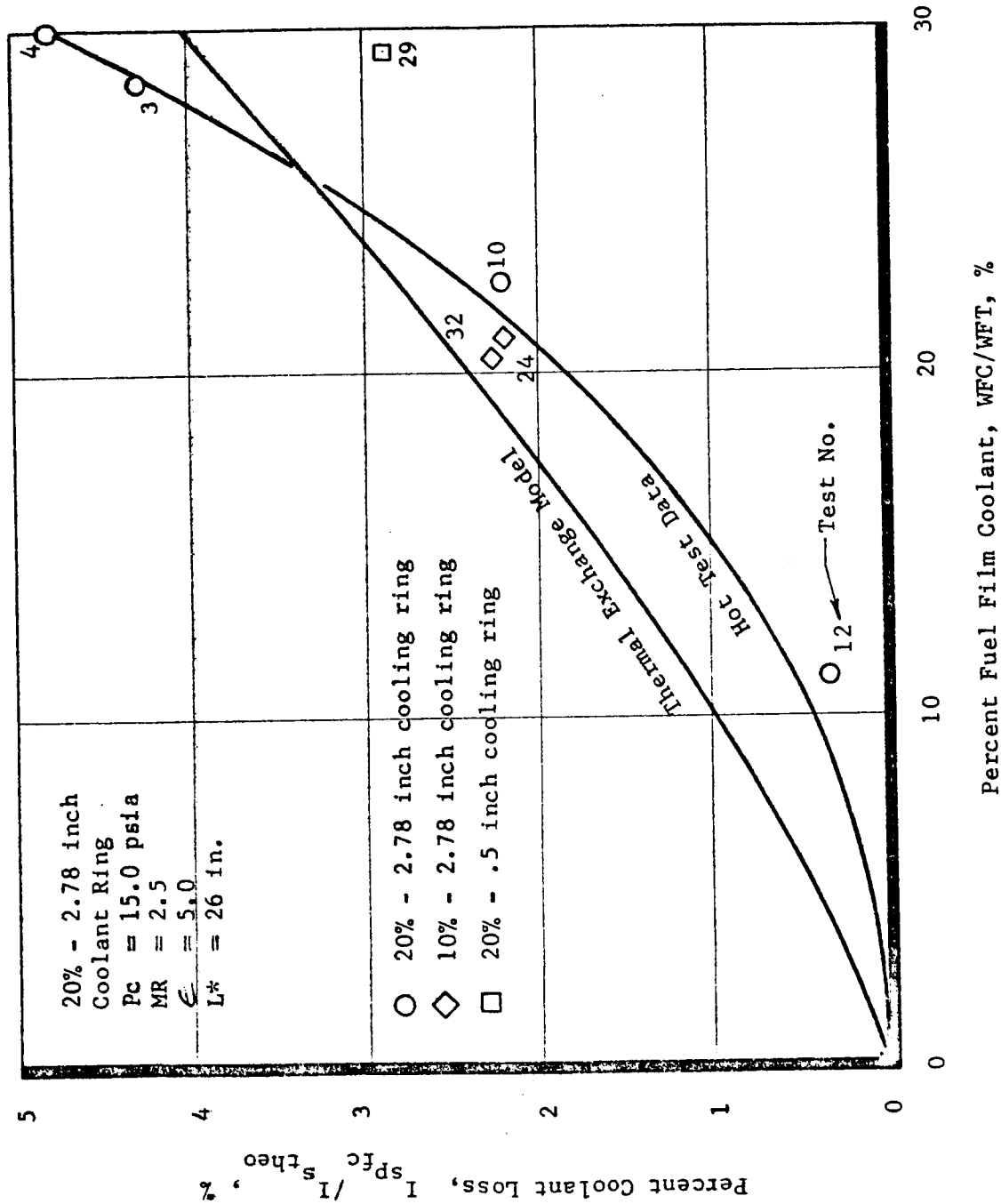


Figure III-48. Film Cooling Performance Loss vs Percent Film Cooling

### III, F, Injector Testing (Task XVIII) (cont.)

The lower than theoretical loss again identifies a core interaction as the coolant mixes with the core products. Tests -003 and -004, on the other hand, which used a 7.1-cm (2.78-in.) length film coolant ring directing the coolant away from the high recirculation zone near the injector face, gave rise to a more predictable coolant loss. Very little coolant performance loss difference was noticed between the 10 and 20% coolant injection rings at 20% coolant flow rate (Tests -010, -032 and -024). The remaining tests at other coolant fractions evidenced nozzle separation, therefore invalidating the measured performance data.

#### c. Performance Demonstration

Analysis of the thermal data from the altitude test series indicated a hydrogen coolant fraction of 10% would be necessary to meet the cycle life durability requirements of the contract. At this condition, contract performance demonstration was obtained on Test 1680-D02-OA-012. The measured specific impulse corresponding to this thermal design point was 386.0 sec, exceeding the contract goal by 11 sec. A comparison of these data with the contract goal is given in Table XV.

#### d. Measured Altitude Performance

All tests were performed with slightly different wall temperature profiles producing varying degrees of boundary layer performance loss. In order to assess the true difference in performance at various levels of coolant fraction, the curves of Figure III-49 were constructed. In this portrayal, a range of measured performance data is plotted using the 20% - 7.1 cm (2.78 in.) coolant ring for tests from 0 to 30% coolant. Correcting this data to a common adiabatic wall boundary layer loss results in the upper curve of the figure. Nominalizing these data to a common boundary layer loss clearly indicates the performance potential of the Low  $P_c$  APS cooled hardware with respect to the contract goal of 375 sec. At the thermal design point, a performance of 389 sec appears obtainable, exceeding the contract goal by greater than 3%.

TABLE XV  
PERFORMANCE SUMMARY  
Test 1680-D02-OA-012\*

	<u>Demonstrated</u>	<u>Goal</u>
Thrust, Newtons (lbf)	7000 (1539)	6820 (1500)
Mixture ratio, O/F	2.48	2.5
Chamber pressure, N/cm <sup>2</sup> (psia)	10.49 (15.2)	10.35 (15.0)
Area ratio	5.0	5.0
Fuel film cooling, %	11.2	**
One-dimensional specific impulse, sec	421.2	421.5
Argon contaminant loss, sec	1.0	1.0
Kinetics loss, sec	4.0	4.1
Nozzle divergence loss, sec	5.8	5.1
Boundary layer loss, sec	7.4	4.0
Mixture ratio maldistribution, sec***	1.0	0.0
Film cooling loss, sec	1.3	**
Energy release loss, sec	14.7	14.8
Delivered specific impulse, sec	386.0	375.0
Percent theoretical specific impulse, %	91.6	89.0
Characteristic exhaust velocity, m/s (ft/sec)	2460 (8056)	2430 (7980)
Percent characteristic exhaust velocity	95.9	95.0

\*A 5.07-sec test with a 2.9-sec data summary.

\*\*As required to meet durability requirements.

\*\*\*Due to igniter torch.



Test Series 1680-D02-OA-XXX

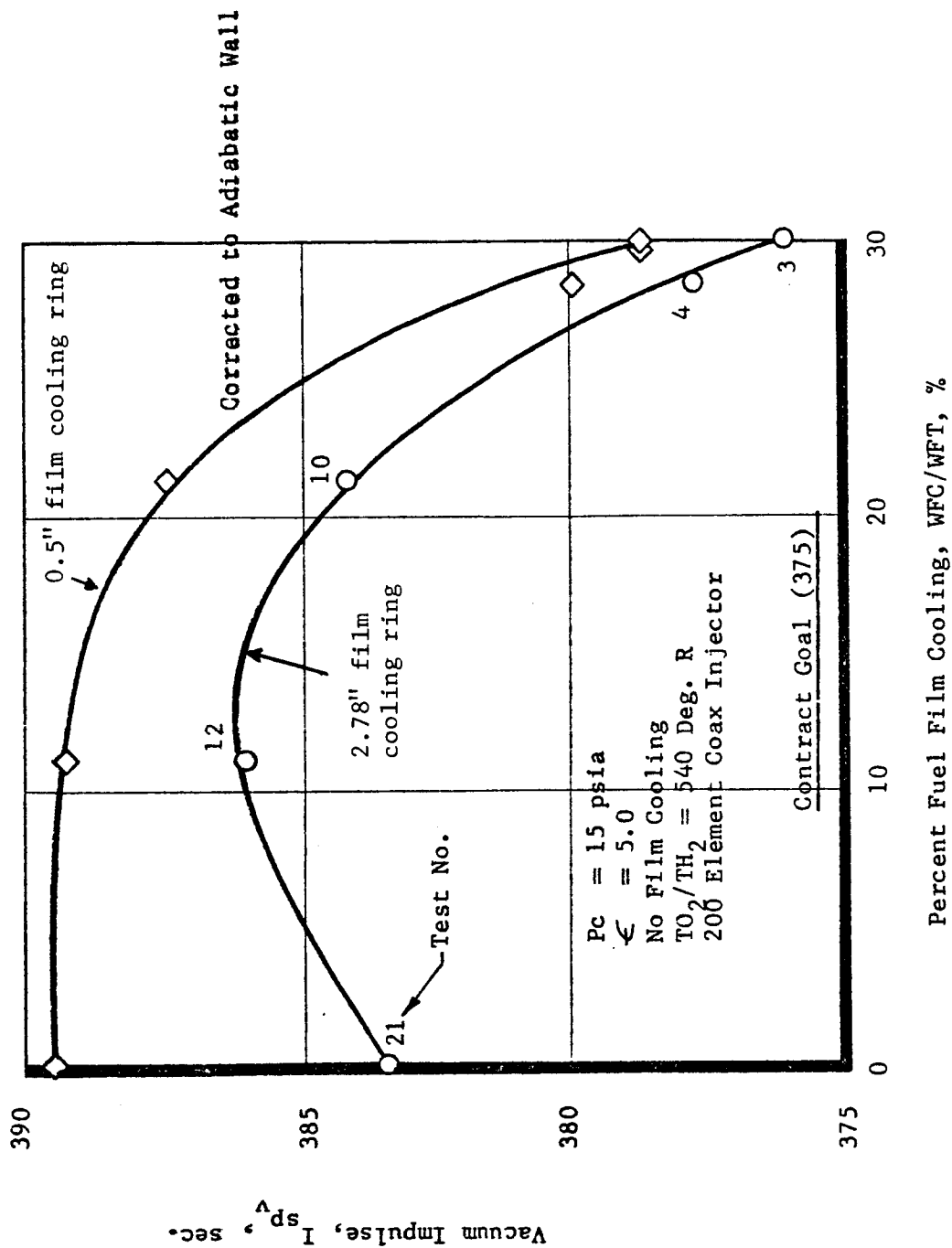


Figure III-49. Corrected Altitude Performance

### III, Technical Discussion (cont.)

#### G. HEAT SINK CHAMBER TESTING

Heat transfer measurements were made on the heat sink chamber as part of the reduced scope test program. The chamber thermal instrumentation consisted of both the gas-side wall thermocouples and the barrier probes described previously in Section III,B,2,b. Data were recorded on all tests. Because of the reduced budget for this effort, a rigorous evaluation of all the data was not performed. Instead, the data were reduced and analyzed only to the point at which the basic thermal characteristics of the thruster could be identified.

The primary source of information for the thermal analysis was the surface temperature measurements made with the flush-mounted chromel-alumel thermocouples. The raw data consisted of simply a surface temperature history of the uncooled wall at six different axial stations in the chamber. These measured temperatures were then used to drive a two-dimensional finite element model of the wall. The driven finite element model, in turn, would supply the heat flux to the wall as a function of wall temperature. This particular method of obtaining heat flux is especially well suited to the low pressure chamber as the relative thinness of the wall reduces axial conduction effects and the low heat flux (in conjunction with the thin wall) makes even a very coarse finite element network quite accurate.

The heat flux versus temperature information obtained in the above manner serves two purposes. First, the heat flux data is important in itself because it constitutes the basic information required in the design of any actively cooled (nonadiabatic) chamber. Even more importantly, however, the recovery temperature or adiabatic wall temperature can be deduced quite readily from a plot of heat flux versus wall surface temperature; this is illustrated in Figure III-50. The recovery temperature is obtained by extrapolating the line drawn through the data point out to its intercept with the abscissa.

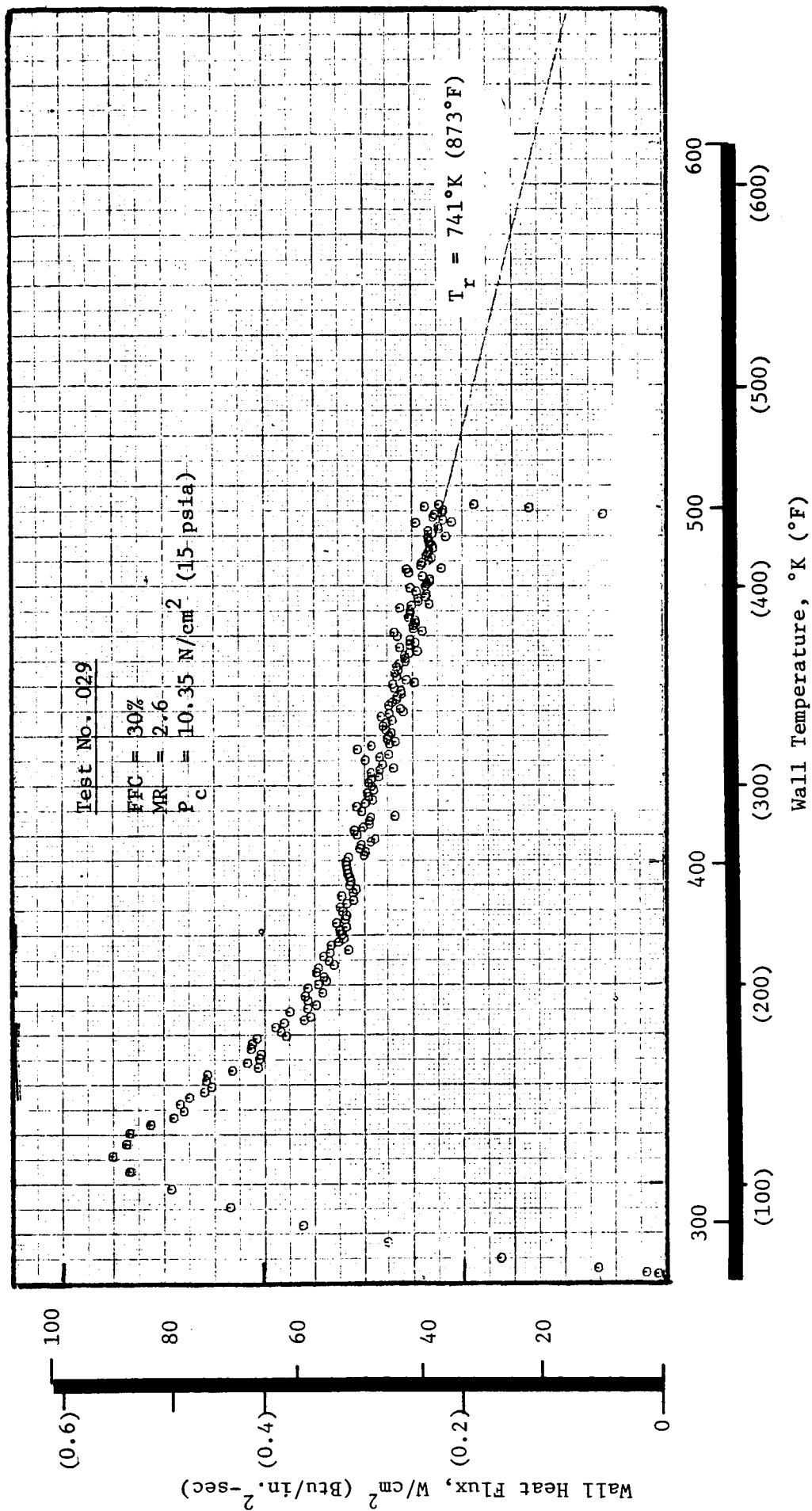


Figure III-50. Wall Heat Flux vs Wall Temperature

### III, G. Heat Sink Chamber Testing (cont.)

The temperature at the intercept (which is the zero heat flux point) is the recovery temperature. The absolute value of the slope of the temperature - heat flux line is the film coefficient. This technique for determining the recovery temperature is reasonably accurate for low recovery temperatures where the slope of the flux - heat transfer line is quite steep. However, when the recovery temperature is high, the slope of the line, and hence the recovery temperature, is difficult to determine accurately with data over a limited temperature range.

The experimental heat flux as a function of axial location and quantity of film cooling is shown in Figure III-51. These data were obtained at a chamber pressure of  $10.3 \text{ N/cm}^2$  (15 psia) and overall nominal mixture ratio of 2.5. Three curves are shown covering 0, 11, and 21% film cooling. The absolute flux levels are low, the peak heat flux being  $123 \text{ watts/cm}^2$  ( $0.75 \text{ Btu/in.}^2\text{-sec}$ ). The curve with no film cooling has a relatively high flux level in the chamber which decreases with increasing length, even in the throat region. This heat flux profile is unusual as, normally in rocket engines, the heat flux rises going into the throat region with the peak flux occurring just upstream of the throat. In addition, the measured throat heat flux is only about 40% of that which would be predicted using a turbulent boundary layer analysis such as that of Bartz. The explanation for this unusual behavior is that the boundary layer has relaminarized going into the throat, causing a significant reduction in the throat film coefficient. The very favorable pressure gradient, which exists due to the sharp convergence angle and the low level of turbulence (throat Reynolds number =  $1.5 \times 10^5$  based on diameter), allows the boundary layer to relaminarize. When the calculated radiant heat flux of  $6.5 \text{ watts/cm}^2$  is subtracted from the measured throat heat flux of  $77 \text{ watts/cm}^2$  ( $0.47 \text{ Btu/in.}^2\text{-sec}$ ), the resulting convective heat flux is what would be predicted based on a laminar boundary layer analysis. This is consistent with results obtained on the high pressure portion of the contract, in which relaminarization was also encountered. (A more detailed discussion of relaminarization can be found in the High Pressure Volume of this Final Report, NASA CR-120895).

Nominal  $P_c = 15$   
 Nominal MR = 2.5  
 Cooling Sleeve Length = 2.7"

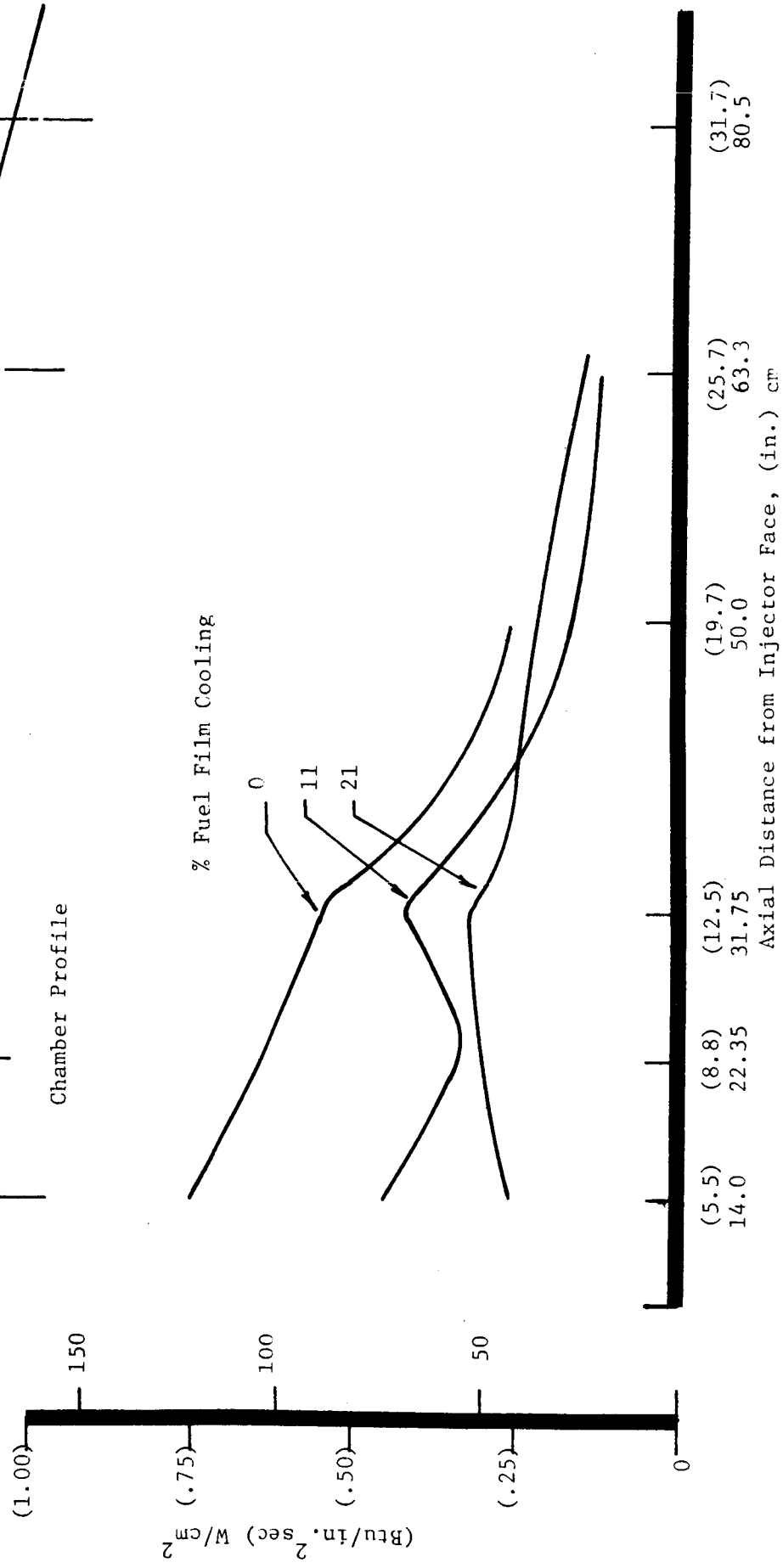


Figure III-51. Experimental Heat Flux to a 533°K (500°F) Wall

### III, G, Heat Sink Chamber Testing (cont.)

The addition of film cooling produces a general reduction in the chamber and throat heat flux levels as well as altering the axial flux distribution. The lower heat fluxes result from the lower recovery temperatures which the film coolant produces. The change in axial flux distribution arises from the fact that the recovery temperature is rising when approaching the throat rather than dropping off slightly as is the case without film cooling. With 21% film cooling, the heat flux actually rises going into the throat rather than dropping off. This does not mean that the relaminarization phenomenon is no longer occurring; instead it reflects the fact that, as the recovery temperature becomes lower, the heat flux becomes increasingly sensitive to variations in the recovery temperature. With 21% film cooling, the recovery temperature is so low that an increase of a few hundred degrees in the recovery temperature can double the driving  $\Delta T$  between the gas and the wall and largely overshadow what is happening to the film coefficient.

The effects which variations in film cooling flow and chamber pressure have on the throat heat flux with a 533°K (500°F) wall are given in the curves of Figure III-52. Although some data scatter does exist, it can be seen that the heat flux varies almost linearly with film coolant flow. The effect of chamber pressure on throat heat flux is best described with a  $P_c^{0.69}$  relationship. This  $P_c^{0.69}$  dependence lies between the  $P_c^{0.50}$  dependence expected with laminar flow and the  $P_c^{0.80}$  dependence of turbulent flow. It appears the most likely explanation for this behavior is that, as the chamber pressure is increased, the initial conditions for the relaminarization process change. Higher chamber pressures produce a higher level of initial turbulence, which delays the onset of relaminarization. In addition, the throat Reynolds number is very close to that at which only partial relaminarization will occur. In this case, the throat may be beginning to operate in a transitional regime and showed a mixed characteristic.

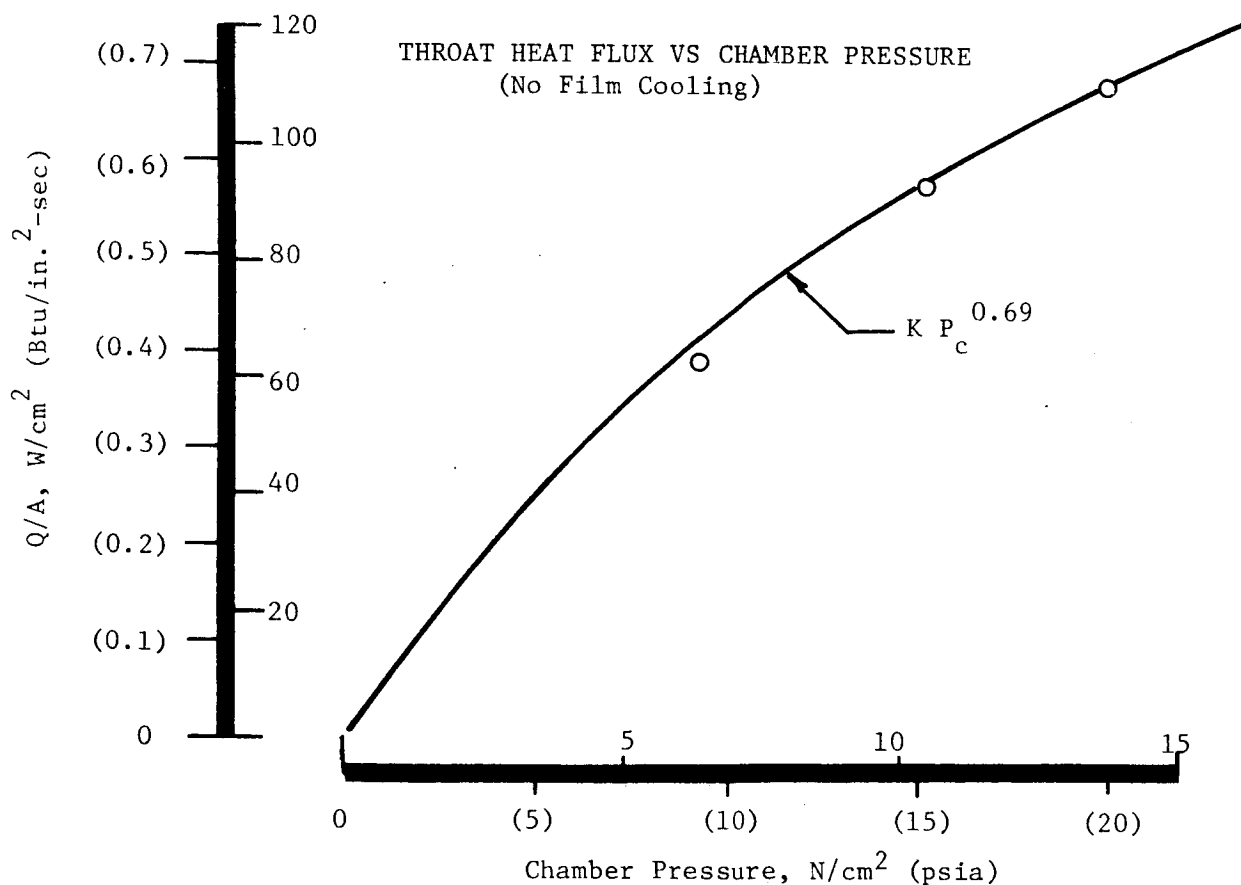
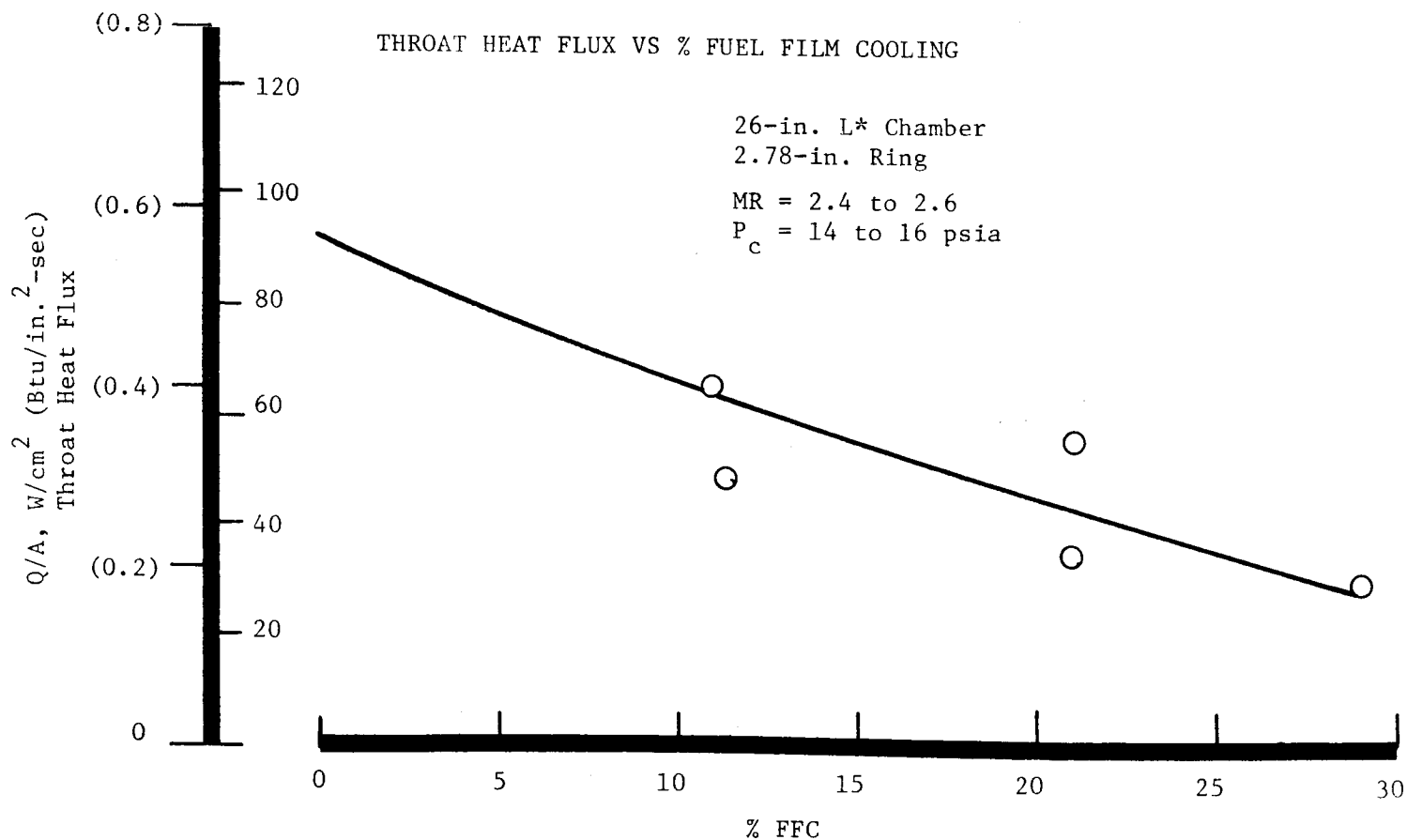


Figure III-52. Throat Heat Flux vs Percent Film Cooling and Chamber Pressure  
Page 139

### III, G, Heat Sink Chamber Testing (cont.)

Although the above heat flux data are of interest, the heat transfer data with the most practical significance for an operating thruster are given in Figure III-53. This figure shows the recovery temperature profiles which were obtained with four different sets of operating conditions. These temperatures are the temperatures at which the thrust chamber wall would operate if it were adiabatic. Since for the low pressure system the most attractive chamber design is simply a thin-walled adiabatic steel shell, the recovery temperatures shown are the actual operating temperatures for such a design. The data curves are for the nominal thruster operating conditions of a  $10.3 \text{ N/cm}^2$  (15 psia) chamber pressure and a mixture ratio of 2.5.

The effect of quantity of film cooling on recovery temperature can be seen by comparing the two sets of data obtained with the 31.8 cm (12.5 in.) long chamber and the 6.85 cm (2.7 in.) long film cooling sleeve. These data were obtained with 11 and 21% of the fuel being used as film coolant. There are two observations which should be made regarding these curves. First, the absolute temperature levels are very low, the peak recorded temperature with 11% film cooling being only about  $1090^\circ\text{K}$  ( $1500^\circ\text{F}$ ) and with 21% film cooling approximately  $865^\circ\text{K}$  ( $1100^\circ\text{F}$ ). This indicates an inexpensive stainless steel thruster could operate very satisfactorily with only 11% film cooling and have a considerable margin of safety. As noted previously in the discussion of the performance results, the thruster exceeds its performance goal with 11% film cooling; so in all respects, this would constitute a satisfactory design point. The second observation is that increasing the coolant percentage from 11 to 21% produces only a  $220^\circ\text{K}$  ( $400^\circ\text{F}$ ) reduction in wall temperature. The reason for this small decrease is that the absolute recovery temperature is so low with the 11% cooling flow that significant further decreases are difficult to accomplish. The recovery temperature approaches the coolant inlet temperature asymptotically as the coolant flow is increased. By going to 21% cooling, the thruster has well reached the point of diminishing returns.



$P_c = (15 \text{ psia}) \ 10.35 \text{ N/cm}^2$   
 $MR = 2.5$

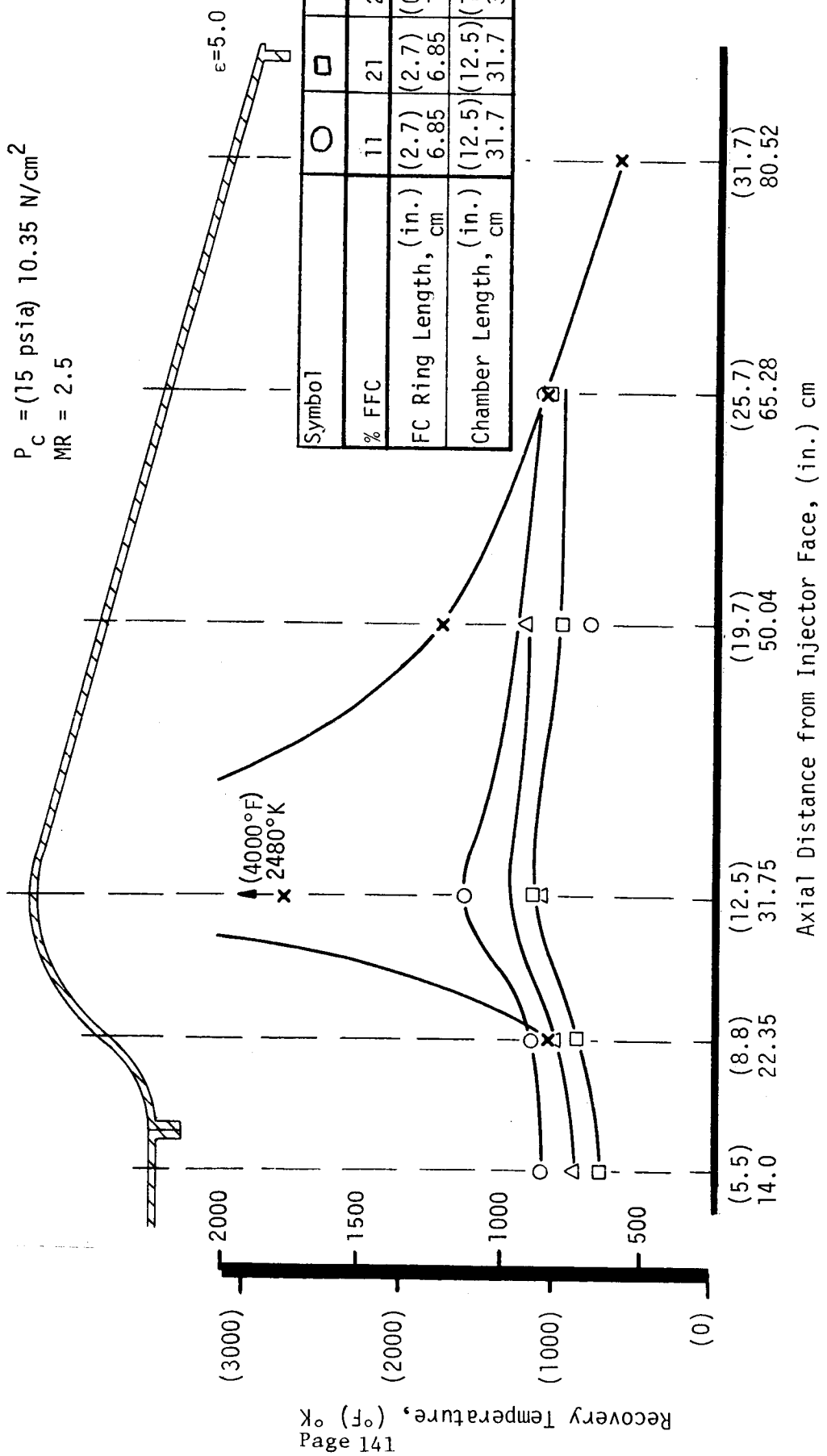


Figure III-53. Recovery Temperature with Film Cooling

### III, G, Heat Sink Chamber Testing (cont.)

The effect which film cooling sleeve length has upon film cooling effectiveness can be seen by comparing the two sets of data with 21% film cooling. The one set of data was obtained with a 1.27 cm (0.5 in.) long film cooling sleeve, while the other employed a 6.85 cm (2.7 in.) sleeve. The effect of the shorter sleeve is to raise the recovery temperatures a consistent 83 to 111°K (150 to 200°F) above the values obtained with the longer sleeve. This increased temperature with the shorter sleeve reflects the additional mixing which occurs between the core gas and coolant with the shorter sleeve. Although the increase in recovery temperature is seemingly small, it does amount to almost half the difference between 11 and 21% cooling. When viewed this way, it becomes apparent that the use of the longer sleeve probably reduces the film cooling requirements by 25 to 30%, and this should be regarded as significant.

The final comparison which can be made from the data of Figure III-53 is relative to the influence of chamber length on recovery temperature. The two sets of data with 11% film cooling were run with a 31.7 cm (12.5 in.) and a 21.6 cm (8.5 in.) long chamber. Both chambers employed the 6.85 cm (2.7 in.) long film cooling sleeve. The differences in recovery temperature profiles between these two conditions are very great, the longer chamber having a 1090°K (1500°F) throat recovery temperature while the corresponding value for the shorter chamber is approximately 2480°K (4000°F). The reason the shorter chamber is so much hotter is undoubtedly attributable to the injector and not the film cooling effectiveness. Apparently, the shorter chamber is not of sufficient length to allow the oxygen streams from the injector to completely mix and burn. As a result, the oxygen streams are impinging on the converging portion of the nozzle and mixing with and burning off the film coolant, producing recovery temperatures approaching the combustion temperature. These data make it obvious that the 200-element coaxial injector should not be run with a 21.6 cm (8.5 in.) long chamber.

APPENDIX A

DISTRIBUTION LIST

Report  
Copies  
R    D

Recipient

Designee

	National Aeronautics & Space Administration	
	Lewis Research Center	
	21000 Brookpark Road	
	Cleveland, Ohio 44135	
1	Atten: Contracting Officer, MS 500-313	
5	E. A. Bourke, MS 500-205	
1	Technical Report Control Office, MS 505	
1	Technology Utilization Office, MS 3-16	
2	AFSC Liaison Office, 501-3	
2	Library	
1	Office of Reliability & Quality Assurance, MS 500-111	
3	J. W. Gregory	Chief, Propulsion Systems Branch
		MS 500-203
1	P. N. Herr	MS 500-203
		MS 500-203
1	W. A. Tomazic	MS 500-203
1	L. H. Gordon	MS 500-203
1.	Director, Shuttle Technology Office, RS	
	Office of Aeronautics & Space Technology	
	NASA Headquarters	
	Washington, D.C. 20546	
2	Director Space Prop. and Power, RP	
	Office of Aeronautics & Space Technology	
	NASA Headquarters	
	Washington, D.C. 20546	
1	Director, Launch Vehicles & Propulsion, SV	
	Office of Space Science	
	NASA Headquarters	
	Washington, D.C. 20546	
1	Director, Materials & Structures Div., RW	
	Office of Aeronautics & Space Technology	
	NASA Headquarters	
	Washington, D.C. 20546	

Report  
Copies  
R    D

Recipient

Designee

1		Director, Advanced Manned Missions, MT Office of Manned Space Flight NASA Headquarters Washington, D.C. 20546	
37		National Technical Information Service Springfield, Virginia 22151	
1	1 1	National Aeronautics & Space Administration Ames Research Center Moffett Field, California 94035 Attn: Library	Hans M. Mark Mission Analysis Division
1		National Aeronautics & Space Administration Flight Research Center P.O. Box 273 Edwards, California 93523	
1		Director, Technology Utilization Division Office of Technology Utilization NASA Headquarters Washington, D.C. 25046	
1		Office of the Director of Defense Research & Engineering Washington, D.C. 20301 Attn: Office of Asst. Dir. (Chem Technology)	
2		NASA Scientific and Technical Information Facility P.O. Box 33 College Park, Maryland 20740 Attn: NASA Representative	
1	1	National Aeronautics & Space Administration Goddard Space Flight Center Greenbelt, Maryland 20771 Attn: Library	Merland L. Moseson, Code 620
1	1	National Aeronautics & Space Administration John F. Kennedy Space Center Cocoa Beach, Florida 32931 Attn: Library	Dr. Kurt H. Debus

Report Copies		<u>Recipient</u>	<u>Designee</u>
R	D		
1	1	National Aeronautics & Space Administration Langley Research Center Langley Station Hampton, Virginia 23365 Attn: Library	E. Cortwright Director
1	1	National Aeronautics & Space Administration Manned Spacecraft Center Houston, Texas 77001 Attn: Library	J.G. Thiobodaux, Jr. Chief, Propulsion & Power Division C.A. Vaughan
1	1	National Aeronautics & Space Administration George C. Marshall Space Flight Center Huntsville, Alabama 35912 Attn: Library	Hans G. Paul Keith Coates
1	1	Jet Propulsion Laboratory 4800 Oak Grove Drive Pasadena, California 91103 Attn: Library	Henry Burlage, Jr. Duane Dipprey
1		Defense Documentation Center Cameron Station Building 5 5010 Duke Street Alexandria, Virginia 22314 Attn: TISIA	
1		Arnold Engineering Development Center Air Force Systems Command Tullahoma, Tennessee 37389 Attn: Library	Dr. H.K. Doetsch
1		Aeronautical Systems Division Air Force Systems Command Wright-Patterson Air Force Base Dayton, Ohio Attn: Library	D.L. Schmidt Code ARSCNC-2
1		Air Force Missile Test Center Patrick Air Force Base, Florida Attn: Library	L.J. Ullian

Report  
Copies  
R    D

Recipient

Designee

1		Air Force Systems Command Andrews Air Force Base Washington, D.C. 20332 Attn: Library	Capt. S.W. Bowen SCLT
1	1 1	Air Force Rocket Propulsion Laboratory (LKDS) Edwards, California 93523 Attn: Library	R.L. Wiswell W. Lawrence
1		Air Force Rocket Propulsion Laboratory (RPM) Edwards, California 93523 Attn: Library	
1		Air Force FTC (FTAT-2) Edwards Air Force Base, California 93523 Attn: Library	Donald Ross
1		Air Force Office of Scientific Research Washington, D.C. 20333 Attn: Library	SREP, Dr. J.F. Mass
1		Space & Missile Systems Organization Air Force Unit Post Office Los Angeles, California 90045 Attn: Technical Data Center	
1		Office of Research Analyses (OAR) Holloman Air Force Base, New Mexico 88330 Attn: Library RRRD	
1		U. S. Air Force Washington, D.C. Attn: Library	Col. C.K. Stambaugh, Code AFRST
1		Commanding Officer U. S. Army Research Office (Durham) Box CM, Duke Station Durham, North Carolina 27706 Attn: Library	
1		U. S. Army Missile Command Redstone Scientific Information Center Redstone Arsenal, Alabama 35808 Attn: Document Section	Dr. W. Wharton

Report Copies		Recipient	Designee
R	D		
1		Bureau of Naval Weapons Department of the Navy Washington, D.C. Attn: Library	J. Kay, Code RTMS-41
1		Commander U. S. Naval Missile Center Point Mugu, California 93041 Attn: Technical Library	
1		Commander U. S. Naval Weapons Center China Lake, California 93557 Attn: Library	
1		Commanding Officer Naval Research Branch Office 1030 E. Green Street Pasadena, California 91101 Attn: Library	
1		Director (Code 6180) U. S. Naval Research Laboratory Washington, D.C. 20390 Attn: Library	H.W. Carhart J.M. Krafft
1	1	Picatinny Arsenal Dover, New Jersey 07801 Attn: Library	I. Forsten
1		Air Force Aero Propulsion Laboratory Research & Technology Division Air Force Systems Command United States Air Force Wright-Patterson AFB, Ohio 45433 Attn: APRP (Library)	R. Quigley C.M. Donaldson
1		Space Division Aerojet-General Corporation 9200 East Flair Drive El Monte, California 91734 Attn: Library	S. Machlawski
1		Aeronutronic Division of Philco Ford Corp. Ford Road Newport Beach, California 92663 Attn: Technical Information Department	Dr. L.H. Linder

Report  
Copies  
R   D

Recipient

Designee

1		Aerospace Corporation 2400 E. El Segundo Blvd. Los Angeles, California 90045 Attn: Library-Documents	J.G. Wilder
1		Astropower Laboratory McDonnell-Douglas Aircraft Company 2121 Paularino Newport Beach, California 92163 Attn: Library	
1		ARO, Incorporated Arnold Engineering Development Center Arnold AF Station, Tennessee 37389 Attn: Library	
1		Susquehanna Corporation Atlantic Research Division Shirley Highway & Edsall Road Alexandria, Virginia 22314 Attn: Library	
1		Beech Aircraft Corporation Boulder Facility Box 631 Boulder, Colorado Attn: Library	Douglas Pope
1	1	Bell Aerosystems, Inc.	T. Reinhardt
	1	Box 1	W. M. Smith
	1	Buffalo, New York 14240 Attn: Library	J. Flanagan
1		Instruments & Life Support Division Bendix Corporation P.O. Box 4508 Davenport, Iowa 52808 Attention: Library	W. M. Carlson
1		Boeing Company Space Division P.O. Box 868 Seattle, Washington 98124 Attn: Library	J.D. Alexander C.F. Tiffany



Report  
Copies  
R   D

Recipient

Designee

1	Boeing Company P.O. Box 1680 Huntsville, Alabama 35801	Ted Snow
1	Chemical Propulsion Information Agency Applied Physics Laboratory 8621 Georgia Avenue Silver Spring, Maryland 20910	Tom Reedy
1	Chrysler Corporation Missile Division P.O. Box 2628 Detroit, Michigan Attn: Library	John Gates
1	Chrysler Corporation Space Division P.O. Box 29209 New Orleans, Louisiana 70129 Attn: Librarian	
1	Curtiss-Wright Corporation Wright Aeronautical Division Woodridge, New Jersey Attn: Library	G. Kelley
1	Fairchild Stratots Corporation Aircraft Missiles Division Hagerstown, Maryland Attn: Library	
1	Research Center Fairchild Hiller Corporation Germantown, Maryland Attn: Library	Ralph Hall
1	Republic Aviation Fairchild Hiller Corporation Farmington, Long Island New York	
1	General Dynamics/Convair P.O. Box 1128 San Diego, California 92112 Attn: Library	Frank Dore

Report  
Copies  
R   D

	<u>Recipient</u>	<u>Designee</u>
1	Missiles and Space Systems Center General Electric Company Valley Forge Space Technology Center P.O. Box 8555 Philadelphia, Pa. 19101 Attn: Library	A. Cohen G.E. DeSalle
1	General Electric Company Flight Propulsion Lab. Department Cincinnati, Ohio Attn: Library	D. Suichu Leroy Smith
1	Grumman Aircraft Engineering Corporation Bethpage, Long Island, New York Attn: Library	Joseph Gavin
1	Honeywell Inc. Aerospace Division 2600 Ridgeway Road Minneapolis, Minnesota Attn: Library	
1	IIT Research Institute Technology Center Chicago, Illinois 60616 Attn: Library	C.K. Hersh
1	Kidde Aerospace Division Walter Kidde & Company, Inc. 476 Main Street Belleville, New Jersey	R.J. Hanville
1	Ling-Temco-Vought Corporation P.O. Box 5907 Dallas, Texas 75222 Attn: Library	
1	Lockheed Missiles and Space Company P.O. Box 504 Sunnyvale, California 94087 Attn: Library	
1	Lockheed Propulsion Company P.O. Box 111 Redlands, California 92374 Attn: Library, Thackwell	H.L. Thackwell

Report  
Copies

R D

Recipient

Designee

1		Marquardt Corporation 16555 Saticoy Street Box 2013 - South Annex Van Nuys, California 91409	Tom Hudson
1		Martin-Marietta Corporation (Baltimore Division) Baltimore, Maryland 21203 Attn: Library	
1		Denver Division Martin-Marietta Corporation P.O. Box 179 Denver, Colorado 80201 Attn: Library	Dr. Morganthaler F.R. Schwartzberg
1	1	Western Division	R.W. Hallet
	1	McDonnell Douglas Astronautics	G.W. Burge
	1	5301 Bolsa Avenue Huntington Beach, California 92647 Attn: Library	P. Klevatt
1	1	McDonnell Douglas Aircraft Corporation P.O. Box 516 Lambert Field, Missouri 63166 Attn: Library	R.A. Herzmark
1	1	Rocketdyne Division	Dr. R.J. Thompson
	1	North American Rockwell Inc. 6633 Canoga Avenue Canoga Park, California 91304 Attn: Library, Department 596-306	S.F. Iacobellis
1	1	Space & Information Systems Division North American Rockwell 12214 Lakewood Blvd. Downey, California Attn: Library	R.E. Field
1		Northrop Space Laboratories 3401 West Broadway Hawthorne, California Attn: Library	Dr. William Howard

Report  
Copies  
R   D

Recipient

Designee

1		Radio Corporation of America Astro-Electronics Products Princeton, New Jersey Attn: Library	
1		Rocket Research Corporation Willow Road at 116th Street Redmond, Washington 98052 Attn: Library	F. McCullough, Jr.
1		Thiokol Chemical Corporation Redstone Division Huntsville, Alabama Attn: Library	John Goodloe
1	1 1	TRW Systems Inc. 1 Space Park Redondo Beach, California 90278 Attn: Tech. Lib. Doc. Acquisitions	D.H. Lee H. Burge
1		United Aircraft Corporation Corporation Library 400 Main Street East Hartford, Connecticut 06108 Attn: Library	Dr. David Rix
1		United Aircraft Corporation Pratt & Whitney Division Florida Research & Development Center P.O. Box 2691 West Palm Beach, Florida 33402 Attn: Library	R. J. Coar  Dr. Schmitke
1		B. F. Goodrich Company Aerospace & Defense Products 500 South Main Street Akron, Ohio 44311	
1	1	Goodyear Aerospace Corporation 1210 Massillon Road Akron, Ohio 44306	D. Romick
1		Vought Astronautics Box 5907 Dallas, Texas Attn: Library	